

# Storage of Charge in Redox Conductive Polymers Probed with Electron Spin Resonance Spectroscopy

**Ilia Romanovich Kulikov**

Im Fachbereich Physik der Freien Universität Berlin eingereichte  
Dissertation zur Erlangung des Grades eines  
Doktors der Naturwissenschaften

Berlin  
August 2023

Erster Gutachter: Prof. Dr. Jan Behrends  
Zweiter Gutachter: Prof. Dr. Kirill Bolotin  
Tag der Disputation:

# Contents

<b>1</b>	<b>Introduction</b>	<b>7</b>
<b>2</b>	<b>Electrochemical Energy Storage in Redox Conductive Polymers</b>	<b>11</b>
2.1	Rechargeable Electrochemical Cells . . . . .	11
2.1.1	Characteristics of Rechargeable Batteries . . . . .	14
2.2	Electrochemical Instrumentation . . . . .	15
2.2.1	Cyclic Voltammogram . . . . .	15
2.2.2	Charge-Discharge Cycling . . . . .	16
2.3	Redox Conductive Polymers . . . . .	18
2.3.1	Charge Transport Model for Redox Conductive Polymers . . . . .	21
2.4	Organic Radical Battery . . . . .	22
2.5	Organic Electrode Materials . . . . .	22
2.5.1	TEMPO . . . . .	22
2.5.2	PTMA . . . . .	24
2.5.3	NiSalen . . . . .	24
2.5.4	Poly-Di-TEMPO-Salens . . . . .	24
2.5.5	Electro-polymerization of TEMPO-Salens . . . . .	26
2.5.6	Ag/AgCl reference electrode . . . . .	28
2.6	Ex Situ Electrochemistry . . . . .	28
<b>3</b>	<b>Operando EPR Spectroscopy of TEMPO-Salen Electrochemical Cells</b>	<b>35</b>
3.1	Electron Paramagnetic Resonance . . . . .	35
3.1.1	The Spin Hamiltonian . . . . .	35
3.1.2	cwEPR Instrumentation . . . . .	38
3.2	cwEPR Spectroscopy of TEMPO Containing Molecular Fragments . . . . .	42
3.2.1	Room Temperature Spectra of TEMPO <sup>•</sup> Solutions . . . . .	42
3.2.2	Spectra of TEMPO <sup>•</sup> /TEMPO <sup>+</sup> Films . . . . .	45
3.2.3	Spectra of NiSalen Films . . . . .	47

3.3	cwEPR Spectroscopy of a Charging Electrochemical Cell . . . . .	48
3.4	Fabrication of EPR-compatible Electrochemical Cells . . . . .	49
3.4.1	Versatile electrode setup for ex-situ and in-situ spectroelectrochemical EPR . . . . .	49
3.4.2	Fabrication of the modified tube . . . . .	50
3.4.3	Q-factors and cwEPR spectra for p-DiTS in standard and modified tube . . . . .	51
3.5	cwEPR Spectra During a Charge-Discharge Cycle . . . . .	52
3.5.1	Spectral Simulations . . . . .	53
3.5.2	Quantitative Analysis of Potential-Dependent EPR Spectra . . . . .	53
3.6	EPR-Detected State Of Charge . . . . .	54
3.6.1	Formation of Singlet Spin States in a Reduced Cathode Film . . . . .	55
3.7	Monitoring of Degradation Processes . . . . .	55
3.8	Monitoring of Self Discharge . . . . .	55
3.8.1	Electrochemical Cells with Solid Electrolyte . . . . .	56
3.8.2	Low Temperature Measurements . . . . .	56
<b>4</b>	<b>Pulsed EPR Spectroscopy of TEMPO-containing Battery Cathodes</b>	<b>75</b>
4.1	Coherent Spin Motion under Pulsed Microwave Field . . . . .	75
4.1.1	Bloch Equations . . . . .	75
4.1.2	Refocused Spin Echo . . . . .	76
4.1.3	Spin Relaxation Times . . . . .	76
4.1.4	Spin Packets . . . . .	76
4.2	Pulsed EPR Instrumentation . . . . .	76
4.2.1	Pulse Sequences and Measurement Techniques . . . . .	76
4.2.2	Broad-Band Excitation and Instantaneous Diffusion . . . . .	77
4.3	Pulsed EPR Spectroscopy of a charged pDiTBuS Cathode film . . . . .	78
4.3.1	Ex Situ Charging of the Cathode Films . . . . .	78
4.3.2	Field Swept Echo of a charged pDiTBuS Cathode film . . . . .	78
4.3.3	Instantaneous Diffusion in Charged pDiTBuS . . . . .	78
4.4	Simulations of the EDFS Spectra Considering Instantaneous Diffusion . . . . .	81
4.4.1	EDFS in 50 mM TEMPOL Measured with Narrow-Band Pulses . . . . .	81
4.4.2	EDFS in 50 mM TEMPOL Measured with Broad-Band Pulses . . . . .	82
4.4.3	EDFS in PDiTBuS at ESOC 85% Affected by Instantaneous Diffusion . . . . .	83
4.4.4	EDFS in PDiTBuS at ESOC 95% Affected by Instantaneous Diffusion . . . . .	84

<b>CONTENTS</b>	<b>5</b>
4.4.5 Limitation on Shortest Detectable $T_m$ by the Spectrometer Dead Time . . . . .	85
4.4.6 Estimation of Local Spin Concentrations with Instantaneous Diffusion . . . . .	86
4.5 Spin Relaxation in a charged pDiTBuS Cathode Film . . . . .	86
4.5.1 Temperature Dependence of Pulse Spectra of Charged pDiTBuS . . . . .	89
4.6 Padé-Laplace Deconvolution of Polyexponential Decay Signals . . . . .	90
4.6.1 Padé-Laplace Deconvolution of the Echo-Decay and Inversion-Recovery Transients . . . . .	93
4.6.2 Limitation on Shortest Detectable $T_m$ by the Spectrometer Dead Time . . . . .	99
4.6.3 Detection of Domains with Poor Conductivity . . . . .	100
4.6.4 Towards Electron Resonance Imaging of Spin Concentrations in Battery Electrodes . . . . .	100
<b>5 Conclusions and Outlook</b>	<b>103</b>

---

$\vec{e}_x, \vec{e}_y, \vec{e}_z, t$	Laboratory frame of reference
$\vec{\hat{S}} = (\hat{S}_x, \hat{S}_y, \hat{S}_z)$	Spin operator
$h = 6.62607015 \times 10^{-34} \text{ J} \times \text{s}$	Planck constant
$g_e = -2.00231930436118(27)$	Electron g factor
$\mu_B = 9.2740100783(28) \times 10^{-24} \text{ J/T}$	Bohr magneton
$\mu_0 = 1.25663706212(19) \times 10^{-6} \text{ N/A}^2$	Permeability of free space
$\epsilon$	Relative dielectric permittivity
$\vec{B}_0 = B_0 \vec{e}_z$	Static magnetic field
$\omega_L$	Larmor frequency
$\vec{B}_1(\vec{r}, t)$	Microwave field
cwEPR	Continuous wave electron paramagnetic resonance
pEPR	Pulsed electron paramagnetic resonance
DUT	Device under testing
ORB	Organic radical battery
WE	Working electrode (cathode, "+")
CE	Counter electrode (anode, "-")
RE	Reference electrode
$V_{OC}$	Open circuit potential
SoC	State of charge
ESOC	EPR-detected state of charge
CV	Cyclic voltammogram
GCD	Galvanostatic charge-discharge
TEMPO	2,2,6,6-tetramethylpiperidine-1-oxyl
pDiTS	Poly-di-TEMPO-Salen
pDiTBuS	Poly-di-TEMPO-Butyl-Salen
PTMA	Poly-TEMPO-methacrylate
EDFS	Echo-detected field sweep
ID	Instantaneous diffusion
$\langle n \rangle$	Mean spin concentration
$C$	Local spin concentration
$T_1$	Spin-lattice relaxation time
$T_m$	Phase memory time
$t_d$	Microwave detector dead time

---

Table 1: List of abbreviations

# Chapter 1

## Introduction

Life needs energy to continue its spread. Plants use photosynthesis to separate carbon from oxygen and to grow. Higher life forms as humans consume energy during the day and during the night, being dependent on the available energy source [?]. While fossil fuels are still the major source of energy [?] and while fire is used to convert the Joules that hold together hydrocarbon molecules into a "horse power" of a combustion engine and kilowatt-hours in a power socket, there are cleaner and more efficient ways to harvest energy. Photosynthesis had inspired the creation of solar panels that convert the sunlight into electricity, the atom had been tamed in the core of a nuclear reactor to power cities; we can extract energy from sound [?], wind and waves and from the heat of the planet. Moreover, there are hopes and continuous attempts to achieve nuclear fusion [?] - the creation of an artificial Sun by melting together atomic cores - the virtually inexhaustible and clean source of energy. The oil and gas are limited and unevenly distributed resources, wind does not always blow, the Sun does not shine at night, the wild Nature is still unpredictable and the extracted energy has to be stored in order to level out its production and consumption.

With the rise of the technological era, over the last century, energy has been delivered to our homes in form of electricity. Energy storage systems such as fuel cells, supercapacitors and batteries are crucial elements for powering portable electronics and vehicles, or for balancing a power grid with a renewable energy source [42]. The capacity of installed battery storage systems is predicted to increase upto 400 GWh by 2030 [25].

Stable, capacious and powerful batteries have become of great demand for today's energy driven society [114, 110, 76]. The advances in lithium ion technology for rechargeable batteries have enabled energy densities that make it possible to battery-power a wearable Internet-of-things device [60, 66], an airplane [46] or a house [17, 39]. Still, the

application of lithium ion batteries is limited by irreversible processes [58, 27, 119] that occur upon extreme operating conditions such as high power demand [118, 32] or over-discharge [65]. Such degradation processes limit the performance of a battery by lowering its safe operating power, resulting in lower power density and longer charging times. The challenge to overcome these limitations, together with low abundance of Lithium, Cobalt and rare earth metals, [110, 42] and the toxicity of the manufacturing process [86, 84] is motivating research and development of advanced battery technologies [16]. This requires understanding of charge transport and degradation pathways in energy storage materials as well as exploring novel materials such as materials based on organic precursors [64, 49].

The flexible molecular design together with questions regarding unresolved charge transport- and performance limiting mechanisms have inspired a variety of characterization techniques to be developed and applied to both energy storage materials and energy storage devices, operando (during the operation of a device) and ex-situ. Together with electrochemical characterization as the standard method for studying the properties of energy storage materials [100, 117], operando optical microscopy [68], neutron imaging [65], mass spectroscopy [22] and X-ray diffraction [87] were applied to monitor irreversible structural deformations of the components of Li cells during extreme charging conditions.

UV and IR spectroscopy turned out to be particularly useful for studying organic energy-storage materials. For instance, it was possible to observe formation of positive polarons in the NiSalen backbone of the pDiTBuS upon its oxidation [18]. Since the electrochemical processes happen within the bulk of the energy storage material and involve changes in the spin states, imaging techniques based on magnetic resonance can be applied to obtain structural information on the battery electrodes on the molecular level [73, 67, 61, 7]. NMR was used to study dendrite formation, electrolyte dynamics and intercalation of Li ions[55, 31] in Li cells, including operando imaging [95].

Operando continuous-wave EPR (cwEPR) was applied to study redox kinetics of inorganic battery cathodes [72], radical formation and spin densities in redox polymers [18] and in organic electrochemical cells [41, 52].

Pulsed EPR (pEPR) provides an even more powerful toolbox for material studies with the electron spin as a microscopic structural probe. In particular, pEPR provides access to the dipolar coupling between neighboring electron spins and thus the possibility to determine distances between adjacent redox-active centers using dipolar spectroscopy [90] as in spin-labelled proteins [45, 102]. In addition, the hyperfine coupling between electron

and nuclear spins in close vicinity can be measured by electron spin echo envelope modulation (ESEEM) and electron nuclear double resonance (ENDOR) techniques and can thus elucidate the degree of delocalization for charge carriers in ORB materials in a similar way as in organic semiconductors [23].



# Chapter 2

## Electrochemical Energy Storage in Redox Conductive Polymers

This chapter introduces the concept of an organic radical battery, the electrochemical processes in the battery electrodes, the structures of organic electrode materials based on redox conductive polymers and their electrochemical performance. Necessary electrochemical characterization techniques are described. Preparation of electrochemically active organic cathode films with electro-polymerization is described, preparation of spectroscopic samples is described. A general charge transport model for a disordered electro-active conjugated polymer is reviewed.

### 2.1 Rechargeable Electrochemical Cells

Two opposite electric charges separated from each other can store energy in an electrostatic field. It is possible to accumulate many charges on the plates of a capacitor and store some energy [35], but due to the technological difficulties, electrochemical cells are commonly used instead [25]. An electrochemical cell is an energy storage device and a power source that undergoes a chemical reaction to transfer some electric charge from one of its components to another through an external circuit.

A simple electrochemical cell consists of three elements: two spatially separated materials called electrodes, and a solution of mobile ions between them called electrolyte. The two electrodes have different work functions, or, chemically speaking, reduction-oxidation (redox) potentials. The potential difference between the two electrodes is called the open-circuit potential of the cell,  $V_{OC}$ . When the electrodes are connected through an external circuit, as shown in Figure 2.1 a), the charge flows from one electrode to another through the circuit and the ions in the electrolyte rearrange to maintain charge balance [69]. While

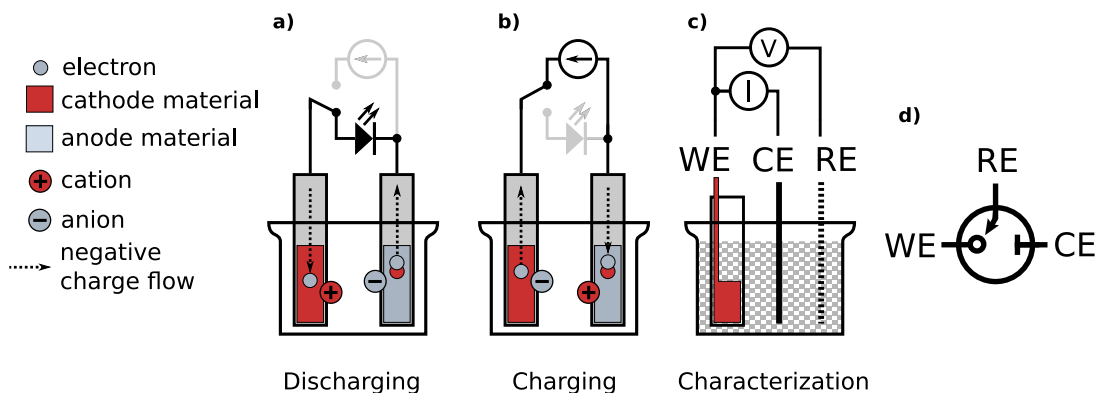


Figure 2.1: Rechargeable electrochemical cell connected to an external circuit for discharging a) and charging b). c): Three-electrode half-cell used for electrochemical characterization and charging of the cathode material. d): symbol for an electrochemical cell used in electric diagrams.

the cell delivers the electric current to the circuit, a chemical reaction is happening on its electrodes: the positively charged electrode, called cathode, is being reduced, obtaining electrons from the negatively charged anode through the external circuit. At the same time, the anode loses electrons and is being oxidized. If the electrodes can undergo a reversible redox reaction, a current applied to the cell restores its charged state, as shown in Figure 2.1 b).

The electrode of an organic electrochemical cell is made of a non-redox-active (metallic) lead and a layer of redox active (organic) molecules. The charge transfer between the conductor and the redox active molecule in the cathode can be described in terms of the energies of molecular orbitals of the cathode molecule [97, 107]. The oxidation potential of a molecule correlates with the energy of its lowest unoccupied molecular orbital (LUMO) [107]. When the electric potential  $V$  of the biased metallic lead is set higher than the energy of the LUMO of the cathode molecule, an electron is transferred from the lead to the cathode molecule and the cathode molecule is reduced. The negative charge that emerges on the cathode is compensated by a positive ion of the electrolyte (cation). The reduction of the cathode results in a positive charge flow from the cathode through the external circuit to the opposite electrode of the cell, the anode. The charge flow implies that, upon adding an electron to the LUMO of the cathode molecule, an electron is removed from the highest occupied molecular orbital (HOMO) level of the anode molecule and the anode molecule is oxidized. The positive charge that emerges on the anode is compensated by a negative ion of the electrolyte (anion). This redox reaction is the discharging of

an electrochemical cell. The opposite reaction is charging. Upon charging, the cathode is oxidized and the anode is reduced.

It is possible to study the redox reaction at one electrode of the cell, e.g. the cathode, using a two-electrode half-cell setup. The studied electrode is called the working electrode (WE). The opposite electrode, called the reference electrode (RE), is made of a known material that maintains a constant composition and has a reproducible potential difference at the electrode-electrolyte interface. Any change in the potential difference between the WE and RE of the half-cell setup is therefore attributed to the processes in the WE only [5]. However, when a half-cell is being charged and the current is flowing through the RE, a chemical reaction can take place at the RE, so its composition and the standard potential can be affected [5, 97]. For this reason, a three-electrode half-cell shown in Figure 2.1 c) is used for characterizing battery electrodes that are designed for significant charging currents.

In the three-electrode half-cell, the charging current is applied between the WE and a chemically inert counter electrode (CE). The oxidation of the WE is accompanied by the formation of a double layer of the electrolyte molecules at the surface of the CE. The electric potential of the WE is measured as a potential difference between the WE and the calibrated RE, inserted in the electrolyte close to the CE. The potential difference between WE and RE is measured with a high impedance voltmeter that ensures no charge flow through the RE. That is, RE does not undergo a chemical reaction during the charging of WE, its chemical environment does not change during the experiment and the measured potential corresponds to the potential of the WE. Due to the finite dimensions of the electrodes and the finite thickness of the double layer around the CE, the RE cannot be inserted at the position of the CE, so the measured potential has a constant offset as the electrolyte between the points where WE, CE and RE are inserted, acts as a voltage divider [5].

A general RE is the standard hydrogen electrode ( $\text{Pt}/\text{H}_2/\text{H}^+$ ), or SHE. The main difference between the various RE is their operation range and a constant potential shift with respect to the SHE due to different equilibrium potentials. The couple  $\text{Ag}/\text{AgNO}_3$  exhibits a shift of 0.7991 V vs. SHE and for the couple  $\text{Ag}/\text{AgCl}$ , the shift is 0.2223 V against SHE [5, 97], although these values can only be used if the configuration is strictly equivalent to the one used for determining them. In other cases, like in the case with a thin electrolyte layer in the modified sample tube, the exact shifts of the RE might differ [97].

### 2.1.1 Characteristics of Rechargeable Batteries

Depending on the redox potentials of the used electrodes, the output voltage of an electrochemical cell ( $V_{OC}$ ) ranges between 0 and 5 V [42]. Most applications require higher voltages, so multiple cells are connected in series to form a battery.

**Capacity, C-rate and State Of Charge** The capacity of a battery  $C$  is measured in mAh. It is the maximal electric charge that can be stored in it. Different electrode materials can store different amounts of charge depending on their chemical structure and macroscopic structure. Due to the unavoidable losses of charge caused by the finite shunting resistance between the battery electrodes, one distinguishes between the charging capacity and the discharging capacity. The capacity of 1 g of an electro-active material is its gravimetric capacity, it is measured in  $\text{mAhg}^{-1}$ . The volumetric capacity is the corresponding value with respect to the volume of the material that is measured in  $\text{mAhL}^{-1}$ . The fraction of charge left in a cell with respect to the full charge that can be stored in that cell in percent is called the state of charge or SoC. The SoC of a fully charged battery is 100%.

A battery is typically charged with a constant current. The magnitude of the charging (or discharging) current relative to the battery capacity determines the rate at which a battery is charged (or discharged). The charging rate, or C-rate is the charge or discharge current in Amps divided by the cell capacity in Ampere-hours. For a modern rechargeable Li-polymer battery a safe charging C-rate cannot exceed 1 C [118]. That means, the charging time for a Li-polymer battery cannot be shorter than 1 hour. The discharge rate of the same battery, however, can be as high as 100 C that corresponds to a discharge current larger than the charging current by a factor of 100. The organic radical batteries can have charging and discharging C rates close to 3000 C and gravimetric discharge capacities upto 111  $\text{mAhg}^{-1}$  [103, 26, 117, 104, 53].

**State Of Health** The capacity of a battery may decrease upon repeated charge-discharge cycling, especially at high C rates [32, 80], over-discharge [65] and extreme environmental conditions [118]. The ratio of the maximum battery charge to its rated as-manufactured capacity expressed in percent is called the battery state of health (SoH). SoH is a measure of the remaining life time of a battery. The decrease in SoH indicates the intensified irreversible processes that take place in an electrochemical cell, such as a physical damage [28], degradation of the electrode material [65, 52] or decomposition of the electrolyte [22]. A damaged cell, especially that can store significant amount of charge, represents a major hazard [65]. Accurate measurements of SoH can prevent hazardous battery malfunctions such as explosions.

## 2.2 Electrochemical Instrumentation

### 2.2.1 Cyclic Voltammogram

The complete electrochemical behavior of a redox active molecular system can be obtained with a series of transient current responses to potentials, applied step-wise to the electrochemical cell containing the system. However for a basic electrochemical characterization a current response during a linearly swept potential is sufficient [5]. During the linear-potential-sweep chronoamperometry, or linear sweep voltammetry, the potential  $E$  applied to the electrochemical cell is swept in a linear manner between the values  $E_{min}$  and  $E_{max}$ , upwards and downwards, with a rate  $v$  ( $\text{mVs}^{-1}$ ):  $E(t) = E_0 \pm vt$ . During the sweep, the current is recorded as a function of the applied potential as shown in Figure 2.2 a). The resulting plot  $i(E)$  is the cyclic voltammogram (CV). The upward potential sweep corresponds to the anodic, or charging branch of the CV and the downward sweep corresponds to the cathodic, or discharge branch. A CV of a three-electrode electrochemical cell with a pDiTBuS electro-active polymer film on the WE is shown in Figure 2.2 b). When  $E$  reaches the oxidation potential of the working electrode, charge transfer happens and the current through the cell increases. This corresponds to the oxidation peak in the cathodic branch. The width of the peak is determined by the temperature of the cell and the number of electrons  $n$  transferred in a single oxidation reaction ( $n = 2$  for poly-di-TEMPO-Salen, the redox conductive polymer described in Section 2.5). The negative current peak in the anodic branch of the CV curve corresponds to the reduction of the WE. The difference between the potentials of the oxidation and reduction peaks arises because of the finite electric capacity of the electro-active film and a finite voltage sweep rate. For higher sweep rates the difference in peak potentials is higher, as the scan rate approaches the RC time constant of the cell.

The area under the anodic branch can be used to calculate the charge that was transferred from the WE upon its reduction from the fully oxidized state. The applied voltage is swept at a known rate, so the anodic branch  $i(E)$  can be plotted vs. time  $i(t)$ , hence the transferred charge equals to the integral under the curve:  $q = \int_{E_{max}}^{E_{min}} i(t)dt$ . By knowing the  $q$  and considering the corresponding chemical reaction (how many electrons are transferred for one molecule) one gets the amount of substance in the electrode  $v = qF$  [mol] and the number of electrochemically active molecules  $N_{echem} = vN_A$  with  $F = 9.46853321233100184 \times 10^4 \text{ C}\times\text{mol}^{-1}$  for the Faraday constant and  $N_A = 6.02214076 \times 10^{23} \text{ mol}^{-1}$  for the Avogadro constant [71]. Given the molecular weight  $M$ , the total mass of the electrochemically active molecules of the film can be calculated, and with the information on the density of the film its dimensions can be estimated. However as demonstrated in Section 3.5.2 and in Refs. [104, 52, 53], the number of electrochemi-

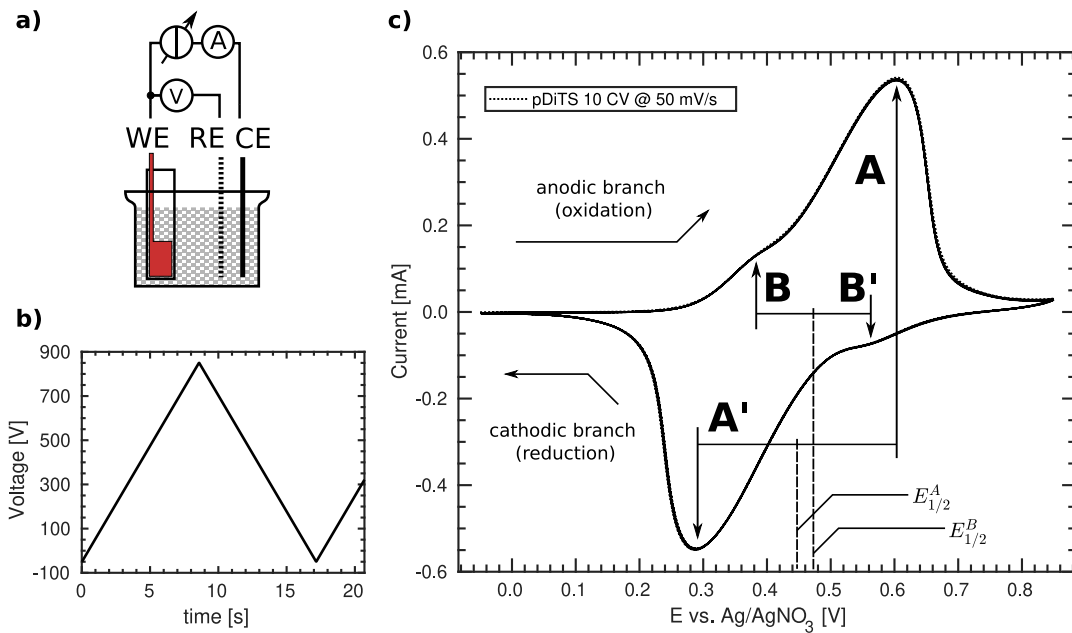


Figure 2.2: a): Electrochemical setup for measuring a cyclic voltammogram. b): Linear voltage sweep at a  $50 \text{ mVs}^{-1}$  rate. c) Cyclic voltammogram of an electro-active polymer cathode film. Oxidation and reduction of the charge-bearing fragments of the film corresponds to the A and A' redox peaks, respectively. Oxidation and reduction of the conductive polymer backbone of the film corresponds to peaks B and B'. The standard oxidation potential of the charge-bearing fragments,  $E_{1/2}^A$ , lies close to the standard oxidation potential of the backbone,  $E_{1/2}^B$ .

cally active molecules in a polymer cathode film can be much lower than the total number of molecules in it.

## 2.2.2 Charge-Discharge Cycling

A constant-current characterization technique called galvanostatic potentiometry [5] can be used in combination with the cyclic voltammetry to study the redox behavior of the electrochemical system quantitatively. The setup for galvanostatic charge-discharge cycling is shown in Figure 2.3 a). The cell is excited with a DC current as shown in Figure 2.3 b) and the potential of the cell is measured as a function of time, as shown in Figure 2.3 c). Upon positive (charging) current, the working electrode of the cell is oxidized. The voltage required to provide the charging current gradually increases, resulting a galvanostatic charging curve shown in Figure 2.3 c). The shape of the charging curve can be approximated by

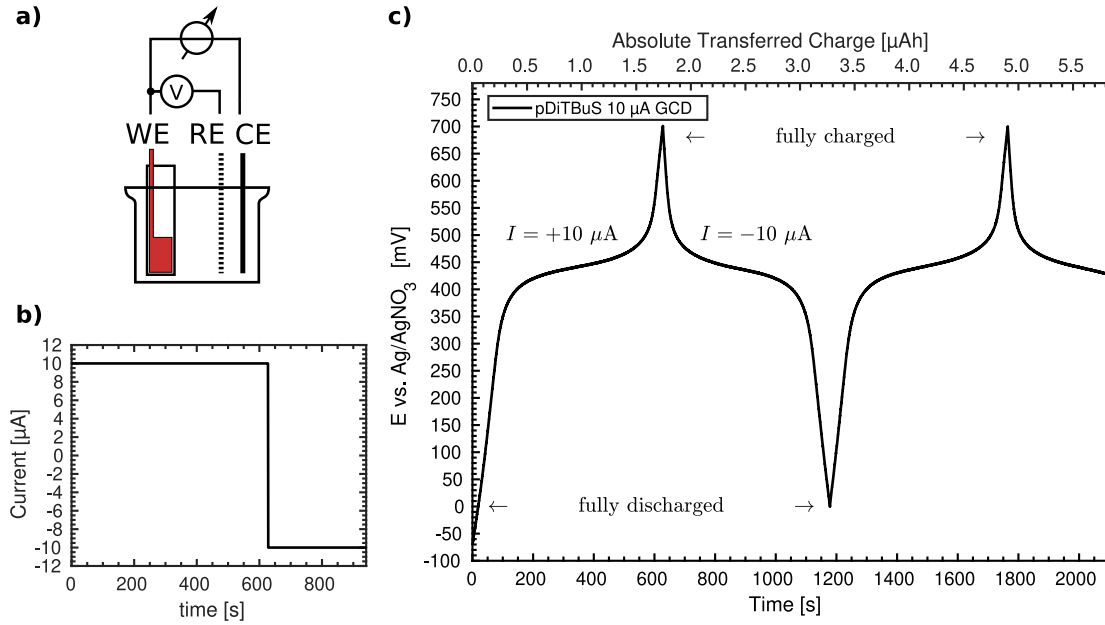


Figure 2.3: a): Electrochemical setup for galvanostatic charge-discharge cycling. b):  $\pm 10 \mu\text{A}$  DC current applied to record the cycling. c) Chronopotentiometry of an electrochemical cell containing electro-active polymer film cathode. Full charging is recognized by the steep increase of the charging curve after passing the Plateau.

considering two major effects: the Faradic current and the displacement current [5]. The Faradic current is caused by the oxidation of the redox active species in the WE. It defines the plateau regions in the middle of the charging and discharging curves. The displacement current is the result of the charging of a double layer around the WE and CE. It explains the capacitor-like response of the charging and discharging curves at their ends [5]. In this regard the electrochemical cell with only one redox active can be treated as a pseudocapacitor [35, 104]. When all redox active species of the WE are oxidized, the voltage required for providing the charging current steeply increases, that is seen in the end of the charging curves in Figure 2.3 c) and 2.4. Eventually, upon charging, the potential of the cell grows beyond the oxidation peak of the WE, according to the cyclic voltammogram (Figure 2.2). Then the charging is stopped and the transferred charge is calculated from the charging time. The same strategy is applied for the discharging curve to determine the discharging capacity of the cell. The reproducibility of the charge-discharge curve indicates the stability of the electrochemical cell. SoH of the cell can be estimated by observing the decrease in the period of the charge-discharge curve.

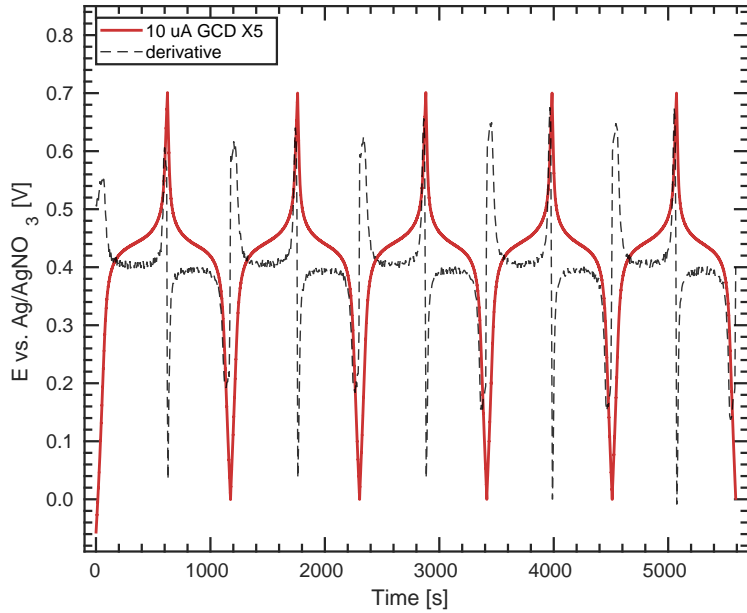


Figure 2.4: Galvanostatic charge-discharge cycling of a pDiTBuS electro-active film with a discharge capacity  $C_{DCG} = 1.6 \pm 0.1 \mu\text{Ah}$  recorded with  $10 \mu\text{A}$  charging and discharging current that corresponds to charging and discharging at a C rate of  $6.3 \pm 0.4 \text{ C}$ .

## 2.3 Redox Conductive Polymers

Redox active macromolecules or polymers [98] are known since 1940s due to the works of Lauth and Cassidy [13] on electron exchange polymers. After the discovery of the conductivity of polyacetylene by Shirakawa, Heeger and McDiarmid in 1977 [96], organic semiconducting polymers with sufficient charge carrier mobilities ( $\mu > 1 \text{ cm}^2\text{V}^{-1}\text{s}^{-1}$ ) were synthesized [40], and the field of organic electronics had emerged [36, 12]. Electron and hole mobilities in modern organic semiconductors have reached the values as high as  $\mu > 10 \text{ cm}^2\text{V}^{-1}\text{s}^{-1}$  [40] and, theoretically, can be above  $\mu > 100 \text{ cm}^2\text{V}^{-1}\text{s}^{-1}$  for organic molecular co-crystals [121], which enables efficient charge transport in fast-switching organic electronic circuits. Organic solar cells [59], organic field effect transistors [50, 112], e-papers [40] and organic electrochemical neurons [34] contain conjugated polymers that have electrical properties of semiconductors, yet can be easily printed in form of thin flexible films without using high temperatures, can be bio-integrated and undergo an environmentally friendly recycling [75]. A combination of conductive polymers with charge-bearing organic radicals [100] has formed the class of redox conductive poly-

mers [12] and lead to the concept of an organic radical battery [88, 74, 70, 109] - the last missing component needed for making a fully organic device.

The key for polymer conductivity is the p  $\pi$  - conjugated network, a system of overlapping  $\pi$  orbitals of carbon in a chain of alternating single and double carbon-carbon bonds that allows charge delocalization along the polymer backbone [36, 57, 12]. An example of a  $\pi$  conjugated network is polyacetylene shown in Figure 2.6b. Polyacetylene exhibits a band structure in the electron energy levels (between  $\pi$  and  $\pi^*$  orbitals) and represents a molecular semiconductor.

Consider a simple organic molecule, ethylene, in Figure 2.5. It contains two carbon atoms and four hydrogens. Each carbon atom has six electrons. Two of them are tightly bound in a 1s orbital and the rest four are valent electrons at 2s and 2p orbitals. The electrons at 2s and 2p orbitals interact to form two  $sp^2$ - hybridized states, and one electron remains at the unhybridized  $p_z$  orbital, as shown in Figure 2.6a.

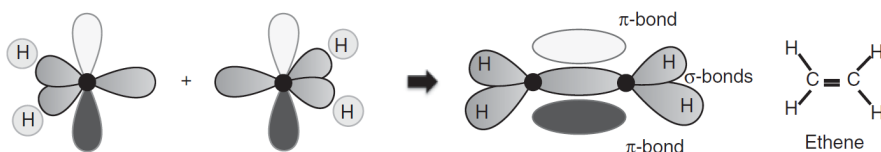


Figure 2.5: Ethylene molecule with  $\sigma$  and  $\pi$  bonds [57].

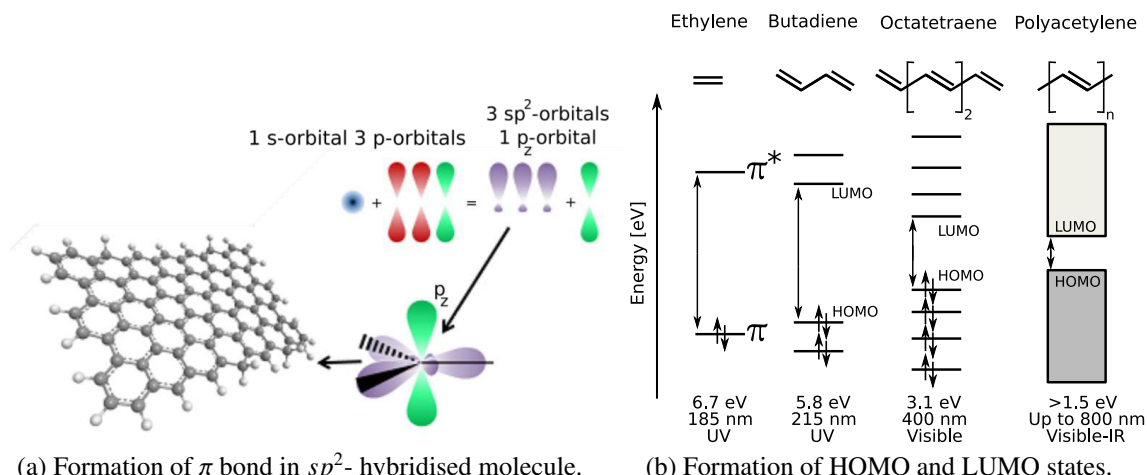


Figure 2.6: Formation of a band gap in a conjugated polymer. Figures adapted from [78].

The  $sp^2$  orbitals form strong  $\sigma$  bonds between adjacent carbon atoms. The  $\sigma$  bonds keep the molecule together. The remaining  $p_z$  orbitals of each carbon atom contain one valence electron each. The  $p_z$ -electrons interact with each other and form a  $\pi$  bond so that  $p_z$  electrons are shared between the carbon atoms. The interaction between  $p_z$  orbitals results in two hybridized molecular orbitals, the bonding ( $\pi$ ) and the antibonding ( $\pi^*$ ) orbitals. A  $\pi$  orbital is described by a symmetric wavefunction and  $\pi^*$  orbital is described by an anti-symmetric wavefunction. A  $\pi$  orbital has a lower energy than  $\pi^*$ , as shown in Figure 2.6b. The symmetric  $\pi$  orbital is more energetically favorable, so the most of electrons occupy it at the equilibrium. Because of that, the  $\pi$  orbital is called the Highest Occupied molecular orbital (HOMO) and  $\pi^*$  is the Lowest Unoccupied Molecular Orbital (LUMO). There is a forbidden energy zone between HOMO and LUMO which is equivalent to a bandgap of a semiconductor. In a longer molecule, the  $\pi/\pi^*$  states are delocalized over many carbon atoms. This is known as conjugation and the number of conjugated atoms determine the conjugation length.

As conjugation length increases, the HOMO and LUMO levels for each pair of carbon atoms in the molecule become slightly different. In a polymer with a very large conjugation length, many energy levels around HOMO and LUMO overlap which forms energy bands. The formation of bands in conjugated polymers is shown schematically in Figure 2.6b [57, 78].

Even though conjugated polymers have band-like energy structure and a bandgap, their charge-transport properties are different from crystalline semiconductors. The energy bands are forming within a single polymer chain and a charge carrier can walk along the backbone of the polymer freely. Real polymer chains have finite lengths and this is what brings disorder to an organic semiconductor (Figure 2.7.a). The disorder causes localization of charges, so when an external electric field is applied, a charge needs to hop from one localized state to another for electric current to flow (Figure 2.7.b). Hopping is a tunnelling process; it happens at much slower rates than the movement within the  $\pi$ -conjugated backbone. This mode of charge transport is referred to as the hopping transport [101].

If an organic semiconductor consists of relatively short molecular fragments, the charge carriers need to hop via localized energy states. In Figure 2.7 c) it is shown how a charge moves through a disordered organic semiconductor choosing the optimal path in both energy and space domains. The localized states act as charge traps and they decrease charge mobility [113].

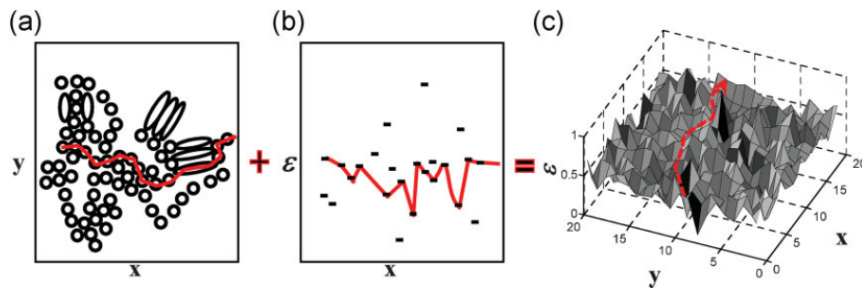


Figure 2.7: The transport sites are distributed both in space (a) and in energy (b). The line describes a possible path that a charge carrier takes while hopping under applied electric field. The trajectory is affected by energy distribution (c). The picture is taken from [101].

### 2.3.1 Charge Transport Model for Redox Conductive Polymers

The transfer of charge between the metallic substrate of the electrode and the surface-bound molecules of the electrode can be described in terms of the electrode workfunction, applied potential, electrolyte dynamics and the LUMO level of the electrode molecule [5]. On the contrary, the transfer of charge between the molecules inside the volume of the electrode is a complex process that involves hopping and time-dependent delocalization of the charge carriers in the percolated network of the porous electrode material under a changing electrostatic field that is dependent on the state of charge of the electrode, as well as on the diffusion of the electrolyte ions. The molecular systems for electrochemical charge storage are inherently disordered materials and the electric performance of a film containing those molecules is strongly dependent on the deposition method, as well as on the molecular structure [109, 120]. The particular charge transport models have been developed that are applicable to certain classes of polymers (look at that chapter in the polymer book + last talk at FU and show what was done), but so far there has not been a unified physical model that would describe the charge transport phenomena in redox-conductive polymer films.

The charge transfer within the redox-conductive polymer electrode governs the speed, reversibility, released by-products and physical conditions of the redox reaction in an organic electrochemical cell, that are the key factors that define the charging rate, cycling stability, self-discharge rate and the area of application of ORBs. This type of redox reaction had been of great interest for the field of energy storage, particularly, electrochemistry, where numerous characterization techniques have been developed to optimize the architecture of electrochemical power sources. In the following chapters a spectroelectrochemical analysis of organic redox-conductive polymers containing nitroxyl radicals is presented using the toolbox of the electron spin resonance spectroscopy.

## 2.4 Organic Radical Battery

Batteries based on conjugated polymers containing stable radical moieties as high-capacitance groups represent a promising class of future electrochemical power sources - organic radical batteries (ORB) [70, 74, 108, 88]. ORB combine the advantages of high-power supercapacitors, namely high discharge rates, and the high energy density of conventional lithium-ion technology. In contrast to the lithium-ion battery, the charging of an organic battery does not involve intercalation of metal ions into the electrodes. This reduces the structural change of the electrode upon repeated recharging which allows for a longer cycle life of an ORB. The semi-conducting nature of organic electrodes reduces the Joule heating during the battery operation, and this allows for higher charge/discharge rates. The amorphous and swollen structure of organic electrodes allows the electrolyte ions to diffuse faster into the electrode, which also increases the charge/discharge rate [75]. A further beneficial property of organic materials over traditional inorganic materials is their availability and the low cost of the starting materials for the synthesis of the target polymers in conjunction with good mechanical properties [42, 69, 26]. The large knowledge base on polymer processing allows for inkjet printing, roll-to-roll processing and other low-cost manufacturing techniques for making low-cost, flexible and light-weight integrated devices, including flexible plastic batteries [42, 75].

## 2.5 Organic Electrode Materials

ORB based on redox polymers containing stable radicals [70] have been shown to compete with or even outperform conventional Li based batteries in terms of power densities [100] with the additional benefit of being free from rare precursors, inheriting mechanical properties of plastics and electrical properties of semiconductors [26, 11, 30]. Advanced molecular design techniques allow for tuning of the electrochemical properties of the redox polymers [43], that brings in a rich variety of organic energy storage materials [109, 104, 44] and creates a large room for their optimization.

### 2.5.1 TEMPO

TEMPO (2,2,6,6-tetramethylpiperidine-1-oxyl) shown in Figure 2.8 a) is a small molecule and a stable radical that can undergo a fast and reversible redox reaction between  $\text{TEMPO}^\bullet$  and  $\text{TEMPO}^+$ . TEMPO is an inexpensive organic compound [104] produced from acetone

with liquid ammonia, hydrazine and peroxide [12]. TEMPO radicals are widely used as spin labels studies of biological systems with electron spin resonance [8], because the unpaired electron of  $\text{TEMPO}^\bullet$  has a well defined spectral signature that changes when the local environment of a TEMPO fragment changes.

TEMPOL is a TEMPO with an OH group. It forms crystals.

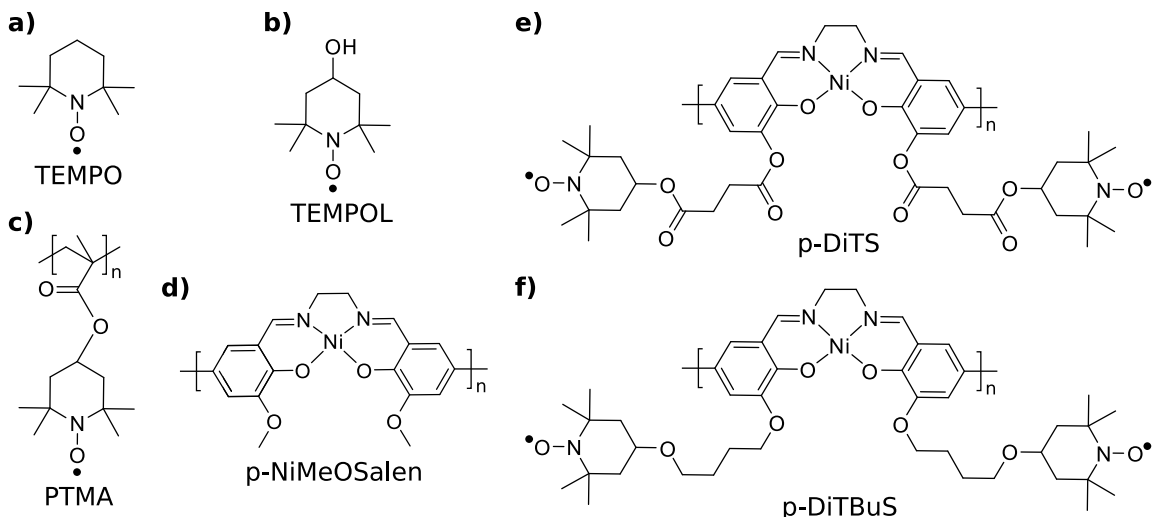


Figure 2.8: Chemical structures of the molecular fragments and polymers that were used for making a battery cathode containing stable nitroxide radicals.

Redox conductive conjugated polymers containing TEMPO redox groups, as pDiTBuS (poly-di-TEMPO-Butyl-Salen) shown in Figure 2.10, demonstrate particularly promising energy and power densities [103]. The pDiTBuS was designed as a cathode material: it is oxidized when the electrochemical cell containing this material is charged. A film of pDiTBuS comprises a high concentration of redox active stable nitroxyl radicals attached to a conjugated polymer backbone that interconnects them as a molecular wire. Such system can be viewed as a highly disordered molecular hole-transporting semiconductor (the poly-NiSalen backbone) that contains a large amount of hole traps (TEMPO groups) attached to it with butyl linkers. When the film is reduced (discharged), the TEMPO groups are in the radical state and act as unfilled traps. Upon oxidation (charging), the TEMPO fragments lose an unpaired electron and acquire a positive charge, so the traps are being filled with holes. The reversible redox reaction in the pDiTBuS film is demonstrated in a cyclic voltammogram shown in Figure 2.2, c) and in the equal charging and discharging capacity of the film in Figure 2.4, c).

While active electrode materials with nitroxide radicals as redox-active groups are ideally suited for organic radical batteries (ORBs) that exhibit high power densities, the

broad application of most nitroxide-based materials is limited by their moderate electrical properties. A promising route towards overcoming the conductivity problem is the use of polymers that combine radical-containing moieties and a conductive backbone. This strategy was successfully followed in a number of studies focusing on different polymers [82, 4, 47, 111, 3, 92]. The standard redox potential of the NiSalen molecular backbone ( $E_{1/2}^B$  in the middle of the peaks B and B' in Figure 2.2) lay close to the standard redox potential of the attached nitroxide charge-bearing fragments ( $E_{1/2}^A$  in the middle of the peaks A and A' in Figure 2.2) - that ensures an efficient charge transport between the charge-bearing fragments and the conductive backbone and allows for very high charge and discharge rates up to 3000 C [103, 52].

### 2.5.2 PTMA

A simple organic radical polymer containing TEMPO is poly-TEMPO-methacrylate) (PTMA, Figure 2.8 c). The polymer backbone of PTMA consists of single C-C bonds and therefore is not conductive, so the transport of charge in a PTMA film has to be mediated by adding conductive mesh such as activated carbon. When mixed with conductive carbon additive, PTMA has become a standard cathode material for ORBs and Li-ORBs, providing a discharge cell voltage of  $V_{OC} = 3.5$  V (with a Li anode) and a theoretical discharge capacity of  $C_{theo} = 111$  mAh/g [14]. PTMA is soluble in acetonitrile (AN), chloroform (CF), tetrahydrofuran and dichlormethane. It is claimed to be insoluble in toluene, ethers, carbonates, and alcohols, however it becomes gel-like with some of these solvents [97].

### 2.5.3 NiSalen

The molecular backbone of a redox conductive polymer has to conduct electric charge. A NiSalen molecule is a Schiff complex of Ni that has a conjugated path through it. The conductivity of NiSalen was measured. Upon oxidation of a polymeric NiSalen, the formation of positive polarons was observed in it with UV-Vis spectroscopy [18], that suggests p-NiSalen is a p-type molecular semiconductor. p-NiSalen exhibits electrochemical capacity and can store up to two positive charges per monomer unit.

### 2.5.4 Poly-Di-TEMPO-Salens

Redox conductive conjugated polymers containing TEMPO (2,2,6,6-tetramethylpiperidine-1-oxyl) redox groups, as pDiTS [103, 52] (poly-Di-Tempo-Salen) and pDiTBuS [53] (poly-di-TEMPO-Butyl-Salen) shown in Figure 2.8 e) and f), demonstrate particularly promising energy and power densities with charging rates upto 3000 C and gravimetric

capacity up to  $91.5 \text{ mAh g}^{-1}$  for pDiTS [103] and up to  $75 \text{ mAh g}^{-1}$  for pDiTBuS [53]. pDiTS and pDiTBuS have similar molecular structures, except for pDiTBuS has no oxygens in the linkers that connect the backbone to the TEMPO fragments, which has led to its higher electrochemical stability and a more efficient electro-polymerization, that allows for growing thicker films. pDiTS is a charge storage material that consists of TEMPO redox active molecular fragments [104, 45, 33] interconnected by a redox conductive conjugated NiSalen backbone [103, 18]. DiTS and DiTBuS monomers were synthesized in the Levin group at the Saint-Petersburg State University.

pDiTS was designed as a cathode material: it is oxidized when the electrochemical cell containing this material is charged. A film of pDiTBuS comprises a high concentration of redox active stable nitroxyl radicals attached to a conjugated polymer backbone that interconnects them as a molecular wire. Such system may be viewed as a highly disordered molecular hole-transporting semiconductor (the poly-NiSalen backbone) that contains a large amount of hole traps (TEMPO groups) attached to it with butyl linkers. When the film is reduced (discharged), the TEMPO groups are in the radical state and act as unfilled traps. Upon oxidation (charging), the TEMPO fragments lose an unpaired electron and acquire a positive charge, so the traps are being filled with holes [53].

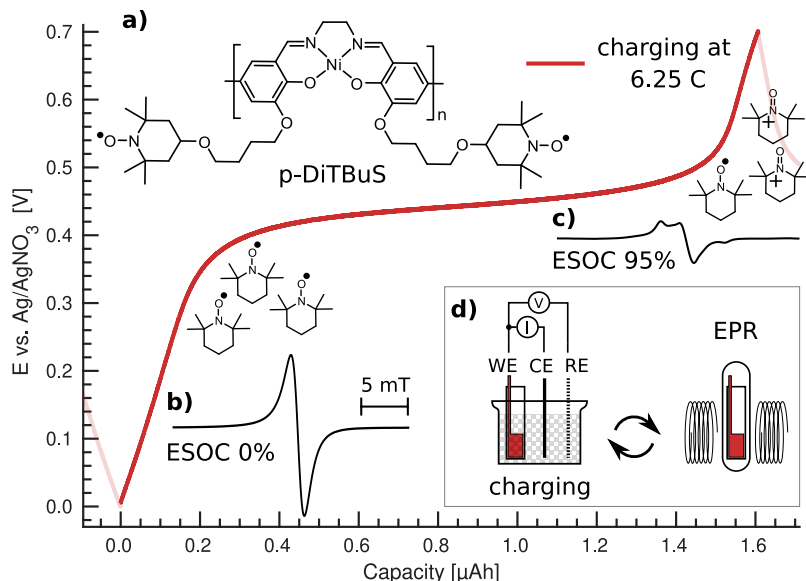


Figure 2.9: Galvanostatic charge-discharge curve for a pDiTBuS cathode film at  $10 \mu\text{A}$  (6.25 C), chemical structure of pDiTBuS (a), normalized cwEPR spectral signatures for reduced (b) and oxidized (c) states. Scheme of the ex-situ EPR measurement on the pDiTBuS half cell (d).

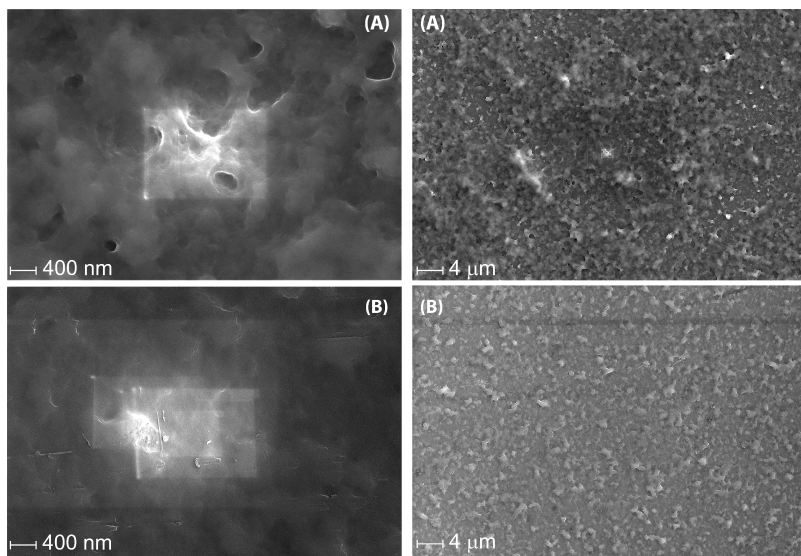


Figure 2.10: Scanning electron microscope images of a pDiTS film in a reduced (a) and oxidized (b) states, image adapted from Ref. [103].

### 2.5.5 Electro-polymerization of TEMPO-Salens

The process of polymerization is connecting multiple monomer units of one sort to a continuous molecular chain. Among various polymerization techniques, redox conductive molecules with pendant charge bearing groups the cyclic electropolymerization turned out to be an efficient technique.

#### Fast And Capacious:

"Electrochemical polymerization of DiTS was studied by means of the EQCM technique on piezoelectric crystals coated with platinum using a linear voltage sweep. The CV of DiTS (Figure FAC2A) shows the paired peaks A and A' at 0.55 V and 0.47 V respectively, which correspond to charging and discharging of the nitroxyl fragments. An irreversible anodic peak B corresponds to oxidative coupling of the NiSalen fragments of DiTS, which results in the polymer p-DiTS [105, 51]. The gradual increase of the CV current and the electrode mass (Figure FAC2A) in the subsequent cycles indicates the course of the polymerization process. An unusual feature in the EQCM curves, recorded during the electropolymerization process, is that the mass growth at the electrode occurs predominantly at potentials below the peak A' (Figure FAC2A), which is in contradiction to previous reports on the deposition of a NiSalen-type polymer, where polymerization occurs at potentials above the oxidation peak of the monomeric NiSalen.[22] The CV sweep boundaries were varied to establish the optimal conditions for the polymerization of DiTS.

Only the redox peaks of the TEMPO moieties in solution are observed on CV (Figure 2C, curve i) while sweeping in 0.40–0.75 V range without polymer formation. An extension of the anodic boundary to 0.90 V (Figure FAC2C, curve ii) led to an increase in EQCM mass and CV current, which indicates the polymer growth on the electrode surface. Further extension of the anodic region of the CV range (Figure 2C, curve iv) did not improve the polymerization process, but led to a decrease of the conductivity of the film due to overoxidation (Figure FACS4), highlighting 0.90 V as an optimal position of the anodic boundary. While polymerization is possible at higher potentials on the surface of a clean substrate, low conductivity of the overoxidized film is blocking further monomer oxidation on the surface, leading to rapid decrease in monomer oxidation current (Figure S4 and Figure 2C, curve iv). When the cathodic boundary was set near the A/A' pair and the CV was performed between 0.35 V and 0.90 V (Figure FAC2C, curve iii), no polymerization occurred, emphasizing the crucial role of the charge-discharge of the nitroxyl fragments in the polymerization process.

The conventional mechanism for the chain growth of polymeric NiSalens is based on the formation of radical cation species. Although the NiSalen-centered radical cations of DiTS are formed on the peak B (Figure FAC2A), apparently the polymerization proceeds at a low rate in this area of potentials, compared to other NiSalen type complexes [77]. Based on the obtained results, we assume that the positive charge density both on the monomer molecules and deposited polymer layers grow rapidly above the A (Figure FAC2A) peak potential due to simultaneous oxidation of the NiSalen core and two TEMPO fragments in one molecule. High charge density causes intermolecular coulombic repulsion, acting as a coulombic "shield", which hinders the coupling of radical cation species and prevents the chain growth. As soon as the potential has decreased to the A' (Figure FAC2A) peak on the negative scan of the CV (Figure S5C, point C), rapid polymer growth occurred due to the discharge of the p-DiTS film, which deactivates the coulombic shield. The formation of the polymer proceeds until the shield recovers during the next CV cycle due to the oxidation of nitroxyl fragments. At this point, a sharp decrease in mass occurs due to the desorption of the monomeric DiTS molecules repelled by the charging coulombic shield. The scheme of this process is depicted in Figure FAC2B and a scheme of the polymer formation process in Figure FAC2D.

The mass growth for one deposition cycle is ca. 0.3  $\mu\text{g cm}^{-2}$  both for 5 mV s<sup>-1</sup> and 50 mV s<sup>-1</sup> CVs. Polymer deposition is observed both at potentials higher than 0.8 V and lower than 0.4 V, and during low rate CV almost two thirds of the overall polymer mass is formed at potentials more positive than the potentials of the A/A' peaks. On the contrary, at 50 mV/s only one third of the polymer is formed at potentials higher

than 0.8 V. This indicates that the Coulombic shielding from oxidized TEMPO groups allows coupling between the radical cations of DiTS and the charged TEMPO groups, though at quite low rate. The possibility of polymerization at both potential regions was confirmed by the experiment consisting of a series of successive iterations of potentiostatic and potentiodynamic syntheses, as well as open-circuit rest periods (See SI and Figure FACS6 for further discussion”)

### 2.5.6 Ag/AgCl reference electrode

The Ag/AgCl reference (RE) electrode was formed by coating a layer of AgCl onto a 250  $\mu\text{m}$  Ag wire galvanically from a 1 M aqueous solution of KCl. For that, the Ag wire and a Pt wire were connected as a cathode and an anode respectively to 10 mL of the KCl solution and a DC potential of 500 mV was applied for 7500 s which resulted in a dark AgCl layer deposited onto the Ag cathode. In the beginning of the galvanic deposition, the current through the KCl solution was changing in a jumpy manner, that indicated the growth of the AgCl layer. The galvanic process was stopped after the current was stable for at least 300 s.

JOSHKAS PLOT HERE

## 2.6 Ex Situ Electrochemistry

The pDiTBuS film was brought to the desired oxidation state by galvanostatic discharging with a current of 10  $\mu\text{A}$  in a three-electrode electrochemical cell in a 5 ml beaker with the electrodes and the electrolyte described above. Each potential of the film was reached by first fully charging the cell to 700 mV and then discharging it to the desired potential (labeled points in Figure 2.13). When the desired potential was reached, the output relay of the potentiostat was opened so that no current went through the cell after charging. The substrate with the WE and the pDiTBuS film was removed from the charging cell, placed in a 5 mm OD quartz EPR tube, evacuated down to  $< 5 \times 10^{-3}$  mbar, filled with He up to a pressure of 500-600 mbar, then flame sealed with a H<sub>2</sub>/O<sub>2</sub> burner.

After reaching the fully charged state with 10  $\mu\text{A}$  (by  $t = 0$  in Figure 2.14), a 10  $\mu\text{A}$  discharge current was applied to reach the four states of charge considered in this study (a-d in Figure 2.14 and in Figure 2.13). Initially, the full charging capacity of the film was 1.48  $\mu\text{Ah} = 5.11 \text{ mC}$  (3.29e+16 electrons withdrawn upon the full charging). The charging capacity has decreased by 0.06  $\mu\text{Ah}$  (4%) after the four temperature cycles between 300 K and 5 K during the cryogenic EPR measurements.

From the quantitative analysis of the GCD for each SoC, we calculate the number of elementary charges that are transferred to the film (withdrawn from the film) upon charging (discharging). The GCD and the calculated values of the transferred charge are shown in Figure 2.14. During the full discharge from +700 mV down to -200 mV the pDiTBuS film has gained a total charge of  $1.355 \mu\text{Ah} = 4.88 \text{ mC}$  (d), corresponding to  $3.01e+16$  electrons that had been transferred to the film.) The considered SoC correspond to discharging by  $0.020 \pm 0.005 \mu\text{Ah}$  (Figure 2.14 a,  $(5 \pm 1) \times 10^{14}$  electrons injected),  $0.060 \pm 0.005 \mu\text{Ah}$  (Figure 2.14 b,  $(1.4 \pm 0.1) \times 10^{15}$  electrons injected),  $0.480 \pm 0.005 \mu\text{Ah}$  (Figure 2.14 c,  $(1.07 \pm 0.01) \times 10^{16}$  electrons injected) and  $1.360 \pm 0.005 \mu\text{Ah}$  (Figure 2.14 d,  $(3.05 \pm 0.01) \times 10^{16}$  electrons injected). The SoC values determined from the respective potentials are different when mapped to the initial discharge curve in Fig. 2.13 and when considering the individual discharge curves in Fig. 2.14, as the film was gradually losing its capacity during the temperature cycling, so the discharge curves were reaching the considered potentials at shorter times, leading to a lower Coulomb counting, lower discharge capacity and therefore a lower SoC.

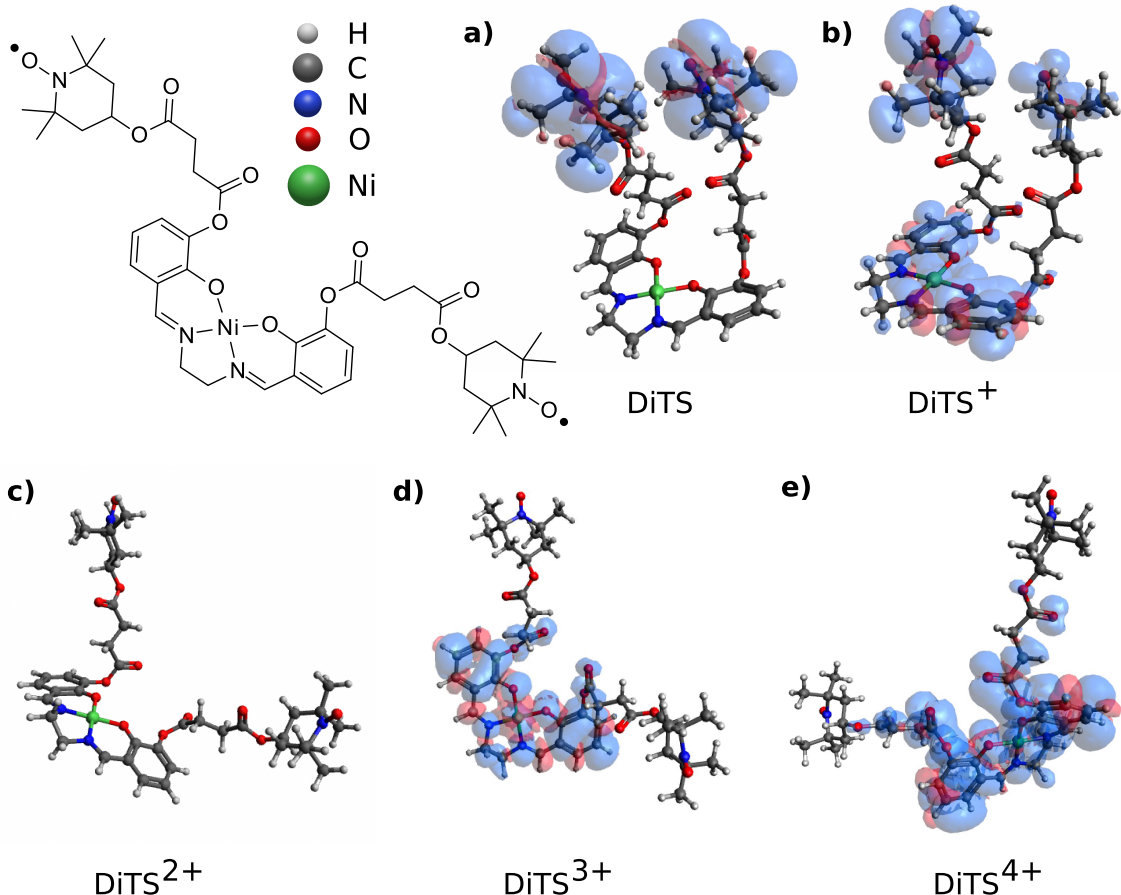


Figure 2.11: Spin density in a single DiTS monomer unit for various oxidation states calculated by Marcel Gauglitz with density-functional theory in ORCA [?], using the def2-TZVP functional basis set for the geometry optimization and the calculations of the spin density. The calculations were carried out at the high-performance computing cluster Curta of the Free University of Berlin [6]. a): neutral DiTS with two TEMPO radicals, b) singly oxidized DiTS (one hole injected), b) doubly oxidized DiTS showing no spin density, c) DiTS<sup>3+</sup> showing a positive polaron localized on the NiSalen backbone, d) DiTS<sup>4+</sup> showing increased spin density on the backbone.

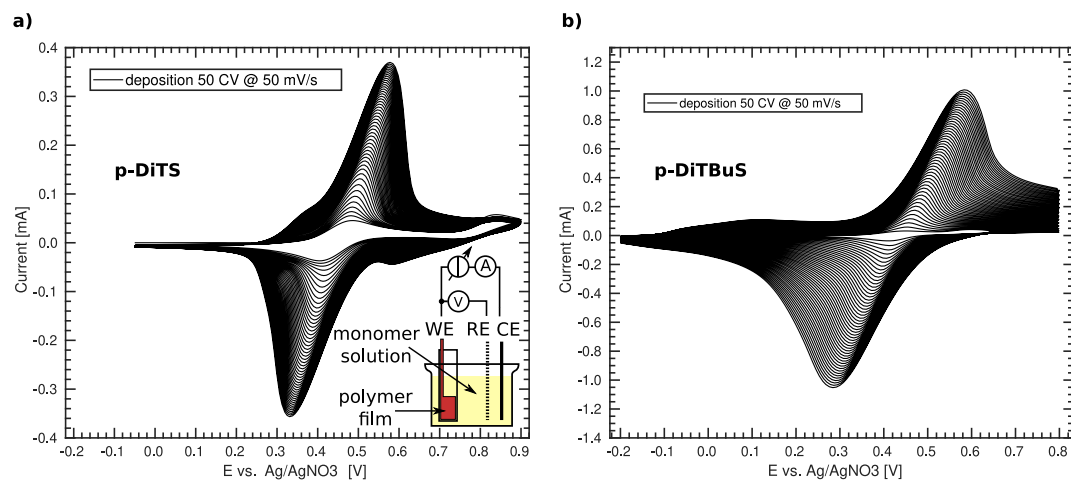


Figure 2.12: Deposition of TEMPO-Salen films with cyclic electrochemical polymerization from 1 mM monomer solutions in the 10 mM Et<sub>4</sub>NBF<sub>4</sub> electrolyte at 50 mVs<sup>-1</sup> and 50 deposition cycles. a): pDiTS, b): pDiTBU<sub>S</sub>.

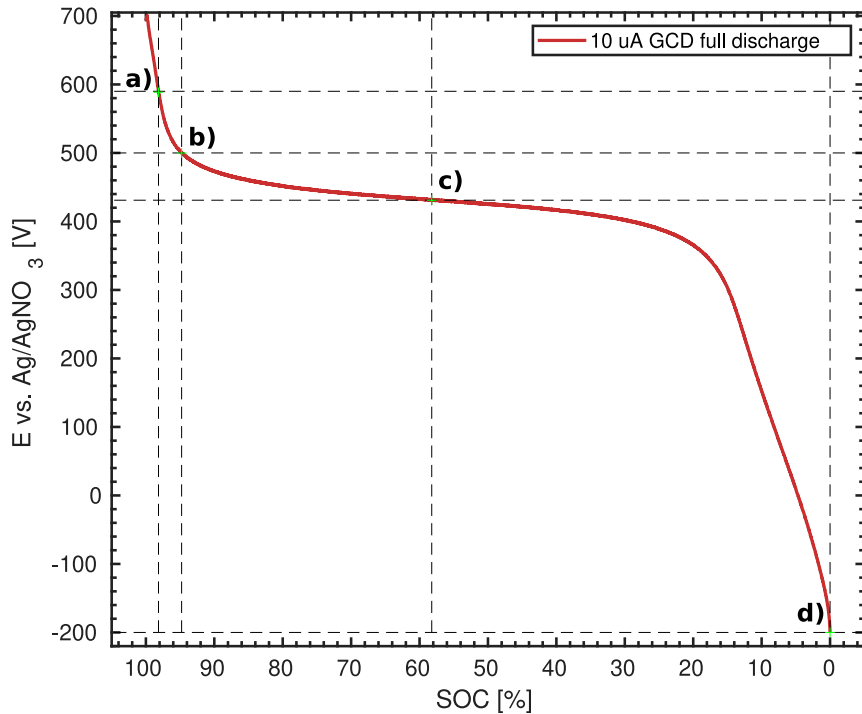


Figure 2.13: Initial galvanostatic discharge curve for the pDiTBuS film with the redox potentials described in the main text. Since the film has lost 12% of its capacity during the temperature cycling, the SoC determined from the potentials mapped to the initial curve are lower than the SoC determined from the individual discharge curves (given in brackets). The SoC values corresponding to the initial (individual) discharge curve are a): SoC 98 (98)% , b): SoC 94 (96)% , c): SoC 57(65)% , d): SoC 0(0)% . (Dis-)charging current: 10  $\mu$ A, charging rate: 6.25 C. After this initial discharging, the pDiTBuS film has undergone 10 charge-discharge cycles and 4 temperature cycles.

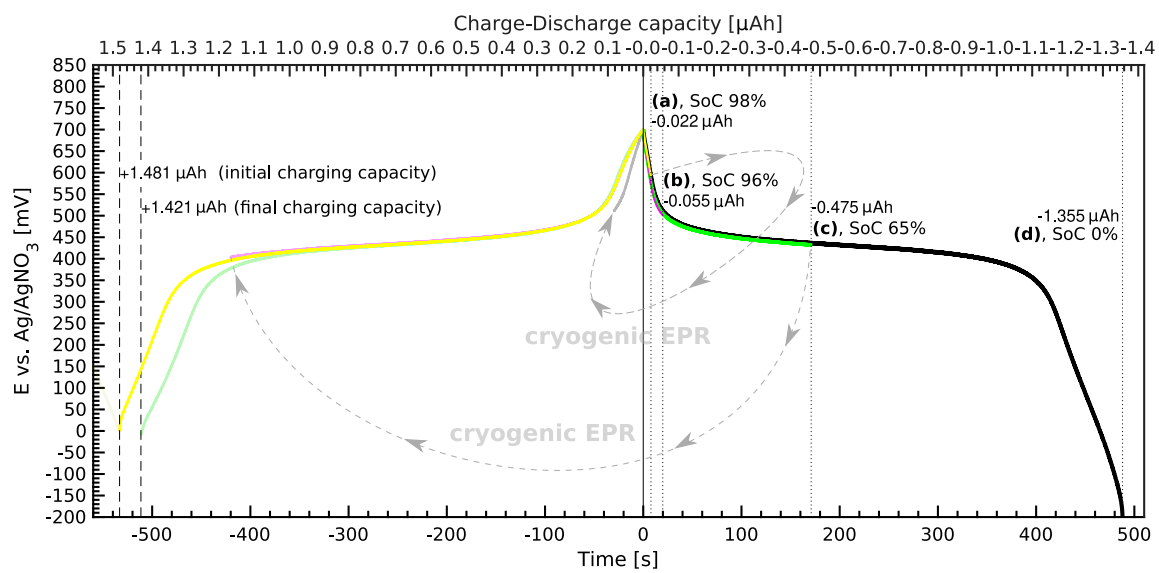


Figure 2.14: Calculation of the number of withdrawn electrons from a pDiTBuS film for the four states of charge. At negative times the pDiTBuS film is charged, corresponding to the withdrawal of electrons from the film. At positive times the film is discharged. The number of transferred electrons during discharging is determined from the four overlaid galvanostatic discharge curves (a-d).



# Chapter 3

## Operando EPR Spectroscopy of TEMPO-Salen Electrochemical Cells

### 3.1 Electron Paramagnetic Resonance

In this section, the phenomenon of electron paramagnetic resonance is briefly described with details that are required to interpret the spectra of a charging electrochemical cell containing nitroxide radicals attached to a conjugated polymer backbone. After the introduction of the spin Hamiltonian, an experimental procedure to observe the corresponding spin transitions with continuous microwaves is described. The characteristic spectra of nitroxide radicals in various environments are described. That information is used to decompose the complex spectra of a charging cell to identify the state of charge of the cell and the by-products that are being released during the cell operation.

#### 3.1.1 The Spin Hamiltonian

**Electron Spin** In the Poincaré group of special relativity [85], when rotations are considered together with the relativistic boosts [20], there emerges an additional quantity that is associated with rotation and is preserved together with the orbital angular momentum, yet this quantity is retained for point objects - it is called spin [54]. Spin is quantized [29]; it can take values in integer- or half-integer multiples of the Planck's quantum of action  $\hbar$  up to a certain magnitude  $S$ . The electron, as a fundamental particle and a fermion, bears a half-integer spin with a magnitude  $S = 1/2$ .

An isolated electron has two degenerate spin states - spin-up  $|\uparrow\rangle$  and spin-down  $|\downarrow\rangle$  - that are eigenfunctions of the square of the spin operator  $\hat{s}^2$  with the same (degenerate) eigenvalue  $\hat{s}^2|\uparrow\rangle = \hat{s}^2|\downarrow\rangle = \frac{3}{4}\hbar^2$ . The states  $|\uparrow\rangle$  and  $|\downarrow\rangle$  are also eigenfunctions of the  $z$

component of the spin operator, but correspond to different (non-degenerate) eigenvalues  $m_s = \pm \hbar/2$  [89]:

$$\begin{aligned}\hat{s}_z |\uparrow\rangle &= +\frac{\hbar}{2} |\uparrow\rangle \\ \hat{s}_z |\downarrow\rangle &= -\frac{\hbar}{2} |\downarrow\rangle\end{aligned}\quad (3.1)$$

**g factor** Spin combines with the charge of the electron to endow the electron with a magnetic moment  $\mu_{spin} = \gamma S$ , where  $\gamma = \frac{g_e \mu_B}{\hbar} \approx 28$  GHz/T is the gyromagnetic ratio of the electron,  $\mu_B = \hbar e/m_e$  is the Bohr magneton and  $g_e \approx 2$  is the electron g factor [9]. The g factor connects the spin of a particle with a magnetic moment that the particle expresses through interactions with external fields [94]. The Dirac quantum theory of the electron predicts  $g_e = 2$  [83]. However, up to date,  $g_e = 2.00231930436256(35)$  has been measured to the unprecedented accuracy of 0.13 ppt [21]. This measurement lies at the frontier of modern particle physics and the accordance of the measured  $g_e$  with the value obtained with quantum electrodynamics [94, 21] is the triumph of the quantum field theory [24].

Depending on the local environment of an electron, its g factor can change from  $g_e$  due to the spin-orbit coupling that changes the observed magnetic moment of the electron [9]. The magnetic moment of an electron can therefore be used as an extremely sensitive probe of the electron's local environment. The g factor of an electron localized in a molecular orbital can be anisotropic, depending on the shape of the orbital. Anisotropic g factor is represented by a  $3 \times 3$  g matrix that can almost always be diagonalized [9] by an appropriate rotation of the molecular coordinate system.

**Zeeman Splitting** When an electron is placed in a static magnetic field  $\vec{B}_0 = B_0 \vec{e}_z$ , its magnetic moment experiences a torque and precesses in the  $xy$  plane about the field axis with the Larmor frequency  $\omega_L = \gamma B_0$ . The magnetic moment of the electron has two possible projections on the magnetic field axis, according to 3.1. The two corresponding eigenvalues  $\pm \frac{\hbar}{2}$  define the energy difference between the states  $|\uparrow\rangle$  and  $|\downarrow\rangle$  when the spin couples to the external magnetic field, that is known as the Zeeman splitting. The energy difference between  $|\downarrow\rangle$  and  $|\uparrow\rangle$  in a magnetic field is the Zeeman energy.

The energy of an isolated electron placed in the external magnetic field  $\vec{B}_0$  is the energy of the electron's magnetic moment in that field, that is given by the eigenvalue of the spin Zeeman Hamiltonian:  $\hat{H}_{EZ} = \frac{\mu_B}{\hbar} \vec{B}_0 g_e \vec{s}$ . In the laboratory frame of reference  $\vec{B}_0 \parallel \vec{e}_z$ ,  $[\hat{H}_{EZ}, \hat{s}_z] = 0$ , so  $\hat{H}_{EZ}$  and  $\hat{s}_z$  share the two eigenfunctions  $|\uparrow\rangle$  and  $|\downarrow\rangle$ . The energies of the corresponding states are  $E_{EZ}^{\pm} = \pm \frac{1}{2} \mu_B g B_0$  (see Figure 3.2), and their difference is the Zeeman splitting:

$$\Delta E_{EZ} = \mu_B g_e B_0 \quad (3.2)$$

The measurement of the magnetic moment of an electron can be done by measuring its Zeeman energy. The local molecular environment affects the electron's magnetic moment through spin-orbit coupling which can be seen as a deviation in the electron's  $g$  factor [9].

**Nuclear Spin and Nuclear Zeeman Splitting** A proton has a half-integer spin  $S = 1/2$  that results in a magnetic moment  $\mu_p = \mu_e \frac{m_e}{m_p}$ , that is  $\frac{m_p}{m_e} \approx 1836$  times smaller than the electron's magnetic moment. A neutron bears no charge but also has a half-integer spin  $S = 1/2$ . An atomic nucleus that consists of protons and neutrons has a magnetic moment which is a vector sum of the aligned spins of its protons and neutrons. The spin of a nucleus is defined by the arrangement of its nucleons and by the nuclear charge. A nitrogen nucleus has 7 protons and 7 neutrons that total in a nuclear spin  $I = 1$  which, with the  $g$  factor for the nitrogen nucleus  $g_N$ , results in the nuclear magnetic moment of  $\mu_N = \mu_B \frac{m_e}{m_N} g_N I$  that splits each of the electron Zeeman level into three nuclear Zeeman energy sublevels corresponding to the three possible projections of the nuclear spin on the magnetic field axis,  $m_I = -1, 0, +1$ , analogously to the electron with  $m_S = 1/2, -1/2$ . The two splittings are shown in the energy diagram in Figure 3.1. The nuclear Zeeman splitting is more than two orders of magnitude weaker than the electron Zeeman splitting because of the difference in the masses of the particles.

**Hyperfine Interaction** The magnetic moments of an electron and a magnetic nucleus, such as nitrogen, couple in the hyperfine interaction:  $H_{HF} = \vec{s}\mathbf{A}\vec{I} = H_F + H_{DD}$  with the hyperfine coupling tensor  $\mathbf{A}$ . The isotropic part  $H_F = a_{iso}\vec{s}\vec{I}$ , or the Fermi contact interaction, scales with the probability density of the electron at the position of the nucleus  $a_{iso} = \frac{2\mu_0}{3\hbar} g_e \mu_e g_n \mu_n |\psi(0)|^2$  [?]. The anisotropic part  $H_{DD} = \vec{s}\mathbf{T}\vec{I}$  with the dipolar coupling tensor  $\mathbf{T}$  takes into account the anisotropic magnetic dipole coupling between the magnetic moments of the electron and the nucleus.  $\mathbf{T}$  depends on the shape of the electron orbital, its  $3 \times 3$  Cartesian matrix representation depends on the molecular frame of reference and can be diagonalized by rotating the coordinate system. The matrix representation of the hyperfine coupling tensor  $\mathbf{A}$  can be written in as the sum of its isotropic and anisotropic parts:  $\mathbf{A} = a_{iso}\mathbb{1}_3 + \mathbf{T}$  [106]. In its diagonal matrix representation  $\mathbf{A}$  reduces to its three principal components  $[A_{xx}, A_{yy}, A_{zz}]$ . The values of  $\mathbf{A}$  are typically given in MHz.

**Exchange Interaction** In a system of closely placed electrons, such as in a film of densely packed radicals, the electron orbitals may overlap significantly and the radicals

may exchange electrons. The energy required to exchange the electrons is called the exchange coupling  $H_{exch} = \vec{s}_1 \mathbf{J} \vec{s}_2$ , that becomes considerably large at inter-spin distances below  $r < 1.5$  nm or with a large spin delocalisation [?]. The positive  $\mathbf{J}$  corresponds to a weak coupling between  $s_1$  and  $s_2$  which leads to an antiferromagnetic or antiparallel alignment of spins with a total  $S = 0$ , whereas the negative  $\mathbf{J}$  causes the strong inter-spin coupling which leads to a ferromagnetic alignment with  $S = 1$  [?].

**Nuclear Quadrupole Moment** The nitrogen nucleus has a spin greater than 1/2 which alters the charge distribution within the nucleus which gives rise to a non-vanishing nuclear electrical quadrupole moment  $Q$  [93]. The interaction between the asymmetrically distributed charge and the gradient of the electric field at the nucleus is given by the nuclear quadrupole Hamiltonian  $H_{NQ} = \vec{I} \mathbf{P} \vec{I}$  with the nuclear quadrupole tensor  $\mathbf{P}$  that describes the coupling of the nuclear quadrupole moment to the electric field gradient.

**The Spin Hamiltonian** For the interactions considered in this thesis, the following Hamiltonian will be applied to describe the interactions of unpaired electron spins with their local environments, ranging by their magnitude:

$$H = H_{EZ} + H_{HF} + H_J + H_{NZ} + H_{NQ} \quad (3.3)$$

The electron Zeeman term  $H_{EZ}$  defines the requirements on the hardware and sets the range of the magnetic fields used in the spectroscopic experiments. The hyperfine interaction term  $H_{HF}$  allows for reconstruction of the hyperfine coupling tensor from the recorded spectra which is used as a marker to identify the molecular structure and dynamics of the mobile molecular fragments that are released during the operation of an electrochemical cell. The exchange interaction term  $H_J$  scales with the concentration of the electrons, so the information about  $\mathbf{J}$  can be used to characterize the packing of the molecular fragments in the electrode. The nuclear quadrupole interaction term may lead to spectral distortions in a highly charged cathode where electric fields may be sufficiently strong to introduce noticeable nuclear quadrupole couplings to the nitrogen nuclei.

### Energy Diagram of the Spin Hamiltonian

#### 3.1.2 cwEPR Instrumentation

First observed in 1944 [116, 115, 91], the phenomenon of electron paramagnetic resonance had quickly become a tool for probing local molecular environments in species that contain

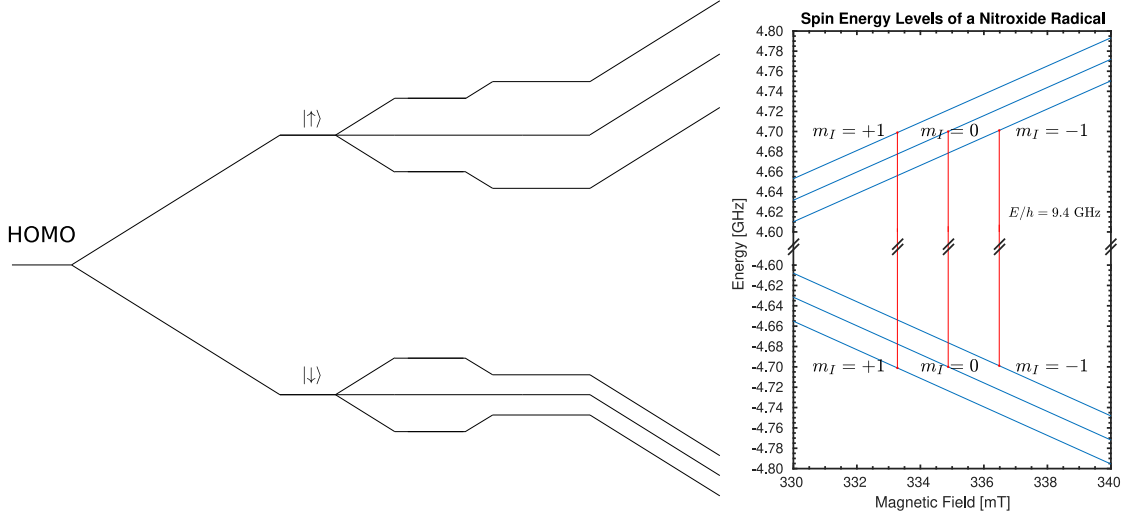


Figure 3.1: Energy diagram of the spin Hamiltonian showing the contributions of the individual terms.

unpaired electron spins. A free electron, that does not interact with its environment and has  $g = g_e$ , experiences a Zeeman splitting of  $\Delta E = g\mu_B B_0$ , that corresponds to the energy of a photon with a frequency of  $\nu = \Delta E/h$ . A microwave photon can drive a magnetic dipole transition between the Zeeman-split spin states - this is called electron paramagnetic resonance (EPR). An X band microwave photon (IEEE X band,  $\nu = 8 - 12$  GHz,  $\lambda = 2.5 - 3.8$  cm, Figure 3.2, left) can drive the magnetic dipole transition between  $|\uparrow\rangle$  and  $|\downarrow\rangle$  at  $B_0 \approx 0.3$  T. In a continuous-wave electron paramagnetic resonance (cwEPR) experiment, the microwave frequency and power is kept constant while  $B_0$  is scanned and the microwave absorption is observed. EPR happens around the  $B_0$  values given by the spin resonance condition:

$$\mu_B g_e B_0 = h\nu \quad (3.4)$$

When  $B_0$  reaches the value that satisfies Eq. 3.4, the sample starts absorbing microwaves. The absorbed microwave power recorded as a function of  $B_0$  is the cwEPR spectrum (Figure 3.2, right, dashed). By construction, cwEPR spectrometers typically record the derivative of the microwave absorption vs.  $B_0$  (Figure 3.2, right, solid). Advanced spin resonance techniques methods that involve coherent spin dynamics and pulsed microwave fields are discussed in Chapter 4.

**cwEPR spectrometer** A basic cwEPR spectrometer consists of a magnet, a microwave source, a resonator and a microwave detector. Figure 3.3 depicts those elements with more

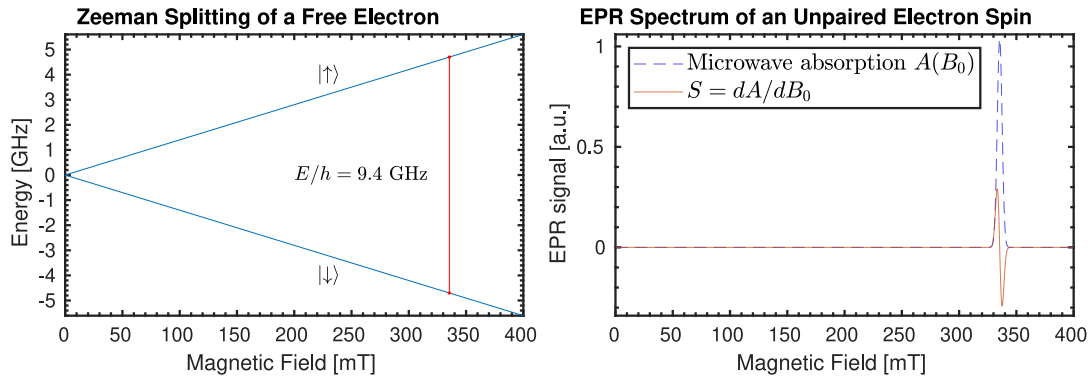


Figure 3.2: Left: Zeeman splitting for the energies of the two states of an isolated electron spin in a static magnetic field computed with EasySpin [99]. Vertical line is the magnetic dipole transition driven by a 9.4 GHz microwave photon. Right: Microwave absorption and its derivative as a function of the static magnetic field for an unpaired electron spin with a 5 mT Gaussian broadening to show the realistic shape of the cwEPR spectrum.

details, including the sample - an electrochemical cell that is placed inside the microwave resonator and its SoC controlled with an external potentiostat.

Continuous microwaves are generated with a klystron (MW source in Figure 3.3) and directed towards the resonator (resonating cavity) through the signal arm that contains a variable attenuator and a circulator. The circulator directs the microwaves from the source to the cavity and passes the microwaves reflected from the cavity further to the microwave detector. The adjustable coupling iris between the circulator and the resonating cavity allows one to match the impedance of the cavity to the impedance of the signal arm so that minimal microwave power is reflected back from the cavity at a non-resonant field  $B_0$ . That impedance matching is called critical coupling. At the microwave detector, the microwaves reflected from the cavity are compensated by the microwaves with fixed microwave power and an adjustable phase, that pass through the reference arm. The signals from the two arms interfere destructively at the detector, so that there is no signal at the detector for non-resonant  $B_0$ .

When the resonance condition (Eq. 3.4) is met, the incident microwaves are being absorbed by the sample and the resonator's  $Q$  factor slightly changes. The change in the  $Q$  factor decouples the resonator from the signal arm, that causes additional reflections in the signal arm. The microwaves in the signal arm that are not compensated by the reference arm become detected by the microwave detector - a biased semiconductor diode that has a linearly changing conductivity in the range corresponding to the incident microwave power. A phase sensitive detection with shallow modulation of  $B_0$  increases the signal-to-noise ratio (SNR) and yields the derivative of the microwave absorption profile vs.  $B_0$ . The

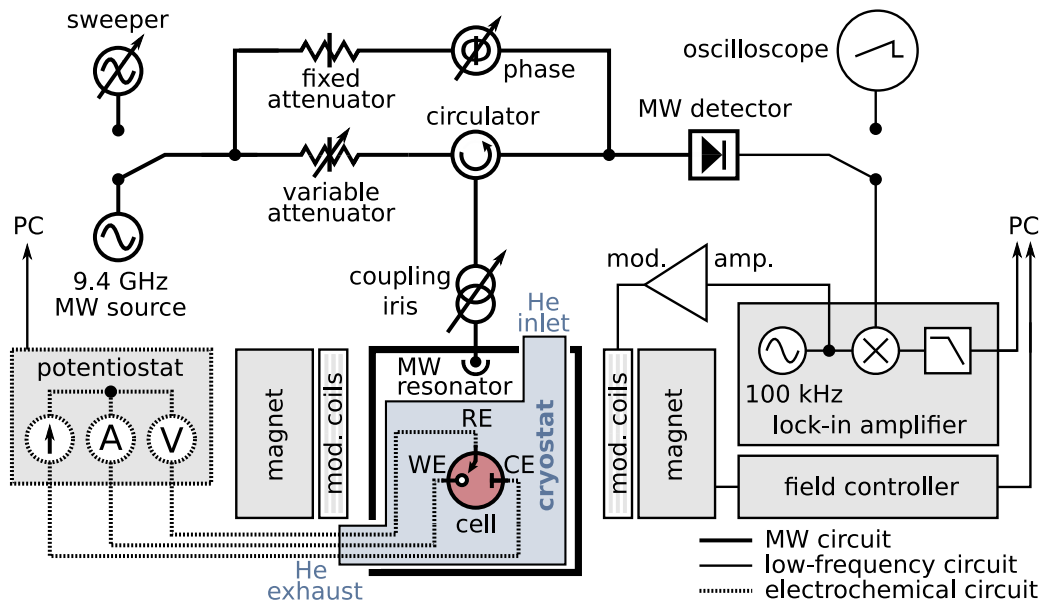


Figure 3.3: Diagram of a cwEPR spectrometer

typically high  $Q \gg 1$  factor of the resonator further increases the SNR, as the decoupling of a resonator with higher  $Q$  leads to a larger reflected microwave power.

To ensure that only the magnetic component of the microwave is interacting with the sample, a standing microwave is formed in the resonating cavity. In the center of the cavity, the magnetic component of the microwave is maximized and the electric component is quenched. When a small sample is inserted in the center of the cavity, it is mostly the magnetic component of the microwave that is interacting with it. That allows one to drive magnetic dipole transitions without heating up the sample by the electric component. For larger samples as, for example, working electrochemical cells, the separation between the electric and magnetic microwave components does not hold within the full sample volume. Furthermore, the insertion of a cell containing metal electrodes and polar electrolyte into a resonator changes the distribution of the microwave field in it and lead to a non-resonant microwave absorption.

**Line Broadening** The lines in the EPR spectra have finite widths. The lines of the liquid samples are broadened mostly by the dynamic effects (relaxation, tumbling, chemical exchange), while the lines of solid state samples are broadened by static effects (orientational disorder, unresolved hyperfine splittings, distributions in  $\mathbf{g}$ ,  $\mathbf{A}$ , and  $\mathbf{D}$  values) [99].

According to the stochastic, gaussian random modulation theory of exchange narrow-

ing, the width of a strongly exchange narrowed EPR line (HWHM) is given by

$$\Delta B_0 \approx \frac{10}{3} \left( \frac{H_p^2}{H_e} \right) \quad (3.5)$$

and the resonance lineshape is lorentzian.  $H_p$  is the mean square dipolar field and  $H_e$  is an effective exchange field which is proportional to the mean exchange integral  $J$  [79]

## 3.2 cwEPR Spectroscopy of TEMPO Containing Molecular Fragments

The stable TEMPO<sup>•</sup> radical is widely used in the EPR spectroscopy as a spin probe and particularly in the EPR studies of TEMPO containing ORB materials [70, 74, 4, 3, 48, 120]. The spin density at the TEMPO<sup>•</sup> radical is localized within the N-O bond [81] and partially resides on the  $I = 1$   $^{14}\text{N}$  nucleus, so to describe the EPR spectrum of an isolated TEMPO<sup>•</sup> one has to take into consideration the electron Zeeman term  $H_{EZ}$ , the nuclear Zeeman term  $H_{NZ}$  and the hyperfine coupling term  $H_{HF}$ . The unpaired electron spin on TEMPO<sup>•</sup> has anisotropic g value, because of the asymmetry of its molecular orbital, so the  $\mathbf{g}$  matrix and the  $\mathbf{A}$  hyperfine coupling tensor are both anisotropic.  $\mathbf{g}$  is diagonal in the molecular frame of reference shown in Figure 3.4. Its principal values are  $[g_{xx} = 2.009, g_{yy} = 2.006, g_{zz} = 2.002]$  [63, 8]. The principal values of  $\mathbf{A}$  in the same frame are  $[A_{xx} = 20, A_{yy} = 20, A_{zz} = 100]$  MHz [63, 8].

### 3.2.1 Room Temperature Spectra of TEMPO<sup>•</sup> Solutions

Solution spectra of radicals are showing averaged values of  $g$  and  $A$  because of the fast molecular tumbling [63, 10]. The observed  $g$  value for a tumbling TEMPO<sup>•</sup> is the average of the principal values of the  $\mathbf{g}$  matrix:  $g = 1/3(g_{xx} + g_{yy} + g_{zz})$ . The anisotropic part of the hyperfine coupling tensor for the tumbling TEMPO<sup>•</sup> also averages to zero, so only the isotropic hyperfine constant  $a_{iso}$  determines the observed hyperfine coupling. CwEPR spectra of a 0.1 mM solution of TEMPOL measured at room temperature are shown in Figure ???. The spectral simulation performed with EasySpin [99] yields  $g = 2.0055$  and  $a_{iso} = 43.8$  MHz.

A biradical molecule like Di-Tempo-Salen (Figure 2.8 e) and f)) has two paramagnetic species that are close to each other and therefore exchange electrons. When the exchange coupling between the radicals  $J$  is comparable to the hyperfine coupling  $A$  of each radical to its 'host' nucleus, the superhyperfine interaction [] takes place, in which the radical is

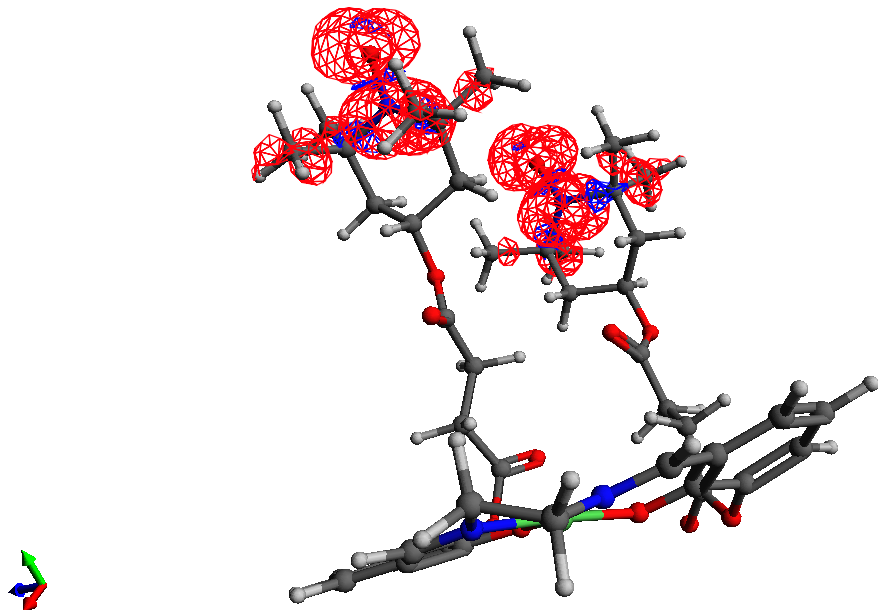


Figure 3.4: DFT on DiTS showing spin density on two neighboring TEMPO groups. The spin density is localized around the Nitrogen nucleus that gives rise to the hyperfine coupling. Calculation by Marcel Gauglitz.

interacting to the nucleus of the neighboring radical [19]. Solutions of biradical molecules with magnetic nuclei show more features in cwEPR spectra when the electron-electron exchange coupling  $J$  between the two radicals within the molecule becomes comparable to the hyperfine coupling between the radical and its 'host'  $^{14}\text{N}$  nucleus. tumbling of the molecule and the restricted motions of each radical within the molecule cause a complex molecular motion that affects the dipolar and exchange couplings between the radicals and causes "spectra with alternating linewidths" [19, 9]. A solution of Di-TEMPO-Salen shows a five-line cwEPR spectrum with alternating linewidths (Figure 3.5, right) with the three most intense lines corresponding to the three hyperfine sublevels of  $\text{TEMPO}^\bullet$ . The five-line structure in the cwEPR spectrum indicates the presence of a di-TEMPO biradical in the solution.

#### TOLYAN:

If the TEMPO groups are far away from each other, their cw-EPR signal consists of three lines that are due to the hyperfine interaction between the electron spin and the spin of

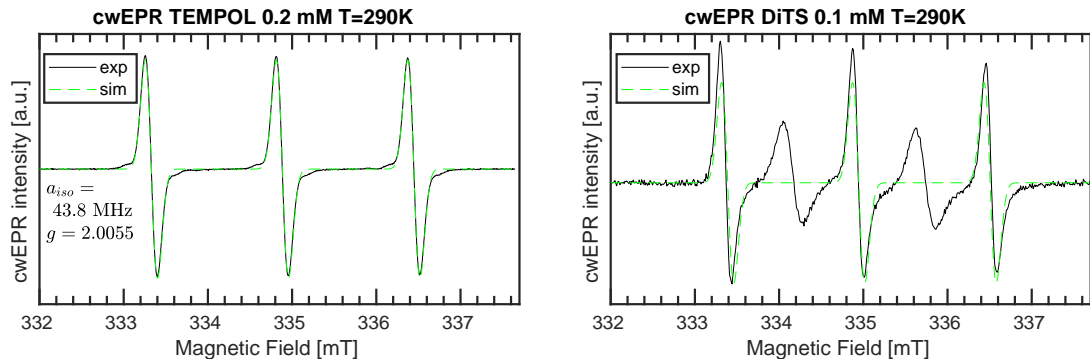


Figure 3.5: Room temperature cwEPR spectra of a low-concentration solutions containing mono- and di-TEMPO molecular fragments. Left: TEMPOL, Right: Di-Tempo-Salen.

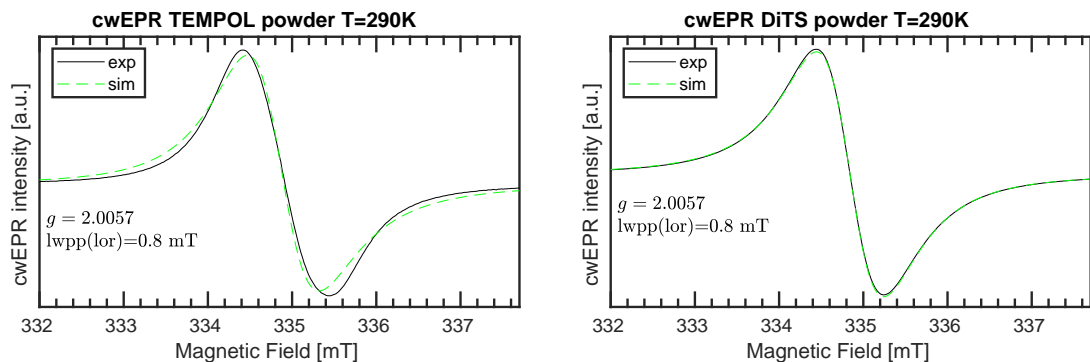


Figure 3.6: Room temperature cwEPR spectra of pure TEMPO-containing powders. Left: TEMPOL, Right: Di-Tempo-Salen.

the Nitrogen nucleus. When the TEMPO groups are brought closer to each other, their electron orbitals start to overlap, and the exchange interaction ( $J$ ) between the electrons grows. That splits the signal into more lines as it was shown by [10] and represented in Fig. 7. In the case of strong exchange interaction the spectrum consists of five lines with relative ratios 1:2:3:2:1. In the absence of the exchange interaction the spectrum contains only three hyperfine lines of equal intensities. In DiTS, a sum of a three-line spectrum and a five-line spectrum was observed. This may be the evidence that TEMPO-bearing linkers are sufficiently long to allow TEMPO groups to move freely in space around the organometallic complex. That can yield to different  $J$  values depending on the relative orientation of the linkers, similar to [10]. In theory, there are several possible positions of TEMPO groups relative to each other that can change the EPR spectrum. Depending on the angle between the linkers (from  $\pi$  to 0),  $J$  may vary from its minimal to maximal

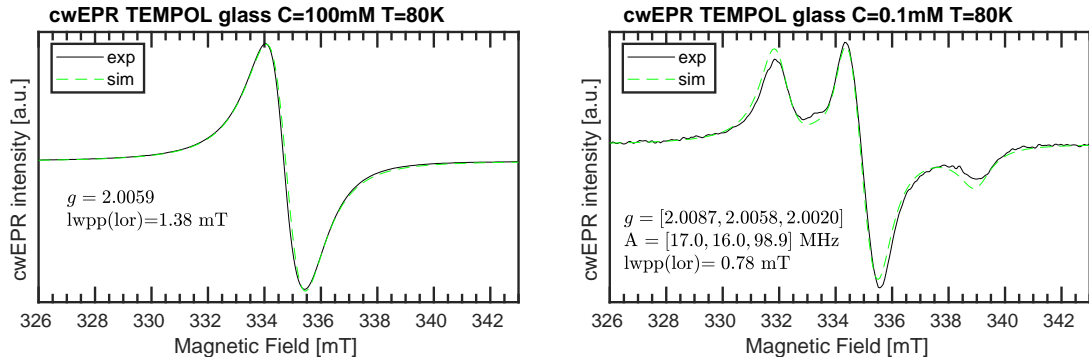


Figure 3.7: Cryogenic cwEPR spectra of TEMPOL at high and low concentration in a Dichloroethane/Acetonitrile glass. Left: 100 mM, Right: 0.1 mM.

value, that should yield a three- and five-line structures respectively. Since the process of movement is dynamic, we can explain the observed picture as a combination of several positions in space [10]. The five-line structure suggests different preferred conformations of the TEMPO fragments and dynamic interconversion between these states with different exchange coupling  $J$  leads to the observed spectrum.

### 3.2.2 Spectra of $\text{TEMPO}^\bullet/\text{TEMPO}^+$ Films

A film made of a TEMPO-containing polymer can be brought to a certain oxidation state, depending on how many of the TEMPO groups are in the radical ( $\text{TEMPO}^\bullet$ ) state and how many are in the oxidized ( $\text{TEMPO}^+$ ) state. The densely packed  $\text{TEMPO}^\bullet$  fragments in the film cannot be considered as isolated molecules anymore, and the interactions between the radicals become significant. Microcrystals of TEMPOL are densely packed  $\text{TEMPO}^\bullet$  with a concentration of ??? mM. The cwEPR spectrum of TEMPOL microcrystals in Figure ?? is one broad line centered at  $g = 2.0055$ . A powder of DiTS monomers is showing the same cwEPR spectrum in Figure ?? . It is the matter of concentration of the paramagnetic TEMPO fragments that changes the cwEPR spectral shape. In Figure ?? cryogenic (80 K) cwEPR spectrum of a 100 mM solution of TEMPOL in Dichloroethane/Acetonitrile is presented. With a slight shift in  $g$  factor due to the polar molecular environment of the frozen solvent [?] and a broader lineshape due to a weaker exchange narrowing, the spectrum consists on one dipolar-broadened Lorentzian line. In contrast, when the concentration of the solution is lowered to 0.1 mM (Figure ??) - the inter-molecular interactions become weak enough to resolve the  $A$  and  $g$  anisotropy of the nitroxide radical, so the spectrum consists of three lines that can be simulated with the known  $A$  and  $g$  parameters.

A redox-active film containing TEMPO radicals, like the TEMPO-Salen cathode film,

shows different cwEPR signatures depending on its redox state. Figure 3.8 represents two cryogenic cwEPR spectra of a  $d \approx 2.2\text{ }\mu\text{m}$  DiTBuS cathode film that was discharged to  $E = -50\text{ mV}$  and charged to  $E = +900\text{ mV}$  vs. the Ag/AgNO<sub>3</sub> RE as described in Section 2.2.2. The spectral intensities were normalized to represent the signal shape not the magnitude. The discharged film shows one broad cwEPR line in Figure 3.8, left, that reflects on the strong interactions between the non-oxidized TEMPO<sup>•</sup> in the discharged cathode. The linewidth of the discharged film spectrum is smaller than the linewidth of the DiTS monomer spectrum, suggesting a smaller exchange interaction between the TEMPO fragments in the film [?].

The oxidized film in Figure 3.7, right, shows a well resolved spectrum of an isolated nitroxide, similar to the low-concentrated solution of TEMPOL (Figure ??). A series of powers was recorded for both redox states of the film to observe possible microwave saturation effects that are crucial for the pulsed EPR experiments discussed in Chapter 4.

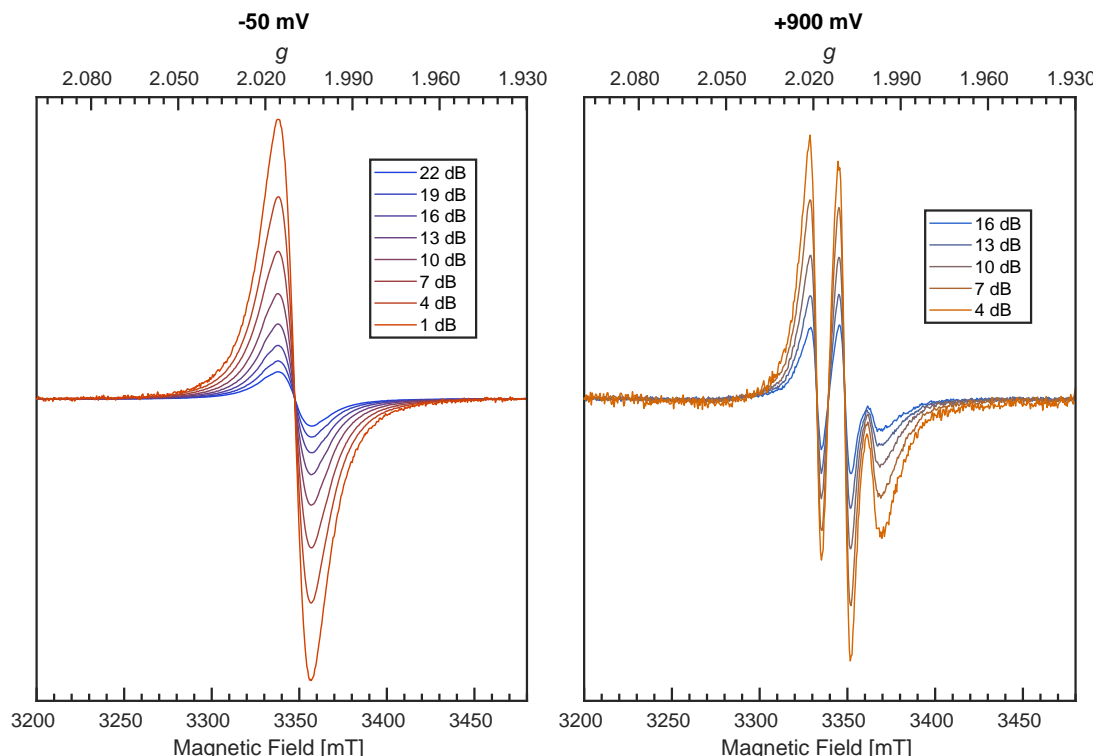


Figure 3.8: Cryogenic (80 K) cwEPR spectra of a pDiTBuS film grown with 200 deposition cycles. Left: discharged film, -50 mV vs. Ag/AgNO<sub>3</sub> RE. Right: Fully charged film, 900 mV vs. Ag/AgNO<sub>3</sub> RE.

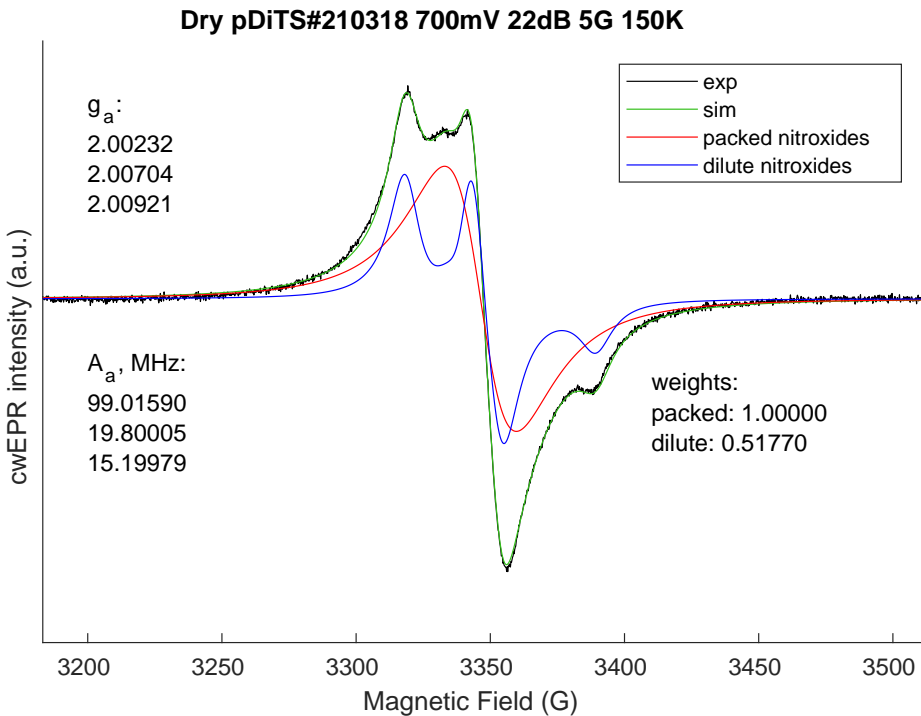


Figure 3.9: A pDiTS film in the intermediate state of charge (700 mV vs. Ag/AgNO<sub>3</sub>) showing a composition of two spectral signatures. The single-line signal from the densely packed nitroxide radicals coexists with the signal of the isolated nitroxide radicals. Two-component simulation.

### 3.2.3 Spectra of NiSalen Films

The molecular backbone of pDiTS and pDiTBuS is the pNiSalen, a conjugated polymer that exhibits redox behavior [18, ?, 2]. The observations of electrochromicity of pNiSalen films with UV-VIS spectroscopy [18] have revealed the formation of polarons and antiferromagnetically coupled (with total spin S=0) bipolarons in the oxidized state of pNiSalen. A series of cwEPR spectra recorded for a pNiSalen film in various redox states is shown in Figure 3.12. Operando cwEPR spectra of a cell containing a pNiSalen cathode is shown in Figure 3.13.

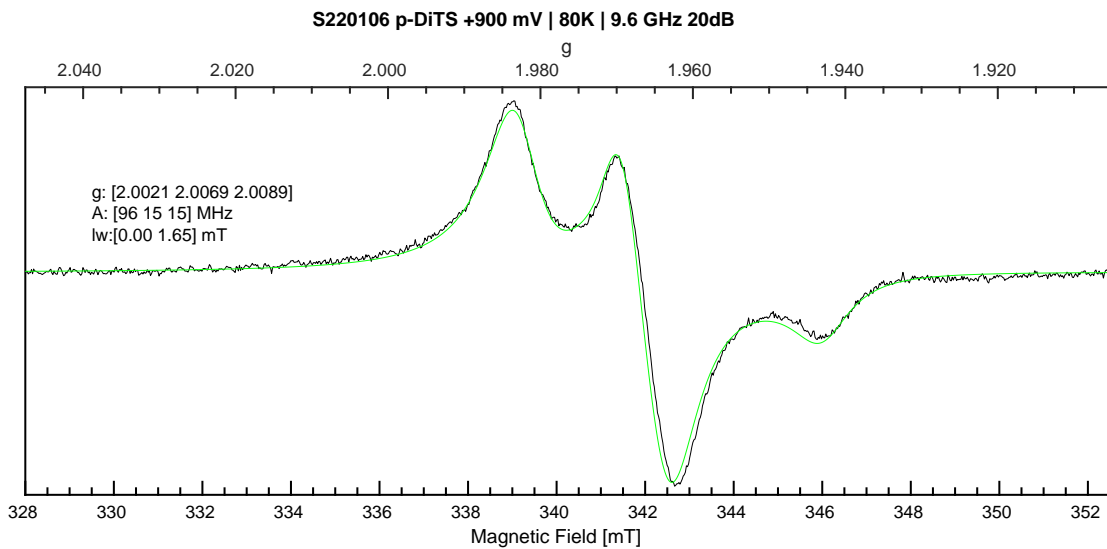


Figure 3.10: Cryogenic (80 K) cwEPR spectrum of an oxidized pDiTBuS film grown with 200 deposition cycles showing a signature of the isolated nitroxide radical with the standard  $g$  and  $A$  parameters, revealed with a simulation.

### 3.3 cwePR Spectroscopy of a Charging Electrochemical Cell

There is a number of difficulties when it comes to an EPR experiment on a working electrochemical cell. The cell must contain mobile ions between its electrodes - cations and anions. The ions are normally produced as products of dissociating salts. To overcome the ionic bond in a salt and to break it into the ions, a solvent with large dipole moment is needed. Solvents with large dipole moments, as acetonitrile ( $\text{CH}_3\text{CN}$ ,  $\epsilon \approx 37.5$ ) or water ( $\epsilon \approx 78.4$ ), have large dielectric constants which results in a non-resonant absorption of microwaves. A cell containing liquid electrolyte absorbs microwaves and lowers the sensitivity of the EPR experiment. Furthermore, due to a finite dimension of cell, not only the magnetic component of the microwave is interacting with the electrolyte, but also the electric one - this results in heating of the electrolyte in a similar fashion as in a microwave oven. The heating of the electrolyte leads to a faster degradation of the cell and does not allow for long systematic measurements.

Another general issue with the operando EPR and EDMR experiments is that the device under testing (DUT) has to have metal electrodes that deliver current to it. Metals, placed in a microwave cavity, change the distribution of the electromagnetic field in it - that

weakens the magnetic component at the device and at the same time strengthens the electric component. It is the magnetic dipole transition that is causing the magnetic resonance, so the weakening of the magnetic component by introducing the metal electrodes further decreases the magnetic resonance response. The increased electric component causes heating to temperatures that can be critical for the DUT operation.

## 3.4 Fabrication of EPR-compatible Electrochemical Cells

### 3.4.1 Versatile electrode setup for ex-situ and in-situ spectroelectrochemical EPR

There is increasing interest in both ex-situ and in-situ spectroelectrochemical (SEC) EPR measurements in research fields ranging from biology to materials science, from redox active systems such as proteins [1] and hydrogenase to catalysis,[56, ?, ?, ?, ?] redox-flow batteries [?] and of course ORBs.[41, ?] One significant drawback with SEC EPR is the fact that microwave resonators suffer from substantial microwave damping as a result of introducing metal electrodes, polar solvents and ionic salts (i.e., the electrolyte) needed for successful electrochemistry.[?] Microwave damping can be significantly reduced by our novel on-substrate electrode design (see Fig. 3.14) as this limits the amount of metal that is introduced into the resonator, while still allowing us to have electrode surface areas large enough to deposit sufficient material of interest to observe EPR signals.

The on-substrate electrodes are produced as follows. Cleaned quartz substrates are placed inside a holder and covered with shadow masks. The assembly is transferred into a vacuum chamber equipped with a thermal evaporator (MBraun ProVap 5G PVD System). At a pressure of  $7 \times 10^{-7}$  mbar, 10 nm of Chromium (Cr) adhesion layer is evaporated, followed by 180 nm of Gold (Au). In this way the on-substrate working and counter electrodes are formed (WE and CE respectively). The reference electrode (RE) is not evaporated on substrate for electrochemical stability reasons. Instead, a 250  $\mu\text{m}$  Ag wire is used, either as is or, for additional stability, coated galvanically with a AgCl layer.[?] See Section ?? in the ESI† for details of the sample preparation.

The above procedure provides a WE active area of 12.0  $\text{mm}^2$  which allows one to deposit an electrochemically active film that is large enough to yield a clear EPR signal. The flat electrode design provides the possibility to increase the WE area for samples with particularly small EPR signals while still maintaining certain film thicknesses. This also allows for studying EPR properties as a function of film thickness. In cases where the electrochemical process is thought to deposit material on both the WE and CE, the distance between the on-substrate electrodes can be adjusted such that only one of the electrodes

is positioned in the active volume of the microwave resonator, allowing for selective EPR probing of either of the electrodes.

The on-substrate electrodes reduce microwave damping. However, a substantial amount of microwave damping occurs due to the electrolyte, made of polar solvent and ionic salts. Therefore, we further optimize our setup by modifying conventional 5 mm outer diameter (OD) quartz EPR tubes by flattening the bottom 1.3–1.6 cm (cf. Fig. 3.14b and Section 3.15 in the ESI†), thereby reducing the active electrolyte volume needed to submerge both the WE and CE on the substrate as well as the RE wire, from ~120  $\mu\text{L}$  to ~60–70  $\mu\text{L}$ .

The flattened tube and the thin-film electrode setup have an additional benefit in that the sample is moved away from the maximum of the electric field distribution in the Bruker ER 4122-SHQE resonator (TE<sub>011</sub> mode cavity for cwEPR), thereby further increasing the resonator quality factor (Q-factor, given by  $Q = \frac{\nu_{res}}{\Delta\nu}$ ,  $\nu_{res}$  = resonance frequency,  $\Delta\nu$  = FWHM of the resonance dip) and hence sensitivity. Further improvements can be made using the flat electrode setup in a TM<sub>110</sub> mode cwEPR cylindrical cavity such as a Bruker ER 4103-TM (developed for studying samples exhibiting high dielectric constants), where the flattened cell can be aligned to further reduce coupling to the microwave electric field. The modified tube is compatible with commercial Bruker ER 4118X-MD5 resonators, most commonly used for advanced pulse EPR measurements at X-band frequencies ( $\nu = 9 - 10$  GHz).

### 3.4.2 Fabrication of the modified tube

The volume of the cell used in this study had to be minimized, as the high dielectric constant of the electrolyte does not allow for the critical coupling of the resonator. The volume of the electrolyte was minimized by flattening the tip of the quartz (melting point  $T_m = 1660 - 1710^\circ\text{C}$ ) tube accommodating the cell. For that, a tungsten (W,  $T_m = 3420^\circ\text{C}$ ) rod of a 3.70×1.35 mm rectangular cross section, narrowing to the bottom of the tube at a wedge angle of  $\alpha \approx 5^\circ$ , was inserted into the tube (Fig. 3.15). The tube was evacuated and filled with He to a pressure of 100 mbar. The tip of the evacuated tube was molten around the thermally expanded rod with a Hydrogen-Oxygen burner ( $T_f = 3080^\circ\text{C}$ ). The modified tube was then connected to atmosphere and the cooled, contracted rod was removed and later reused for modifying other tubes. The tungsten rod was fabricated from an electrode of a flash lamp of a pulsed Nd:YAG laser.

The modification of the tip of the tube provided a decrease in the volume of the electrolyte down to 45  $\mu\text{L}$ , while the cylindrical part of the tube allowed for fitting the substrate connector and the wiring in. That allowed for the room temperature EPR measurements on the electrochemical cell during charging and discharging. Extensive care had to be taken

to reproduce the cv curve in the modified tube as the limited volume of the electrolyte was distributed over the large surface area. That caused poor ionic transport in the electrolyte layer.

To establish the extent to which the modified tube improves the resonator Q-factor (Q) and therefore sensitivity of the cwEPR experiment, cwEPR spectra and associated Q-factors were recorded for a flat-electrode p-DiTS cell assembled in two different sample tubes. For both cell setups we used enough electrolyte to submerge all three electrodes. This required  $100 \mu\text{L}$  for the standard tube and  $70 \mu\text{L}$  for the modified tube. The effect of the two tubes on the cwEPR spectrum and on the Q-factor was studied for a range of heights ( $H$ ) measured from the center of the microwave resonator to the middle of the WE.

### 3.4.3 Q-factors and cwEPR spectra for p-DiTS in standard and modified tube

We determine  $Q \approx 7800$  for the empty resonator. Inserting the tube-based cells initially at  $H = 24$  mm reduces the Q-factor for both cases, but more significantly for the standard tube ( $Q_{\text{standard tube}} \approx 4200$ ,  $Q_{\text{modified tube}} \approx 5400$ , see Fig. 3.16). At  $H = 18$  mm the Q-factor drops for both, again more significantly for the standard tube to  $Q_{\text{standard tube}} \approx 300$  while for the modified tube it is still  $Q_{\text{modified tube}} \approx 1200$ , a factor of 4 difference. This difference between the two tubes shows the benefit of using the modified tube and flat electrode geometries for SEC EPR. When the modified tube is inserted as deep as  $H = 14$  mm, the  $Q_{\text{modified tube}}$  is around 400, which still allows for EPR measurements. Coupling the resonator not possible for  $H < 18$  mm (standard tube) and  $H < 14$  mm (modified tube).

The decreasing Q-factor is not the only effect of a high-dielectric sample in an EPR resonator. The interaction between the sample and the electric field distribution of the resonator causes a mixture of absorption and dispersion signals, leading to asymmetric lineshapes in the cwEPR spectra. This makes double integration of the derivative cwEPR signal more complex, thereby making a quantitative analysis more difficult. This effect can be seen in the cwEPR spectra of p-DiTS (Fig. 3.16) measured in the standard 5 mm tube for  $H = 18$  mm where the cwEPR signal is asymmetric. The modified tube yields symmetric lineshapes at the same sample heights. Further details are presented in the following subsection.

The electrochemical cells based on the modified tube allow for higher EPR signals as compared to the normal X-band EPR tube. Fig. 3.17 represents two sets of measurements that describe the enhancement of the EPR signal for the modified tube. When the cell is inserted closer to the resonator's center, the Q factor of the resonator lowers and the EPR signal increases, because the intensity of the magnetic component of the microwave field

$B_1$  is higher in the center of the resonator. When the cells were inserted closer to the center of the resonator, the Q factor went from  $\approx 6000$  down to  $\approx 400$ , so that the microwave bridge could not be critically coupled to the resonator and no EPR measurements were possible. Depending on the volume of the electrolyte in the cell, it can be inserted more or less deep into the resonator.

The modified tube could be inserted 7 mm deeper into the microwave resonator (see Fig. 3.17). The EPR signal in the modified tube is increased as compared to the normal tube at the same height.

The modified tube also allows for larger cwEPR signal intensities as it can be inserted closer to the resonator center. The signal-to-noise ratio (S/N) for the modified tube is increased by a factor of  $\approx 6$  as compared to the standard tube, both inserted at  $H = 18$  mm. At the maximum sample insertion, the S/N is improved by a factor of  $\approx 8$  for the modified tube.

Using the modified tube we see three major benefits. Firstly, it results in much higher Q-factors and therefore sensitivity when comparing Q-factors for the same sample height. Secondly, the modified tube allows for insertion of the tube closer to the resonator center, allowing for a larger S/N and therefore requiring less averaging time for each cwEPR measurement. This is especially useful for samples where holding the potential for long periods causes unwanted effects or degradation. Thirdly, cwEPR measurements with the modified tube give symmetric cwEPR lineshapes (using the conventional procedure for critically coupling the microwave cavity, the standard tube gives an asymmetric lineshape) which allows for more straightforward quantitative analysis (spin counting), especially useful for in-situ cwEPR with varying redox potentials.

### 3.5 cwEPR Spectra During a Charge-Discharge Cycle

There are four characteristic cwEPR signatures of an electrochemical cell containing di-TEMPO-Salen polymer cathode. The well known signature of a freely tumbling TEMPO $\cdot$  exhibits three narrow lines corresponding to the three nuclear sublevels of nitrogen:  $m_I = -1, 0, +1$ .

EPR spectra of electrochemical cells with p-DiTS as active-electrode material can exhibit a variety of different signals. Before presenting and discussing the experimental results, we will provide an overview about the various characteristic cwEPR lineshapes associated with nitroxides in different environments.

Fig. 3.18a shows the spectrum expected for a *densely packed p-DiTS film* with all nitroxides in the EPR-active reduced state. The broad unstructured line results from the strong dipolar and exchange interaction between both nitroxides of each DiTS monomer as

well as between the nitroxides of different monomers. The exchange interaction can lead to either line narrowing or broadening depending on the strength of the interaction,[?] while the dipolar interaction causes broadening. In consequence, the overall cwEPR line width depends on the spin concentration in the film.

*Dilute mono-TEMPO fragments* dissolved in the electrolyte, each containing only one nitroxide, give rise to a three-line spectrum (cf. Fig. 3.18b) which is well known from nitroxide-based spin labels in solution.[63] Tumbling of the molecules in the liquid electrolyte results in an averaging of the anisotropic interaction between the electron spin and the nitrogen nuclear spin ( $I = 1$ ) as well as of the  $g$  anisotropy, leaving only the isotropic part of the hyperfine coupling and the isotropic  $g$  value.

*Dilute DiTS monomers* in the electrolyte generally give a spectrum consisting of five narrow lines (cf. Fig. 3.18c), if each monomer contains two interacting EPR-active nitroxides. The spectrum depends on dynamic effects, specifically the modulation of the exchange interaction between both radicals of each monomer. Thus, depending on the solvent and temperature, the spectrum can be indistinguishable from the three-line spectrum of mono-TEMPO fragments.

The fully charged (oxidized) p-DiTS film can contain electrically isolated domains in which the nitroxides are not connected to the electrode and cannot be oxidized or reduced. These electrically inactive *immobilized DiTS monomers* in the oxidized film display a spectrum as shown in Fig. 3.18d. In contrast to the densely packed p-DiTS film, the dipolar and exchange interactions between neighboring radicals are much weaker. The anisotropy of the nitroxide's hyperfine tensor adds features to the cwEPR spectrum in d) as compared to a). Yet, there is some remaining line broadening that does not allow one to distinguish between immobilized DiTS monomers with either one or two paramagnetic nitroxides.

We note that the oxidized NiSalen backbone can contribute to the spectrum as well. Its EPR signature, which is not shown in Fig. 3.18, is clearly different from the nitroxide/TEMPO-related spectra discussed above.

### 3.5.1 Spectral Simulations

### 3.5.2 Quantitative Analysis of Potential-Dependent EPR Spectra

The number of spins at each SoC was determined with quantitative cwEPR from the double integral of the cwEPR intensity calculated with the SpinCounting Toolbox [?] for Matlab [?]. The cwEPR spectra in Figure 3.20 were measured in a Bruker Elexsys E580 spectrometer equipped with an ER 4118 X-MD5 dielectric ring resonator with an unknown Q factor. To calibrate the intensity of the measured cwEPR signals and to determine the abso-

lute number of spins in the film, we measured the cwEPR spectrum of the fully discharged film (SoC 0%) with a calibrated spectrometer. The calibrated spectrometer is a lab-built X-band cwEPR spectrometer equipped with a 9.4 GHz, 200 mW microwave source and a 4122-SHQE resonator. With  $Q = 6095$ , the absolute number of spins in the pDiTBuS film at SoC 0% was measured to be  $N = (6.9 \pm 0.4) \times 10^{15}$ . We used  $N$  to get the number of spins for other SoC from the spectra measured with the uncalibrated spectrometer. We assumed that the Q factor of the resonator remains the same for different SoC [?] and computed the corresponding numbers of spins from the doubly integrated spectral intensities.

The doubly integrated cwEPR spectral intensities for the pDiTBuS film in the four considered SoC relate to each other as 100:51:15:6 with the absolute number of spins of  $(6.9 \pm 0.4) \times 10^{15}$ ,  $(3.5 \pm 0.2) \times 10^{15}$ ,  $(1.1 \pm 0.1) \times 10^{15}$  and  $(3.8 \pm 0.4) \times 10^{14}$ , respectively. The respective ESOC are therefore  $(0 \pm 5)\%$ ,  $(49 \pm 3)\%$ ,  $(85 \pm 2)\%$  and  $(95 \pm 1)\%$ . Spin concentrations in the film are  $(5.3 \pm 2.7) \times 10^{20}$ ,  $(2.7 \pm 1.4) \times 10^{20}$ ,  $(0.8 \pm 0.4) \times 10^{20}$  and  $(0.3 \pm 0.2) \times 10^{20} \text{ cm}^{-3}$ , respectively. Integration of the cyclic voltammogram yields  $(2.3 \pm 0.8) \times 10^{16}$  electrons in the reduced state.

## 3.6 EPR-Detected State Of Charge

The SoC of the film determined with Coulomb counting were compared to quantitative cwEPR to directly relate the number of charges, injected into the film upon charging, to the number of paramagnetic centres in it. We refer to the fraction of spins removed from the fully discharged film to reach a given SoC as the EPR-detected state of charge, or ESOC. The fully discharged film has the maximum number of spins and its ESOC is 0%. ESOC at other SoC are determined as the fraction of the missing spins with respect to ESOC 0%. ESOC of 95% thus corresponds to the oxidation state where only 5% of the initially present spins are left in the film. The cwEPR spectra were recorded for the listed SoC, and the corresponding numbers of spins were calculated from the double integrals of the spectra. The integrated spectra and the experimental details are shown in the ESI, Section ???. The injected charges, detected spins and ESOC values are counted for each SoC in Table 3.1. The average spin concentration in the film  $\langle n \rangle$  at each ESOC was calculated from the corresponding number of spins and the estimated volume of the film of  $(1.3 \pm 0.6) \times 10^{-5} \text{ cm}^3$ .

E [mV]	SoC	ESOC	capacity drawn [ $\mu\text{Ah}$ ]	charges injected	spins detected	$n_C$ [ $\text{cm}^{-3}$ ]	$\langle n \rangle$ [ $\text{cm}^{-3}$ ]	C [ $\text{cm}^{-3}$ ]
590 $\pm$ 5	98%	(95 $\pm$ 1)%	0.020 $\pm$ 0.005	(5 $\pm$ 1) $\times$ 10 <sup>14</sup>	(4 $\pm$ 1) $\times$ 10 <sup>14</sup>	(3 $\pm$ 2) $\times$ 10 <sup>19</sup>	(3 $\pm$ 2) $\times$ 10 <sup>19</sup>	> 1 $\times$ 10 <sup>19</sup>
500 $\pm$ 5	96%	(85 $\pm$ 2)%	0.060 $\pm$ 0.005	(1.4 $\pm$ 0.1) $\times$ 10 <sup>15</sup>	(1.1 $\pm$ 0.1) $\times$ 10 <sup>15</sup>	(1.0 $\pm$ 0.5) $\times$ 10 <sup>20</sup>	(8 $\pm$ 4) $\times$ 10 <sup>19</sup>	> 3 $\times$ 10 <sup>19</sup>
430 $\pm$ 5	65%	(49 $\pm$ 3)%	0.480 $\pm$ 0.005	(1.07 $\pm$ 0.01) $\times$ 10 <sup>16</sup>	(3.5 $\pm$ 0.2) $\times$ 10 <sup>15</sup>	(8 $\pm$ 4) $\times$ 10 <sup>20</sup>	(3 $\pm$ 2) $\times$ 10 <sup>20</sup>	—
-200 $\pm$ 5	0%	(0 $\pm$ 5)%	1.360 $\pm$ 0.005	(3.05 $\pm$ 0.01) $\times$ 10 <sup>16</sup>	(6.9 $\pm$ 0.4) $\times$ 10 <sup>15</sup>	(2 $\pm$ 1) $\times$ 10 <sup>21</sup>	(5 $\pm$ 3) $\times$ 10 <sup>20</sup>	—

Table 3.1: EPR-detected state of charge, Coulomb counting and the corresponding spin concentrations in a galvanostatically discharging pDiTBuS film with  $I = -10 \mu\text{A}$ . The electric potential of the film  $E$  was measured with respect to the Ag/AgNO<sub>3</sub> RE. The number of injected (negative) elementary charges and the corresponding concentration of charges  $n_C$  were determined from the drawn capacity. The average spin concentration  $\langle n \rangle$  is the ratio between the number of spins measured with quantitative cwEPR and the volume of the film determined by integrating the cyclic voltammogram. C is the local spin concentration in the film estimated with pEPR as described in text.

### 3.6.1 Formation of Singlet Spin States in a Reduced Cathode Film

## 3.7 Monitoring of Degradation Processes

The operando monitoring of EPR spectra in pDiTS cells has revealed that the amount of paramagnetic species reduces upon the cycling. The cwEPR spectra during one charge-discharge cycle of two different pDiTS cells are shown in Figure 3.23. Both datasets show a significant amount of the three-line structure in the oxidised (fully charged) state, that corresponds to the release of dilute nitroxide radicals from the polymer film to the electrolyte. The fact that the released species exhibit a 3-line structure and not a 5-line structure excludes the release of the di-TEMPO (DiTS) monomers and suggests that individual TEMPO<sup>•</sup> fragments are being detached from the film. Therefore, it was found that it is the molecular degradation of DiTS that is responsible for the loss of cell's capacity and not the decomposition of the polymer film into the monomer fragments. The overall EPR signal intensity decreases for both samples after the charge-discharge cycle. The spectral deconvolution with quantitative analysis of the individual components has revealed that the released fragments do not explain the overall loss of the signal intensity after the cycle.

## 3.8 Monitoring of Self Discharge

Organic Radical Batteries have a tendency to self-discharge, as the organic electrochemically active layer partially dissolves in polar electrolytes. Particularly for the TEMPO containing ORB, the dissolved, mobile TEMPO fragments serve as redox shuttles that carry the charge between the battery electrodes and cause a self discharge. The amount

of unoxidized TEMPO<sup>•</sup> shuttles can be measured with cwEPR spectroscopy as the mobile fragments have distinct spectra as compared to the fragments tightly packed in the electrode. Further in this subsection operando spectra of a TEMPO containing electrochemical cells are shown. Quantitative analysis of the released fragments during a charge-discharge cycle allows for a description of the self-discharge process in an ORB. The charge state of a battery is monitored with cwEPR and, additionally, with a potentiometric measurement to identify the self-discharge rate and to connect it with the concentration of diffusing redox shuttles. Figure 3.25 represents a gradual change in the cwEPR intensity of a self-discharging tube-based cell with a pDiTS cathode. The cell was initially discharged to  $V_{OC} = 350$  mV and then charged to  $V_{OC} = 1300$  mV, at that point the minimal cwEPR intensity was registered. The cell was left under the open circuit condition. After  $t = 500$  s, the cwEPR signal of the cell has fully recovered, that corresponds to the complete reduction of the electrochemically active nitroxide radicals in the cathode film.

### 3.8.1 Electrochemical Cells with Solid Electrolyte

The use of ionic liquids and the suitable polymer matrix allows for fabrication organic electrochemical transistors and can be used for making an all-polymer organic radical battery. PVDF was used as a polymer matrix.

### 3.8.2 Low Temperature Measurements

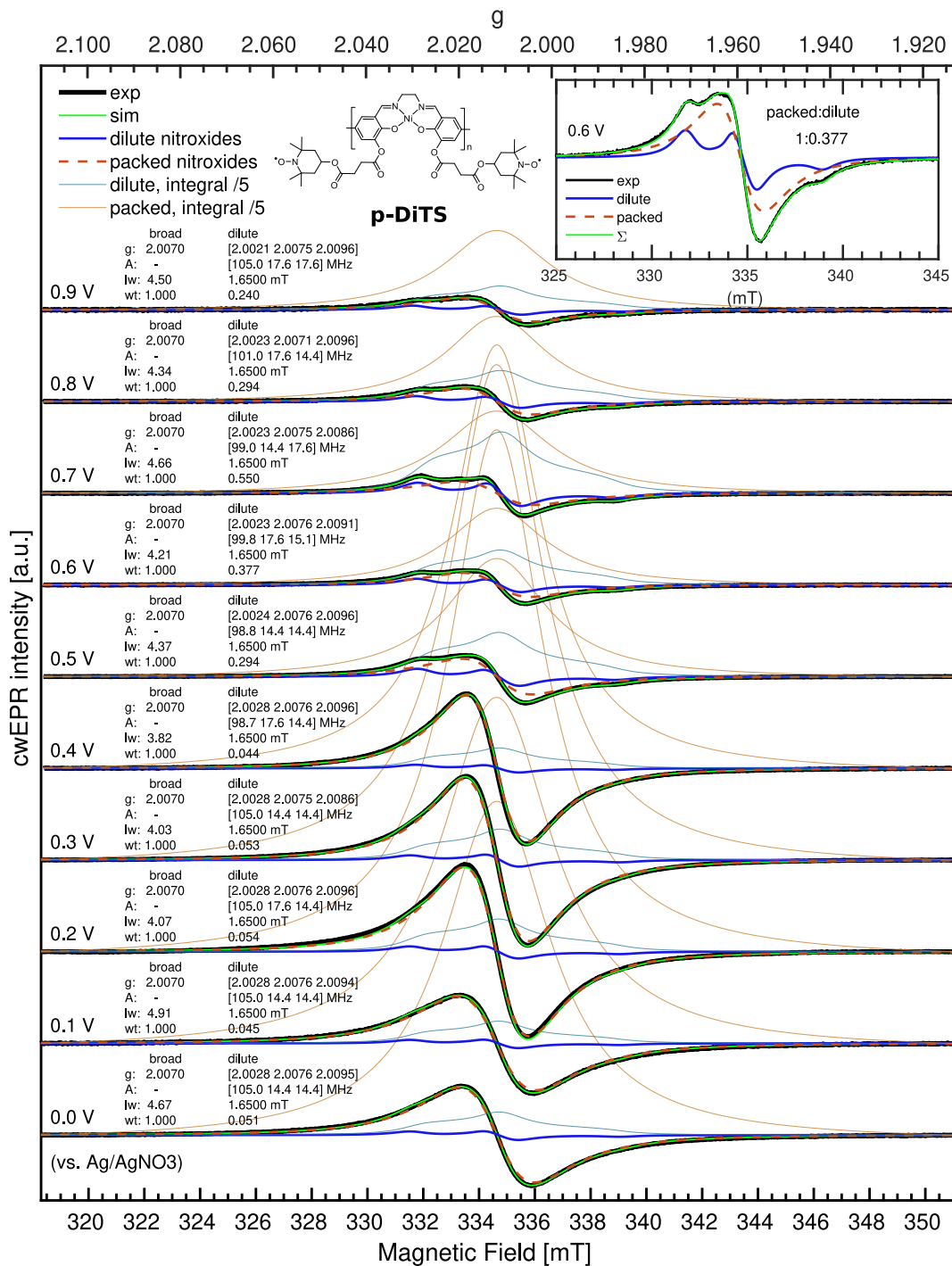


Figure 3.11: Ex-situ SEC cwEPR measurements ( $\nu = 9.4$  GHz) on a dry p-DiTS film at 150 K. Decomposition of spectra into two components with numeric simulations using EasySpin [?]: a broad Lorentzian line ( $g = 2.0070$ ,  $Iw = 4.63 \pm 1.00$  mT) and a dilute component with a hyperfine coupling to  $^{14}\text{N}$  ( $I = 1$ ,  $g = [2.00231\ 2.00711\ 2.00912]$ ,  $A = [100\ 15\ 15] \pm 5\ 2\ 2$  MHz, Lorentzian broadening with  $Iw = 1.65$  mT). The absorption profiles are shown with the integrals of the EPR signals. The ratio between the simulated components for each potential is shown by the double integrals of the components. Inset: sum of the broad and dilute components that reproduce the line shape at 0.6 V.

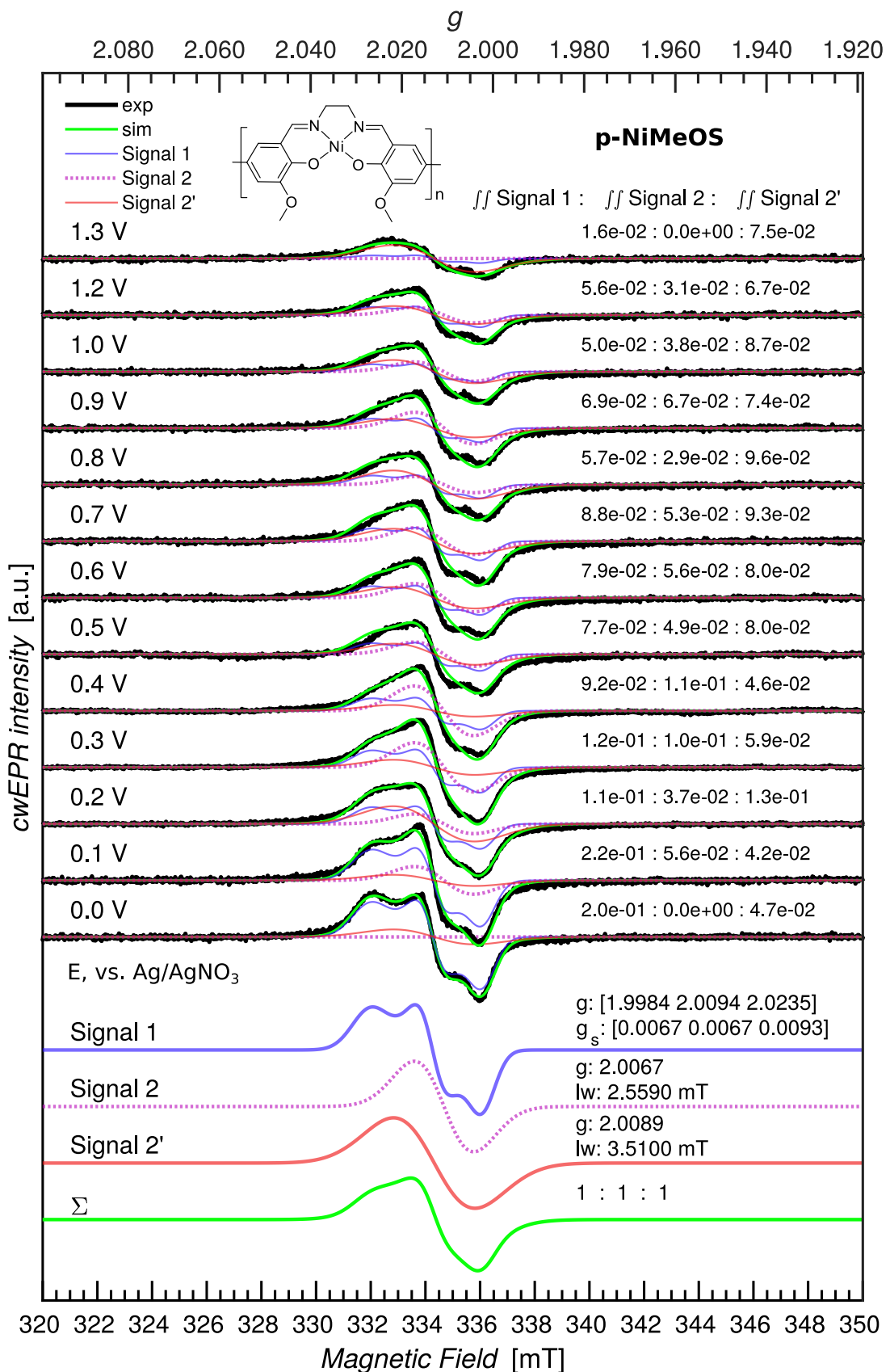


Figure 3.12: Potential-dependent cwEPR spectra of a NiMeOSalen film measured at 150 K. Simulation of the spectra with three components reported by the Timonov group.

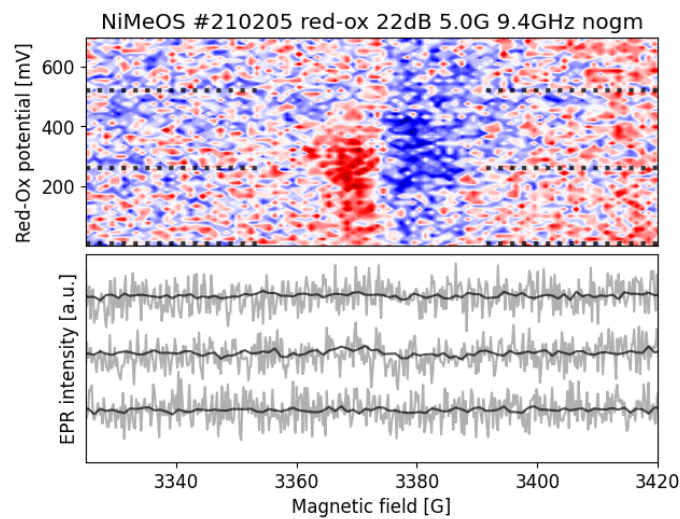


Figure 3.13: Potential-dependent operando cwEPR spectra of a NiMeOSalen cathode film measured at room temperature.

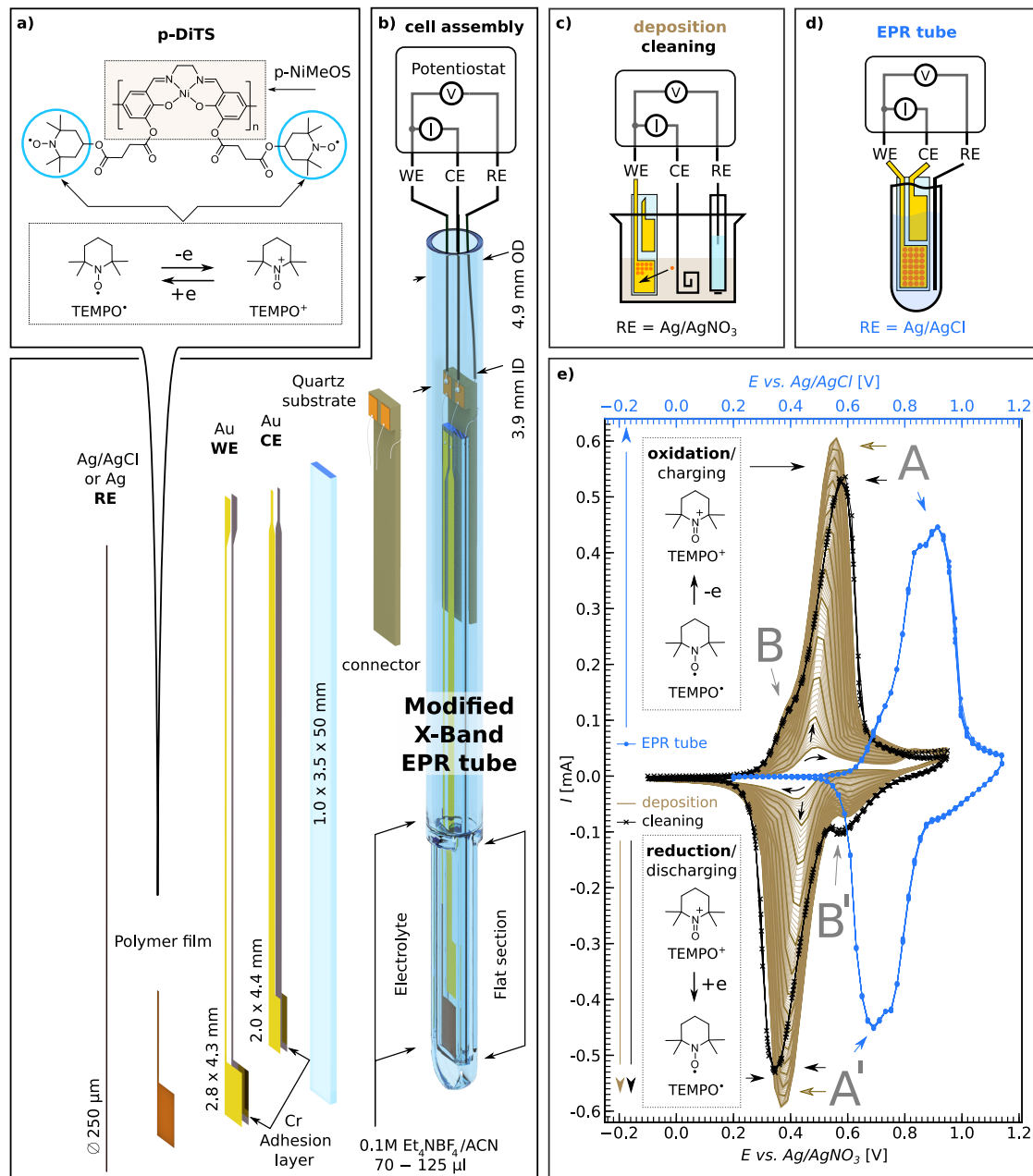


Figure 3.14: Schematic diagram of the electrode design and assembly of the electrochemical cell based on a modified X-band EPR quartz tube. a): Molecular structure of p-DiTS, with the redox reaction of its charge-bearing TEMPO groups; highlighted is the backbone, p-NiMeOSalen. b): Photograph of the modified tube with a flattened bottom section, with the on-substrate electrochemical setup assembled inside, and the process of forming the modified tube. c): Electrochemical setup for deposition and cleaning of polymer films. d): Tube-based electrochemical setup. e): Cyclic voltammograms of a growing p-DiTS film during 100 electropolymerization cycles (solid-brown), during the cleaning process (crossed-black) and in the tube-based setup (dotted-blue). Peaks A/A', B/B' correspond to the oxidation and reduction of the TEMPO fragments and of the p-NiSalen backbone, respectively. All CV were recorded at 50 mV s<sup>-1</sup>.

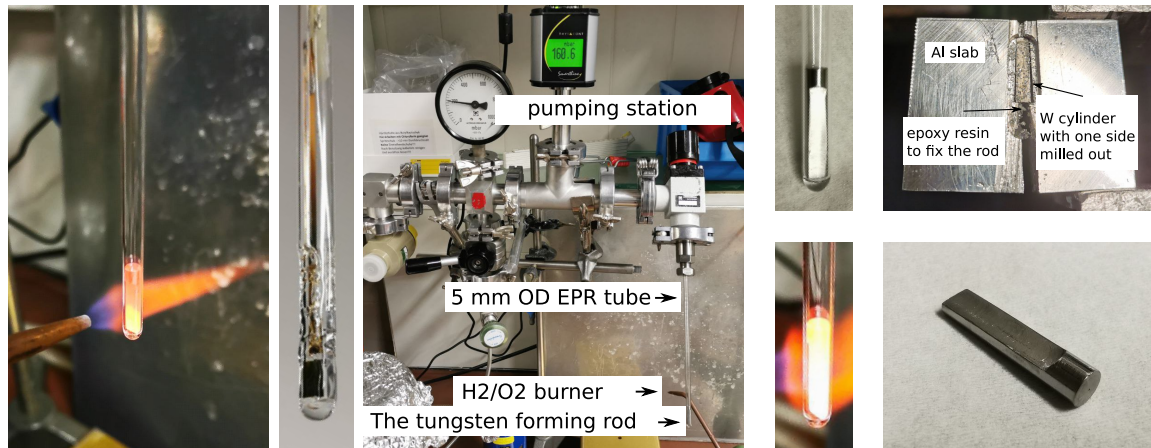


Figure 3.15: Modifying the tip of the standard 5 mm OD quartz EPR sample tube by melting it around a Tungsten (W) forming rod with a H<sub>2</sub>/O<sub>2</sub> burner in an evacuation setup.

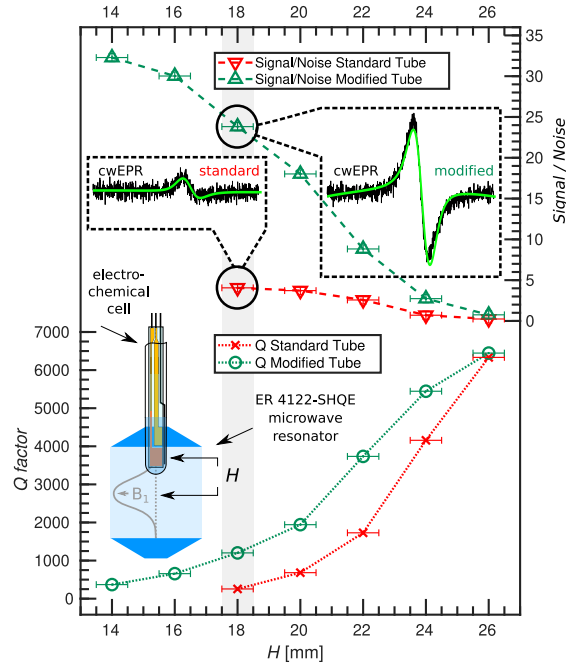


Figure 3.16: Signal-to-noise ratio of the cwEPR spectrum of p-DiTS and the Q-factor of the Bruker ER4122-SHQE microwave resonator measured for an electrochemical cell based on a standard X-band EPR sample tube and for an electrochemical cell based on the modified tube. Data for various heights  $H$  from the center of the resonator. Insets: Representative cwEPR spectra at  $H = 18$  mm, where the signal for the standard tube is the strongest.

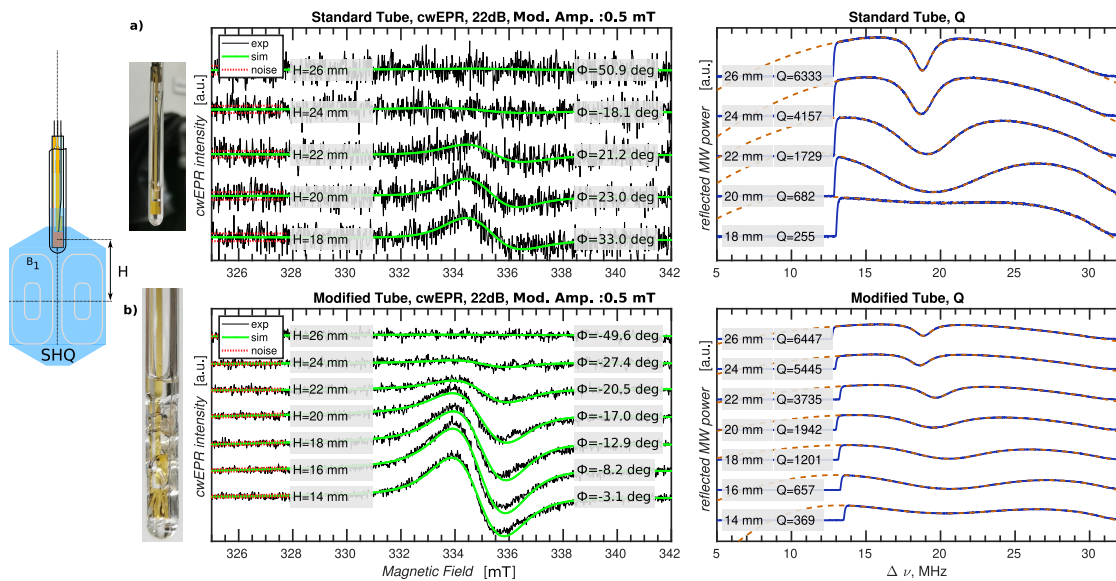


Figure 3.17: cwEPR signal intensity and Q factors for the standard 5 mm OD quartz EPR sample tube and for the modified tube at different heights from the center of the Bruker ER 4122-SHQ resonator.  $\nu = 9.4$  GHz. Simulations of the cwEPR spectra with adjusted microwave phase. Noise analysis.

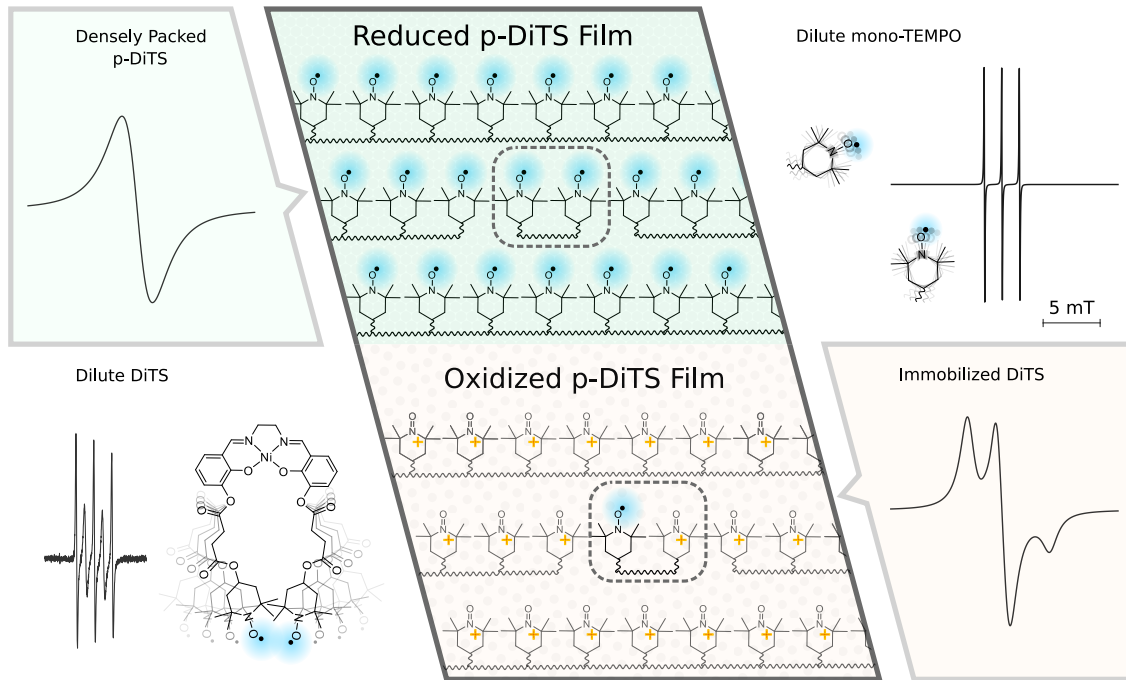


Figure 3.18: Classification of the nitroxide cwEPR spectra observed for p-DiTS under different conditions and in different environments. a): Densely packed nitroxide film with dipolar broadening and exchange narrowing or broadening giving a single derivative line. b): Typical spectrum of dilute mono-nitroxide in solution, three-lines due to  $S = 1/2$ ,  $I = 1^{14}\text{N}$  hyperfine interaction (described by isotropic  $g$ -factor and isotropic hyperfine ( $A$ ) interaction). c): Typical spectrum of tumbling di-nitroxide in solution where dynamic changes in the nitroxide – nitroxide distance modulate the exchange interaction yielding a five-line structure with alternating line width (measured cwEPR of DiTS monomers in solution at room temperature). d): Immobilized nitroxide spectrum with both  $g$  and  $A$  anisotropy.

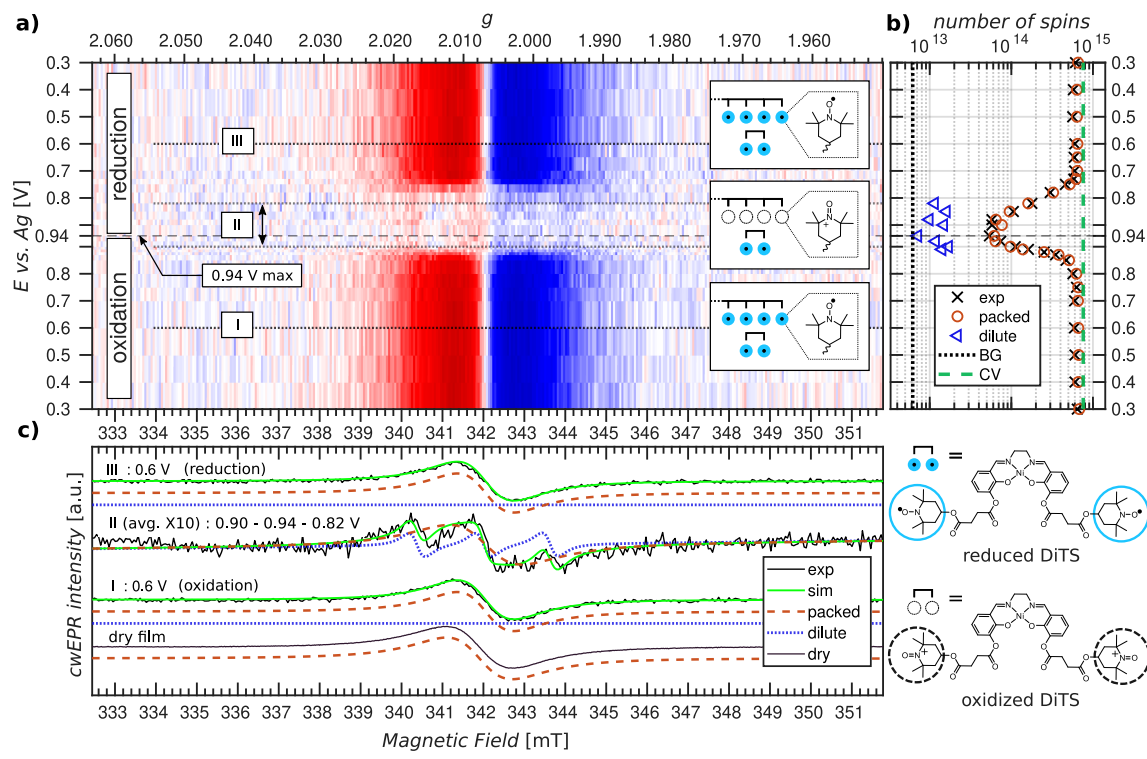


Figure 3.19: XXX

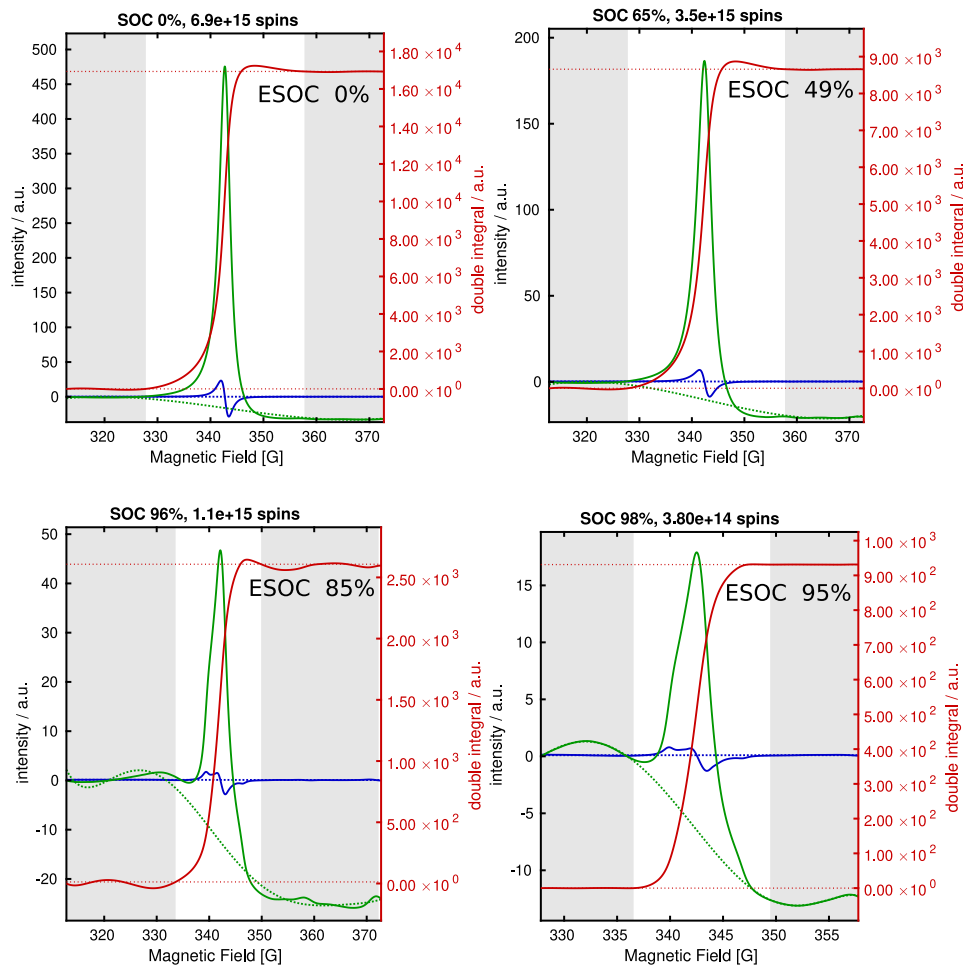


Figure 3.20: cwEPR spectra for a pDiTBuS film in four charge states. Single and double integrals of the signal. Spin count is proportional to the end value of the double integral. Temperature: 80 K,  $\nu \approx 9.6$  GHz, field modulation: 5 G at 100 kHz. ER 4118 X-MD5 dielectric ring resonator.

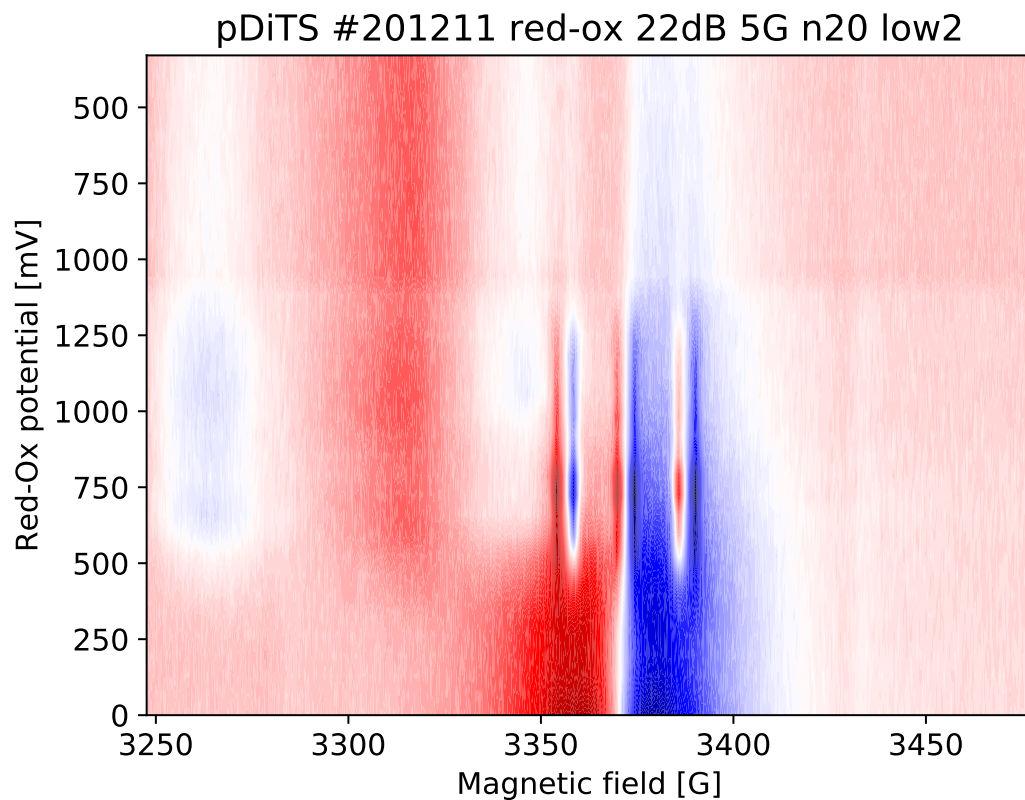


Figure 3.21: Operando cwEPR spectra of a pDiTS electrochemical cell showing irreversible release of charge-bearing fragments and decomposition of the device upon the extreme charging currents.

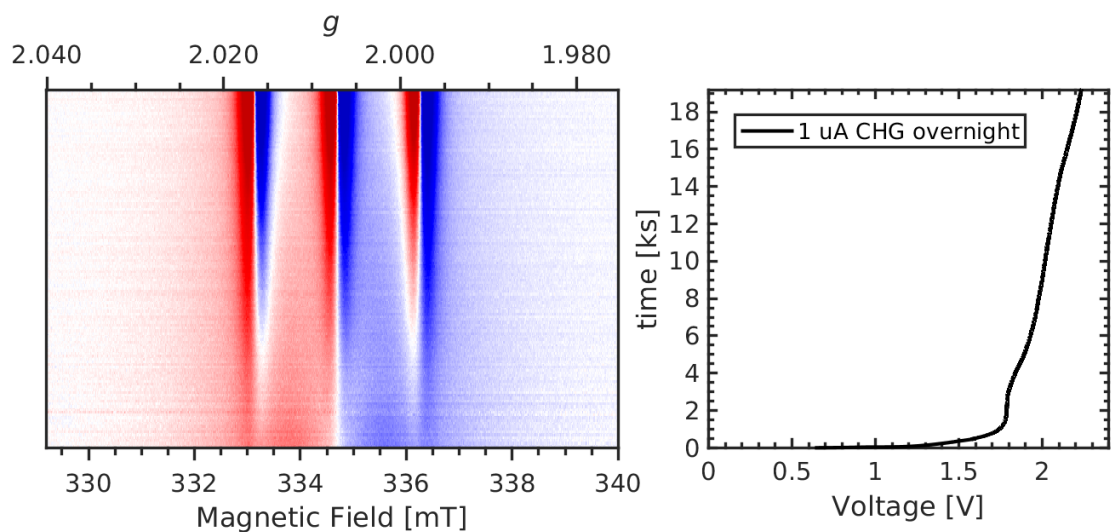


Figure 3.22: Operando cwEPR spectra of a pDiTS electrochemical cell showing irreversible release of charge-bearing fragments upon moderate charging currents.

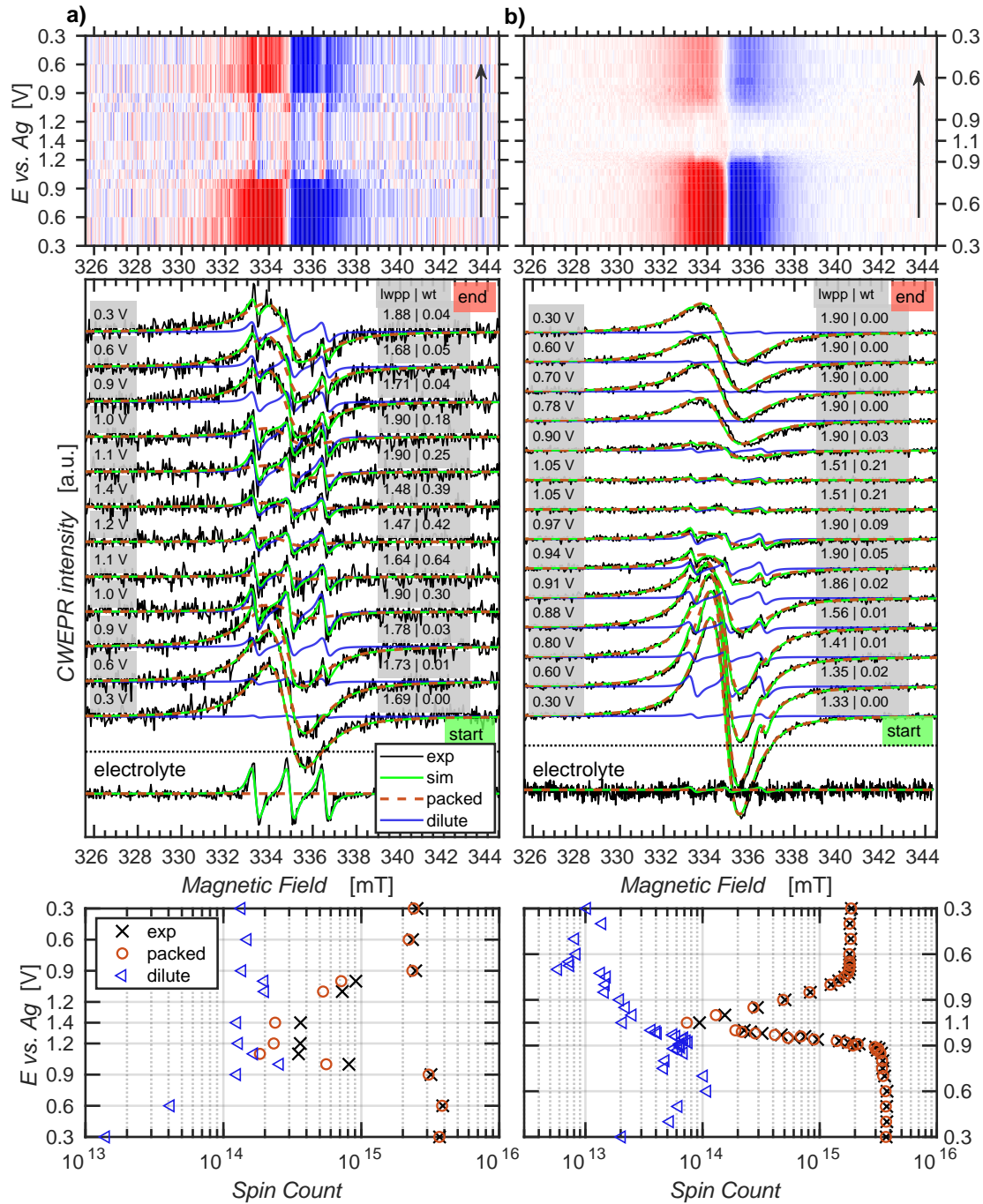


Figure 3.23: Operando cwEPR spectra of two pDiTS electrochemical cells showing release of charge-bearing fragments upon the charge-discharge cycle.

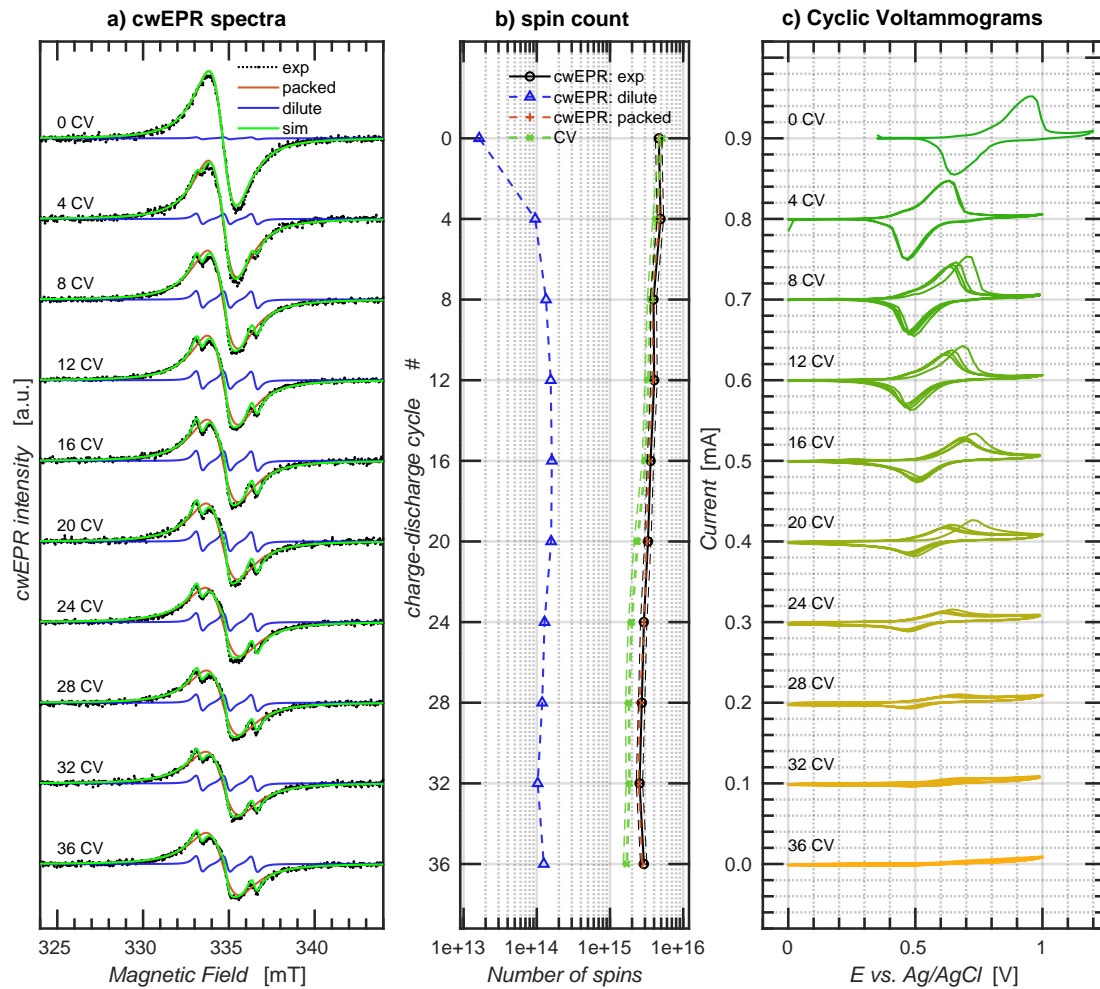


Figure 3.24: ZZZ

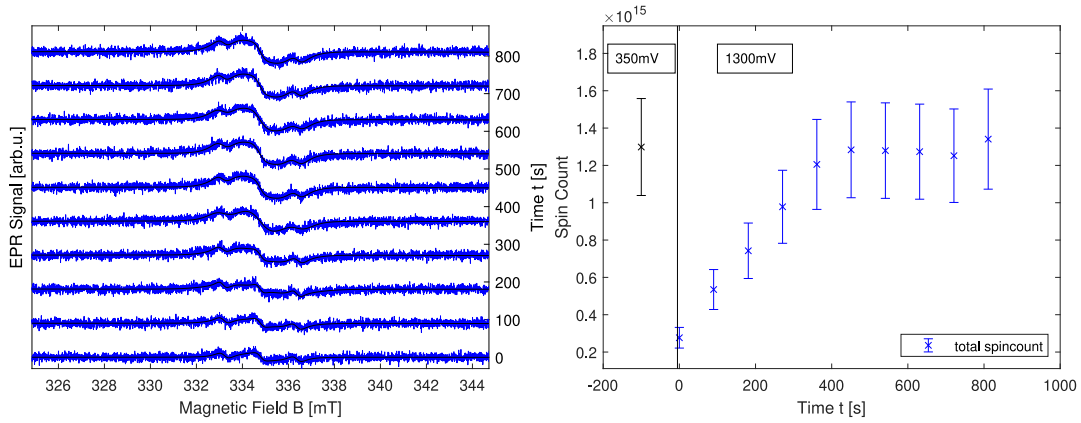


Figure 3.25: cwEPR monitored self-discharge of a tube-based cell containing a pDiTS film made with 50 deposition cycles. Left: Development of the EPR spectra of the oxidised sample over time from bottom to top; Right: Development of the spincount of the oxidised sample over time and comparison to the reduced state. [97]

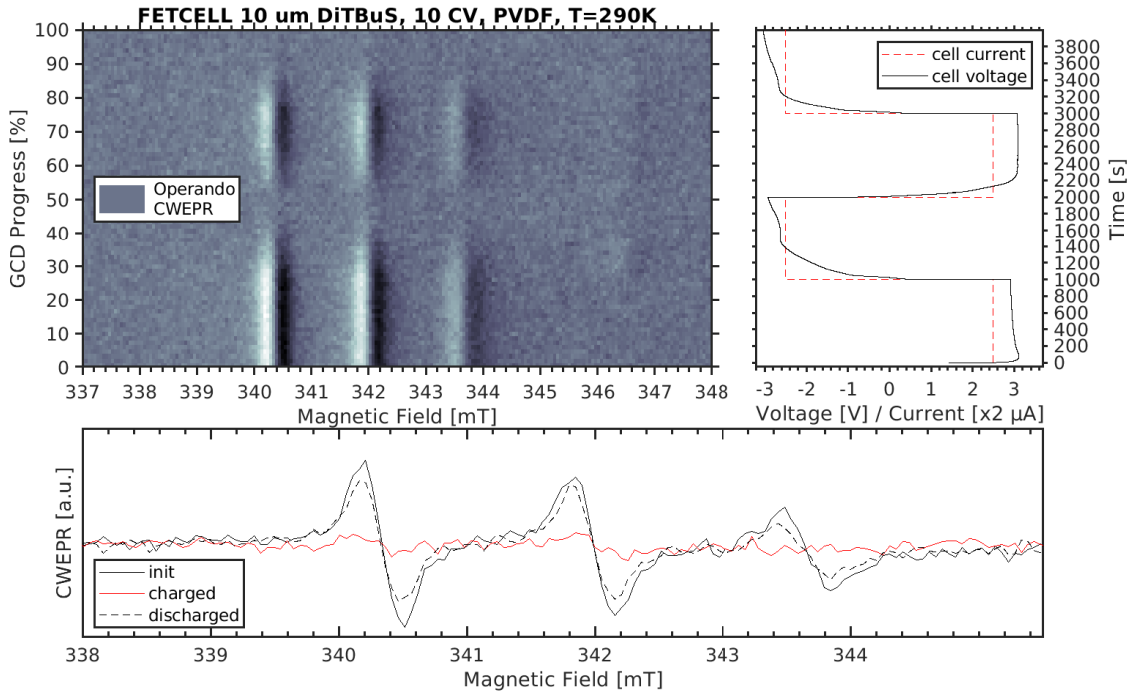


Figure 3.26: Operando cwEPR on an all-polymer organic radical battery made on a  $5 \mu\text{m}$  grid with a PVDF/TFSI gel electrolyte.

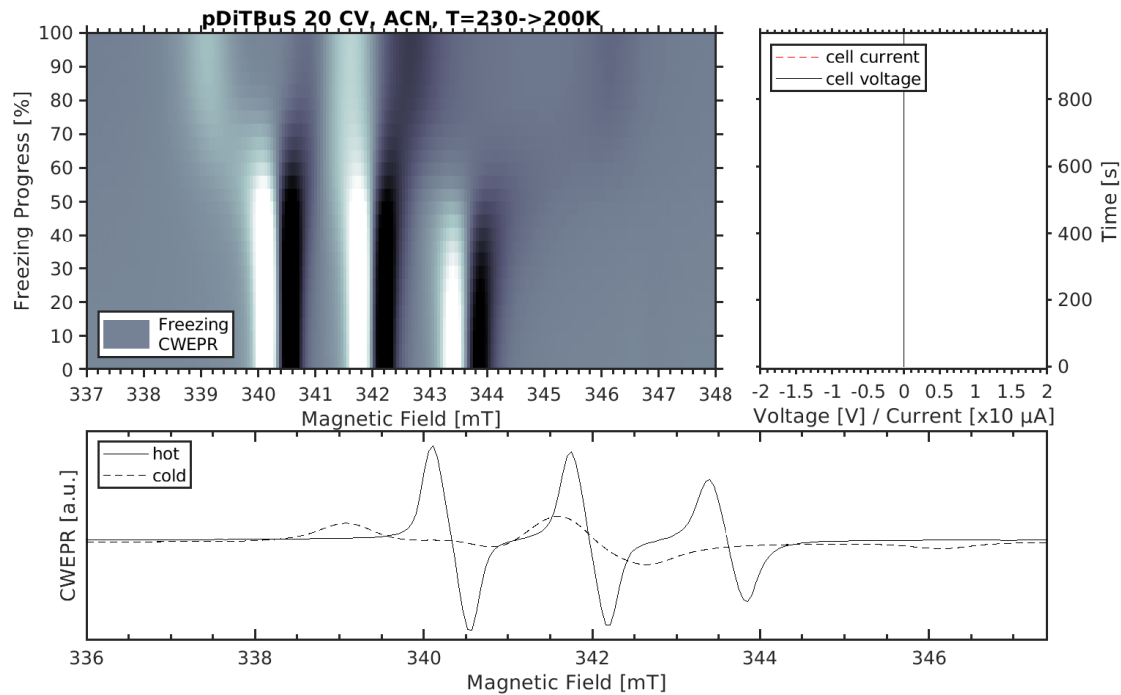


Figure 3.27: Freezing a pDiTBuS cell

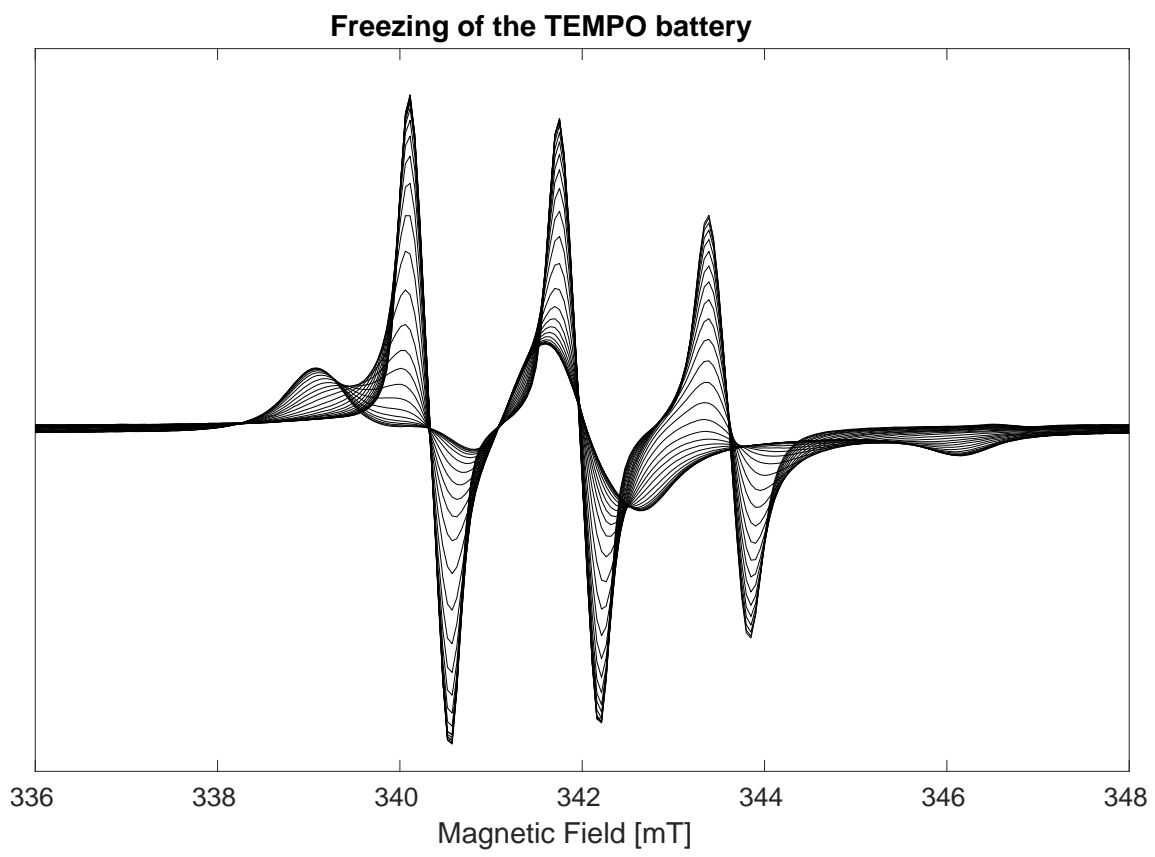


Figure 3.28: Freezing a pDiTBuS cell

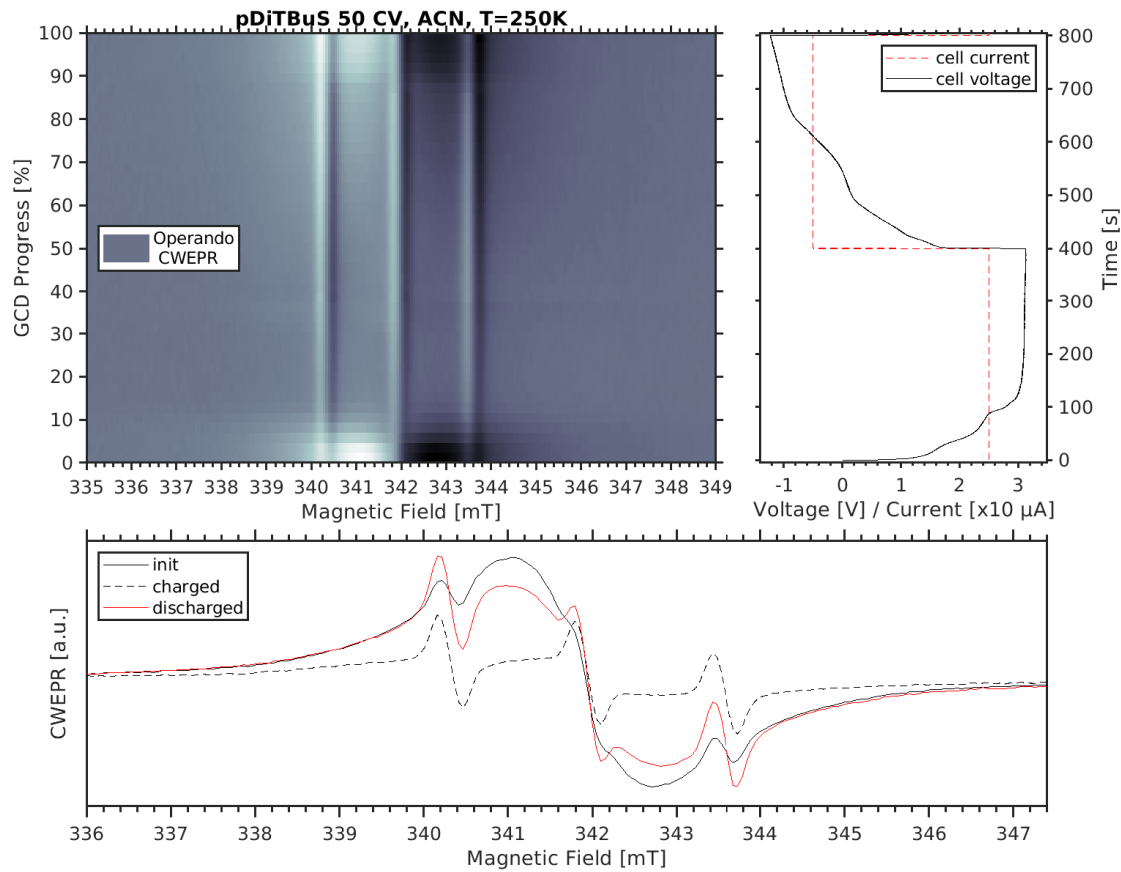


Figure 3.29: XXX

# Chapter 4

## Pulsed EPR Spectroscopy of TEMPO-containing Battery Cathodes

### 4.1 Coherent Spin Motion under Pulsed Microwave Field

The motion of the magnetization vector  $\vec{M}(t, \vec{r})$  precessing in a static magnetic field  $B_0$  is convenient to consider in the rotating frame of reference that has its  $\vec{z}'$  axis fixed to the magnetization vector  $\vec{z}' \parallel \vec{M}$  so that the  $x'y'$  plane rotates around  $\vec{M}$  at the Larmor frequency  $\omega_L = \gamma B_0$  when viewed from the laboratory frame  $\vec{x}, \vec{y}, \vec{z}$ , with  $\gamma \approx 2\pi \text{ MHz/T}$  for the gyromagnetic ratio for electrons described in Section 3.1.1. In the rotating frame, the macroscopic magnetization stays constant as long as the spin system interacts only with the static field  $B_0$ . When the spin system is excited with a linearly polarized microwave field  $\vec{B}_1(t, \vec{r}) \perp \vec{B}_0$ , its evolution is described with the set of equations that is known as the Bloch equations (Eq. 4.3). Let the microwave field of frequency  $\omega_1$  and amplitude  $B_1$  propagate along  $\vec{z}$  and be polarized in the  $xz$  plane:  $\vec{B}_1(t, \vec{r}) = B_1 \vec{x} \cos(\omega_1 t)$ . The total magnetic field  $\vec{B} = \vec{B}_0 + \vec{B}_1$  causes a time-dependent torque on the  $\vec{M}$  which leads to its precession - this time in the rotating frame of reference:

#### 4.1.1 Bloch Equations

$$\frac{dM_x(t)}{dt} = \gamma (\vec{M}(t) \times \vec{B}(t))_x - \frac{M_x(t)}{T_2} \quad (4.1)$$

$$\frac{dM_y(t)}{dt} = \gamma (\vec{M}(t) \times \vec{B}(t))_y - \frac{M_y(t)}{T_2} \quad (4.2)$$

$$\frac{dM_z(t)}{dt} = \gamma (\vec{M}(t) \times \vec{B}(t))_z - \frac{M_z(t) - M_0}{T_2} \quad (4.3)$$

### 4.1.2 Refocused Spin Echo

### 4.1.3 Spin Relaxation Times

### 4.1.4 Spin Packets

## 4.2 Pulsed EPR Instrumentation

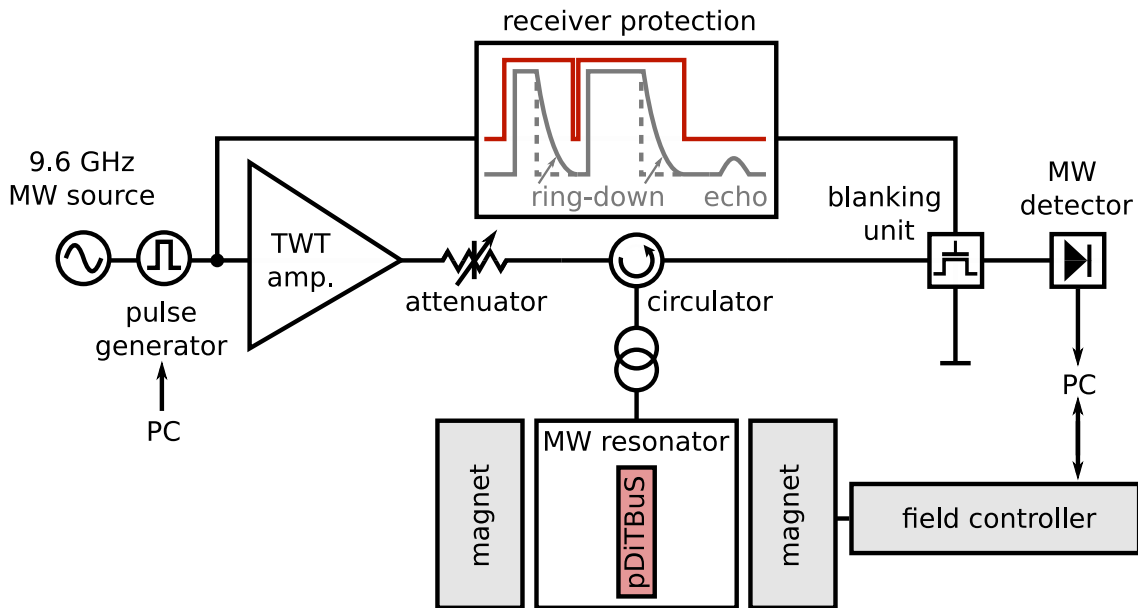


Figure 4.1: Diagram of a pulsed EPR spectrometer.

### 4.2.1 Pulse Sequences and Measurement Techniques

#### The Refocused Spin Echo Sequence

The Hahn Echo sequence consists of two pulses, the  $\pi/2$  pulse and the  $\pi$  pulse, separated in time by  $\tau$ :  $\pi/2 - \tau - \pi - \tau - echo$ . Initially, the macroscopic magnetization of the spin system is aligned along  $\vec{B}_0$ :  $\vec{M}_0 = M_Z \vec{e}_Z$ . The  $\pi/2$  microwave pulse has such length  $t_{\pi/2}$  and amplitude  $B_1$  that, during the pulse,  $\vec{M}$  nutates to the  $xy$  plane, where it keeps precessing about  $\vec{e}_Z$  after the end of the pulse. The difference in local environments for each individual spins in the spin packet, as well as the interactions between the spins, that make up  $\vec{M}$ , leads to slightly different precession frequencies  $\omega_L^i$  of the spins. After some

time  $\tau$ , the difference in the precession frequencies translates into the differences in phases so that the vector sum of the excited spins averages down to  $\vec{0}$  for sufficiently long  $\tau$ . In other words, the excited spin packet dephases with time. The dephasing due to different local spin environments can be reversible if the deviations of the precession frequencies do not depend on time, as is the case for separated electrons in an inhomogeneous solid. In such case, a  $\pi$  pulse can be applied to the spin system to flip every single spin in the dephased spin packet by 180deg in a plane containing  $\vec{e}_z$ , so that the spins keep precessing in the  $xy$  plane, but the direction of precession is inverted for them, leading to the effect that is opposite to the initial dephasing. So a  $\tau$  after the  $\pi$  pulse excites the spin packet, the accumulated phase differences become the smallest and the packet recovers its macroscopic magnetization  $\vec{M}$  that oscillates in the  $xy$  plane with  $\langle \omega_L^i \rangle$  and can be detected. The recovered  $\vec{M}$  at  $t = \tau$  after the  $\pi$  pulse is called the refocused spin echo. The difference in  $\omega_L^i$  leads to a further dephasing of the considered spin packet and to the vanishing of  $\vec{M}$ .

### Spin Echo Decay and Phase Memory Time

### Inversion Recovery and Spin-Lattice Relaxation Time

#### 4.2.2 Broad-Band Excitation and Instantaneous Diffusion

In Section /// it is shown that in a densely packed radical system, as in a TEMPO-Salen cathode film, the phase memory time can be shorter than  $T_m \leq 100$  ns. That is, the spin echo is decaying by  $e \approx 3$  times at  $t = 100$  ns. The short phase memory time limits the duration of the pulse sequence at which the echo is detectable. For a  $\pi/2 - \tau - \pi - \tau - \text{echo}$  sequence, with a hardware limitation on  $\tau \geq t_d \approx 100$  ns, the shorter pulse sequence becomes longer than  $t > 200$  ns. By this time, the spin echo decreases by  $e^2 \approx 7$  times and may be comparable to noise. The limitations imposed by the finite  $T_m$  and  $t_d$  force one to use shorter microwave pulses.

A short microwave pulse may have a spectral width comparable to the width of the observed spectrum. According to the Fourier theorem, the spectral width of a pulse is inversely proportional to the pulse length:  $\Delta\omega \sim 1/t_p$ . A spectrum of a 100 ns long rectangular pulse shown in Figure /// is //MHz wide (FWHM).

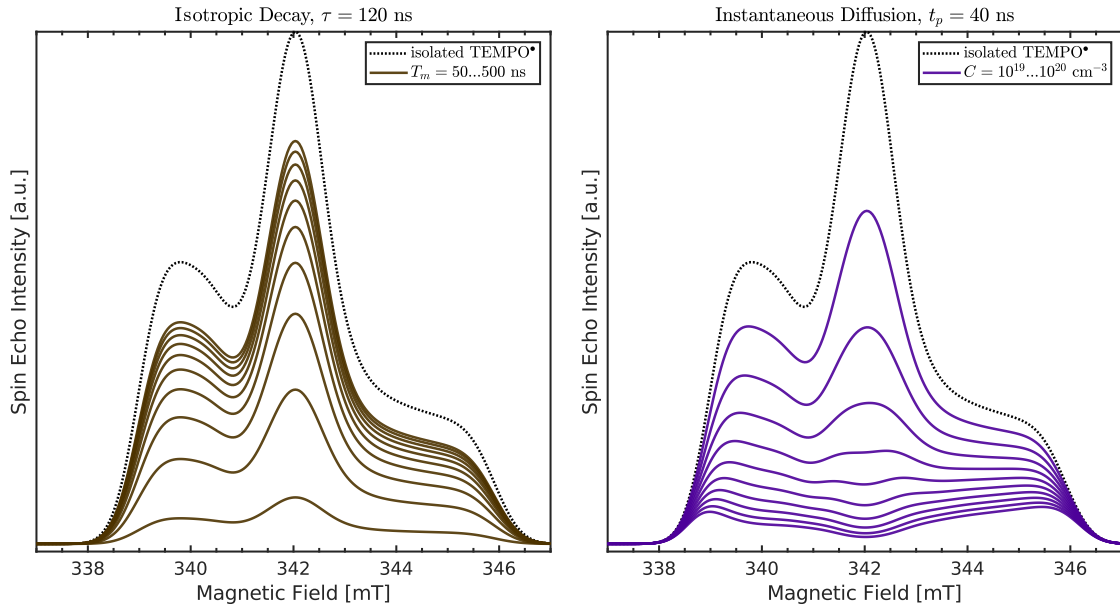


Figure 4.2: Distortions of a nitroxide FSE spectrum caused by isotropic spin relaxation (left) and instantaneous diffusion (right).

### 4.3 Pulsed EPR Spectroscopy of a charged pDiTBuS Cathode film

#### 4.3.1 Ex Situ Charging of the Cathode Films

#### 4.3.2 Field Swept Echo of a charged pDiTBuS Cathode film

#### 4.3.3 Instantaneous Diffusion in Charged pDiTBuS

We have seen that the ESOC has a strong influence on the shape of the EDFS spectra. Furthermore, the EDFS spectra of pDiTBuS are quite different from the reference spectrum of TEMPOL in a dilute frozen solution.

High spin concentration in a pDiTBuS electrode suggests strong inter-spin dipolar couplings which cause instantaneous diffusion when probed with short (broad-band) microwave pulses [102], as it was observed in a PTMA/carbon mixture [15]. Instantaneous diffusion caused by a broad-band microwave pulse shown in Figure 4.7, dashed-red, manifests itself in an additional field-dependent spin relaxation factor  $V(B_0)$ , that alters the

### 4.3. PULSED EPR SPECTROSCOPY OF A CHARGED PDITBUS CATHODE FILM 79

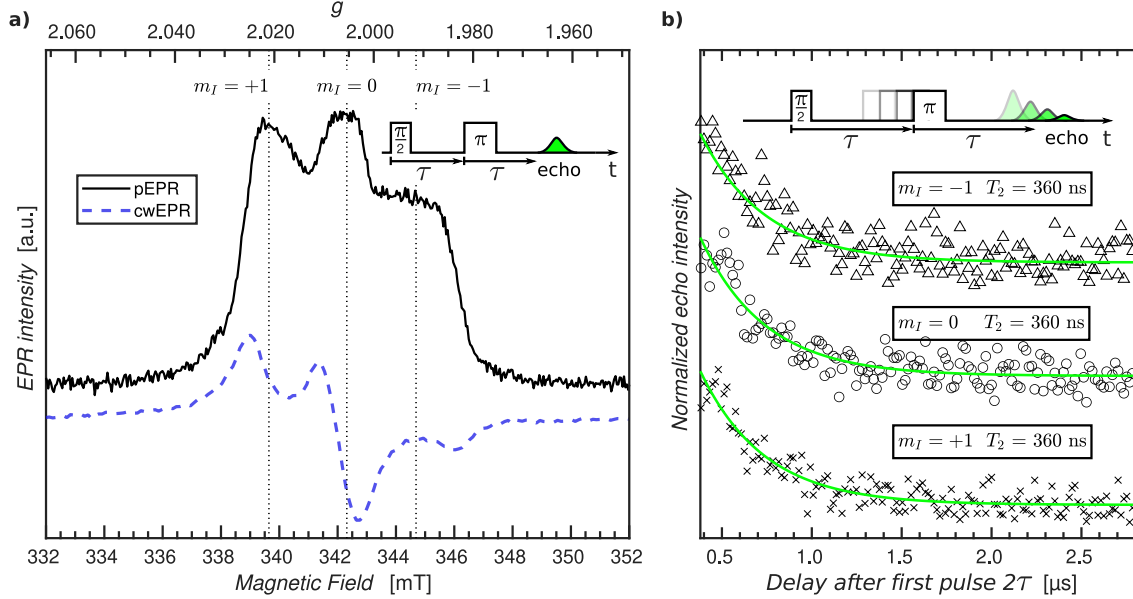


Figure 4.3: X

relative peak intensities in the echo-detected spectrum. For spins uniformly distributed in space,  $V(B_0)$  is described [102] by Equation 4.4:

$$V(B_0, 2\tau, C) = V_0(2\tau) \exp\left(-2\tau \frac{4\pi^2}{9\sqrt{3}} \gamma^2 \hbar C \langle \sin^2(\theta/2) \rangle\right) \quad (4.4)$$

with

$$\langle \sin^2(\theta/2) \rangle = \frac{\int \frac{B_1^2}{(B-B_0)^2+B_1^2} \sin^2\left(\frac{\gamma t_p}{2} \sqrt{(B-B_0)^2+B_1^2}\right) g(B) dB}{\int g(B) dB} \quad (4.5)$$

where  $B_0$  is the static magnetic field,  $C$  is the concentration of spins,  $\tau$  is the time between the first and second pulses in the microwave pulse sequence,  $\gamma$  is the gyromagnetic ratio of the electrons at resonance,  $t_p$  is the duration of the second microwave pulse,  $B_1$  is the amplitude of the second microwave pulse,  $g(B)$  is the EDFS spectrum at  $\tau = 0$  that is not affected by the instantaneous diffusion. As the resulting spectral shape depends on the spin concentration, comparing spectra simulated according to Equation 4.4 and measured spectra thus allows us to provide information about the local spin concentrations.

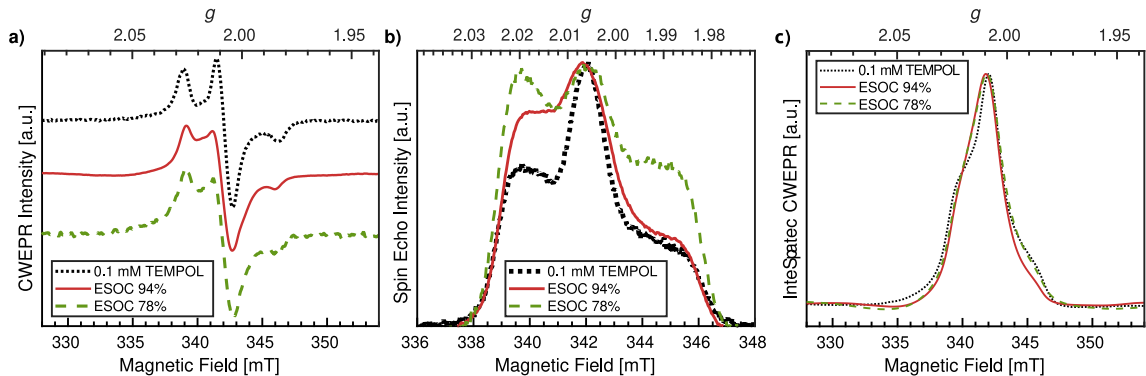


Figure 4.4: a): cwEPR spectra for pDiTBuS charged to 95% and 85%, and for a frozen 0.1 mM solution of TEMPOL. Normalized intensities. Temperature 80 K. b): Corresponding pEPR spectra measured at 5 K. Intensities scaled by the  $m_I = 0$  central peak. c): Integrated cwEPR intensities show similar spectral shapes. Temperature: 80 K, microwave frequency: 9.6 GHz, field modulation: 5 G at 100 kHz. ER 4118 X-MD5 dielectric ring resonator.

Since the spin echo of the most densely packed and thus quickly relaxing spins is not detectable with the given  $t_d$ , the regions of the highest spin concentration do not contribute to the EDFS spectrum. Thus,  $C$  is lower than the true concentration of spins in the densely packed domains and can also be lower than the average spin concentration  $\langle n \rangle$  measured with cwEPR that is most sensitive to the quickly relaxing spins.

We have used a 50 mM solution of TEMPOL as a model system to explore how the excitation bandwidth affects instantaneous diffusion for nitroxides (see Section 4.4.1, ESI). The EDFS spectrum recorded with  $t_p = 40$  ns and  $\tau = 120$  ns shows a distortion that corresponds to  $C = 9$  mM, while for  $t_p = 1000$  ns no effect of instantaneous diffusion is observed. We simulated the undistorted EDFS spectrum of TEMPOL using the Easyspin toolbox [99] for Matlab and obtained the  $g$  matrix and the hyperfine coupling tensor  $A$  (for simulation details see Section ??, ESI). Then we simulated the EDFS spectrum for pDiTBuS, ESOC 85%, using the obtained parameters and Equation 4.4 with  $t_p = 40$  ns and the concentration  $C$  as a fit parameter. The result of the simulation with  $C = 3.1 \times 10^{19} \text{ cm}^{-3} = 50$  mM is shown in Figure 4.7. At the same time, quantitative cwEPR yields a higher spin concentration for ESOC 85%:  $\langle n \rangle = (8 \pm 4) \times 10^{19} \text{ cm}^{-3} = 130 \pm 70$  mM.

The ESOC 95% spectrum cannot be simulated with Equation 4.4 because of the increased intensity of the low-field peak. The ratio of the two remaining peaks at ESOC 95%

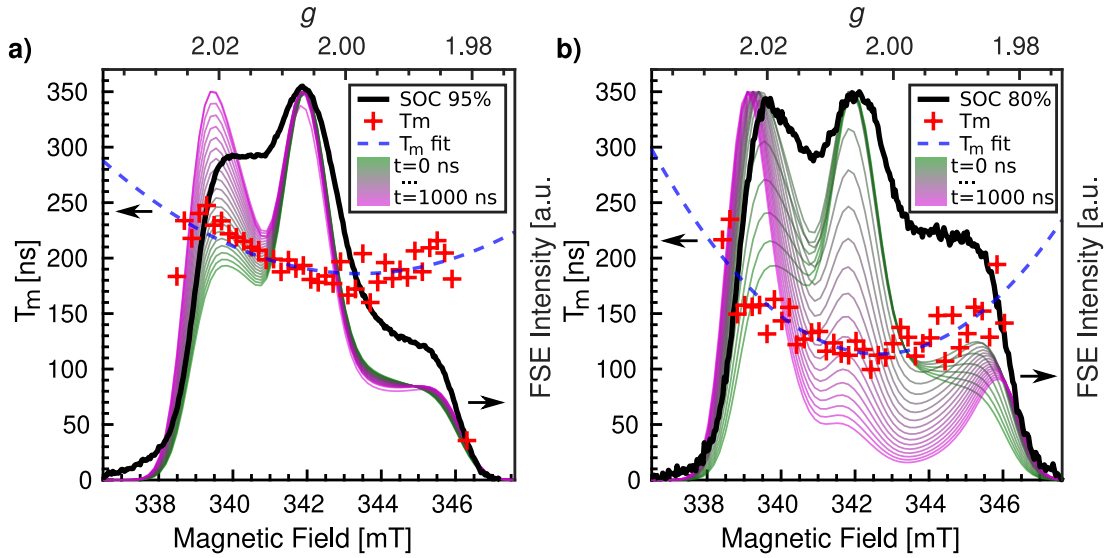


Figure 4.5: X

corresponds to  $C = 1.2 \times 10^{19} \text{ cm}^{-3} = 20 \text{ mM}$  (see ESI, Section 4.4.4), while cwEPR again yields a higher  $\langle n \rangle = 3 \pm 2 \times 10^{19} \text{ cm}^{-3} = 50 \pm 30 \text{ mM}$ .

## 4.4 Simulations of the EDFS Spectra Considering Instantaneous Diffusion

We used Equation 4.4 from the main text with varying  $C$  to fit the EDFS spectra affected by ID.

### 4.4.1 EDFS in 50 mM TEMPOL Measured with Narrow-Band Pulses

The EDFS spectrum of a 50 mM frozen solution of TEMPOL measured with long (selective, narrow band) microwave pulses shows no asymmetry with  $t_p = 1000$  ns and  $\tau = 1000$  ns. The spectrum was deconvoluted into the broad ('packed') and the narrow ('dilute') components. The narrow component is an Easyspin simulation with the typical g and A tensors for a nitroxide radical (see Figure caption for parameters). The broad spectral component might correspond to densely packed agglomerates in the not perfect glass. The fit is shown in Figure 4.8 a.

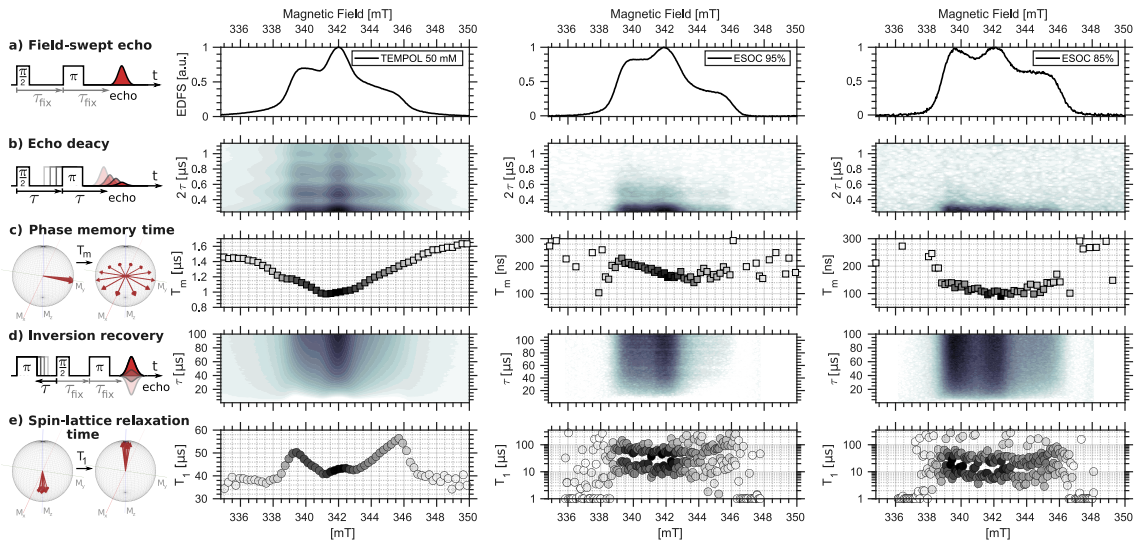


Figure 4.6: XXX

#### 4.4.2 EDFS in 50 mM TEMPOL Measured with Broad-Band Pulses

The EDFS spectrum of a 50 mM solution of TEMPOL in Figure 4.8 b shows asymmetry when measured with shorter,  $t_P = 40$  and  $\tau = 120$  ns pulses with a microwave power attenuation 11 dB. The spectrum has a stronger contribution of the broad component which in this case was calculated as the weighted integral of the cwEPR spectrum. The asymmetric dilute component was simulated considering the anisotropic relaxation of the 'standard' TEMPOL spectrum which was caused by instantaneous diffusion using Equation 4.4 in the main text. The fit of the EDFS spectrum of 50 mM TEMPOL was done with a concentration  $C = 5.6 \times 10^{18} \text{ cm}^{-3}$  or 9.3 mM as a fit parameter,  $t_P = 40$  ns,  $\tau = 120$  ns and  $\gamma = -1.76 \times 10^{11} \text{ rad/T}$  (for  $g = g_e$ ). The spin concentration determined from the instantaneous diffusion simulation is only 19% of the molecular concentration that was used to prepare the TEMPOL solution. The presence of the broad component in the EDFS spectrum suggests that the concentration of TEMPOL was not homogeneous within the sample.

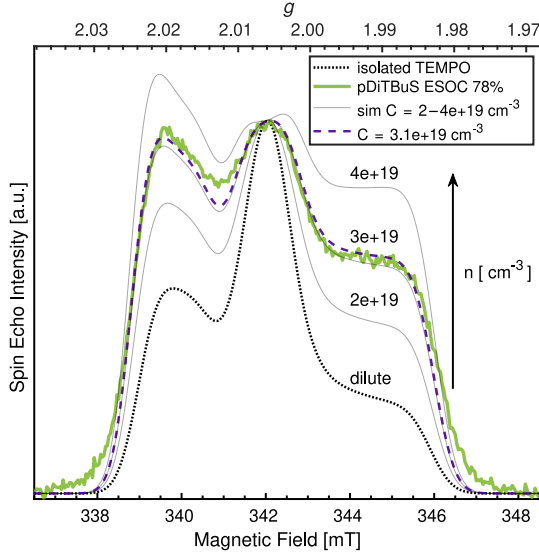


Figure 4.7: EDFS spectrum of p-DiTBuS at ESOC 85% (solid-green) affected by instantaneous diffusion with  $t_p = 40$  ns. Simulation of the spectrum with spin concentration  $C = 3.1 \times 10^{19} \text{ cm}^{-3} = 52 \text{ mM}$  as a fit parameter (dashed-purple). Simulated spectrum of non-interacting TEMPO with  $g=[2.0099, 2.0055, 2.0026]$ ,  $A=[21.99, 21.43, 96.27]$  MHz and 0.812 mT (lwpp) Gaussian line shape as the starting values for the simulation (dashed-black). Excitation profile of the 40 ns pulse at  $B_0 = 340$  mT is shown in dashed red.

#### 4.4.3 EDFS in PDiTBuS at ESOC 85% Affected by Instantaneous Diffusion

The quick echo decay in pDiTBuS necessitates the usage of short microwave pulses that lead to ID. The asymmetric EDFS spectrum of pDiTBuS at 85% ESOC was simulated considering the distortion of the standard TEMPO spectrum caused by the ID. The anisotropic relaxation of the spectral components is given by the equation 4.4 in the main text. The fit of the EDFS spectrum of pDiTBuS at 85% ESOC was done with a concentration  $C=3.1 \times 10^{19} \text{ cm}^{-3} = 50 \text{ mM}$  as a fit parameter,  $t_P = 40 \text{ ns}$ ,  $\tau = 120 \text{ ns}$  and  $\gamma = -1.76 \times 10^{11} \text{ rad/T}$ . The fit was done with  $g=[2.00987, 2.0055, 2.0026]$ ,  $A=[22.0, 21.5, 96.3]$  MHz, 0.81 mT (lwpp) Gaussian line shape, Figure 4.9.

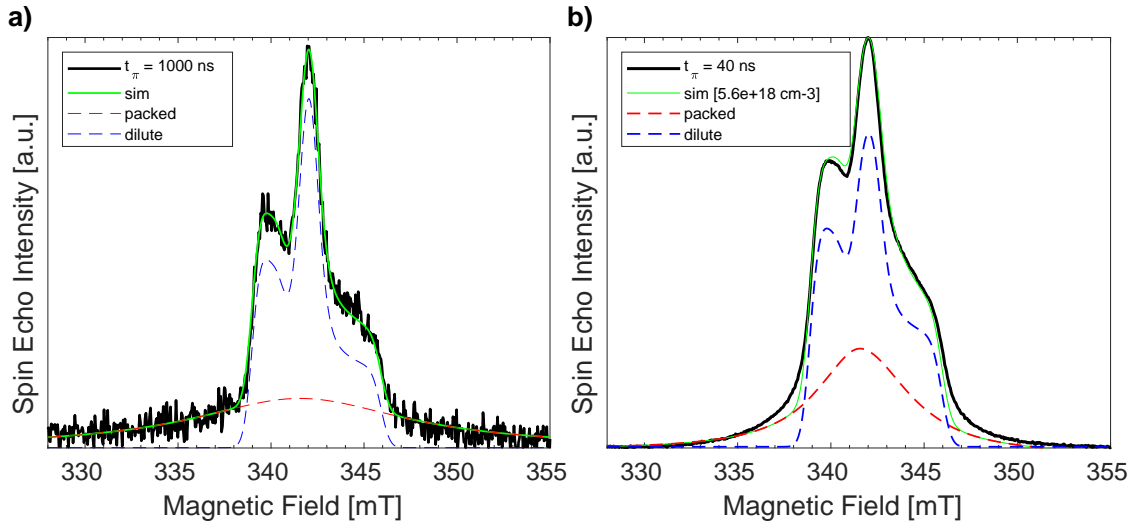


Figure 4.8: a): EDFS of 50 mM TEMPOL in Acetonitrile/Dichloromethane glass measured with long (selective, narrow-band) microwave pulses.  $t_P = 1000$  ns,  $\tau = 1000$  ns, microwave frequency: 9.6 GHz, microwave power attenuation: 36 dB. Temperature: 5 K. 2-component spectral simulation. Dilute component:  $g=[2.0099 \ 2.0055 \ 2.0026]$  and  $A=[21.9850 \ 21.4260 \ 96.2707]$  MHz. Broad component:  $g=2.0082$ ,  $l_{wpp}=8.08$  mT (Lorentzian). No effect of instantaneous diffusion is detectable with the long pulses. b): Same, measured with short (non-selective, broad-band) microwave pulses.  $t_P = 40$  ns,  $\tau = 120$  ns, microwave frequency: 9.6 GHz, microwave power attenuation: 11 dB. Temperature: 5 K. 2-component spectral simulation. Dilute component: same as in (a), but affected by the instantaneous diffusion with  $C = 5.6 \times 10^{18} \text{ cm}^{-3}$ . Broad component: integrated cwEPR spectrum.

#### 4.4.4 EDFS in PDiTBuS at ESOC 95% Affected by Instantaneous Diffusion

The asymmetric EDFS spectrum of pDiTBuS at 95% ESOC could not be simulated considering the distortion of the standard TEMPO spectrum caused by the ID given by Eq. 4.4 in the main text. The spectrum and the attempted fit are shown in Figure 4.10. The low-field peak has a much higher relative intensity than expected from the ID model. The observed spectrum may be a superposition of a dilute species that do not experience instantaneous diffusion and the densely packed species that is affected by ID.

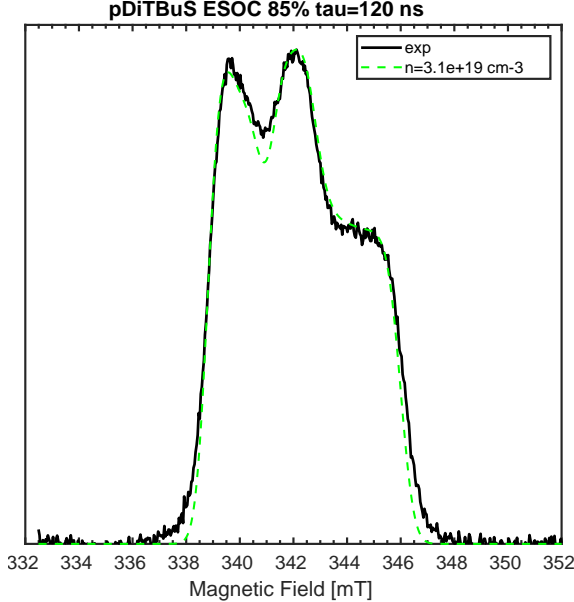


Figure 4.9: EDFS spectrum of pDiTBuS at 85% ESOC (solid-black). Spectral simulation with  $\mathbf{g}=[2.00987, 2.0055, 2.0026], \mathbf{A}=[22.0 \ 21.5 \ 96.3]$ , 0.81 mT (lwpp) Gaussian line shape and anisotropic relaxation caused by instantaneous diffusion (dashed-green). Relative peak intensities correspond to  $C=3.1\text{e}19 \text{ cm}^{-3}$  or 52 mM. Microwave frequency: 9.6 GHz,  $\pi/2 = 20$  ns,  $\tau=120$  ns. Temperature: 5 K.

#### 4.4.5 Limitation on Shortest Detectable $T_m$ by the Spectrometer Dead Time

If a system exhibits multiple phase memory times  $T_m$ , the spin echo from the species with short memory times may decay below the noise level at a given pulse separation  $\tau$ . Figure 4.27 illustrates the spin echo intensity in a two-component system with  $T_m^1 = 100$  ns and  $T_m^2 = 25$  ns in dependence on the pulse separation  $\tau$ . The fast relaxing component with  $T_m^2 = 25$  ns decays below the noise level after the dead time of  $t_d = 100$  ns.

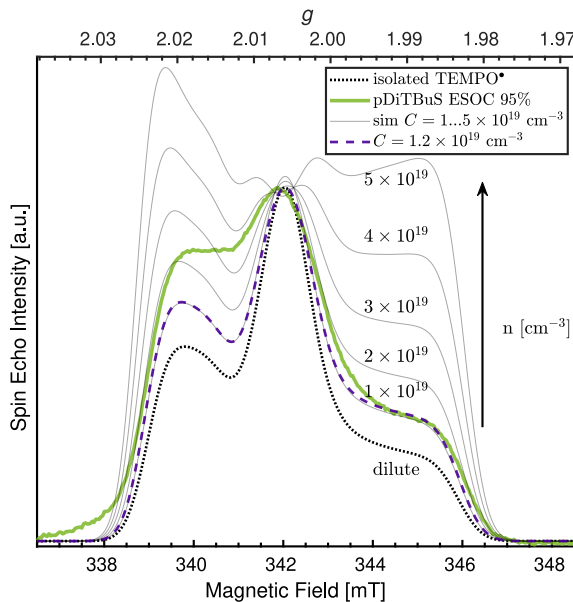


Figure 4.10: EDFS spectrum of pDiTBuS at ESOC 95% (solid-green). Spectral simulation with  $\mathbf{g}=[2.0099, 2.0055, 2.0026]$ ,  $\mathbf{A}=[21.9850 \ 21.4260 \ 96.2707]$  MHz, 0.24 mT (lwpp) Lorentzian line shape and anisotropic relaxation caused by instantaneous diffusion (dashed-blue). Relative peak intensities correspond to  $C= 1.2 \times 10^{19} \text{ cm}^{-3}$  or 22 mM. Microwave frequency: 9.6 GHz,  $\pi/2 = 20$  ns,  $\tau=120$  ns. Temperature: 5 K.

#### 4.4.6 Estimation of Local Spin Concentrations with Instantaneous Diffusion

### 4.5 Spin Relaxation in a charged pDiTBuS Cathode Film

As we have shown in Section 4.3.3, the reason for the distorted spectral shape in pDiTBuS at ESOC 85% is instantaneous diffusion that manifests itself in anisotropic spin relaxation which alters the relative peak intensities. However, the spectrum for ESOC 95% cannot be simulated assuming just instantaneous diffusion (cf. Figure 4.10, ESI). In order to gain additional information about the processes that may influence the shape of the EDFS spectra, we performed field-dependent measurements of the spin relaxation times.

Figure 4.12a shows the EDFS spectra of pDiTBuS for 85% and 95% ESOC as well as a reference sample (50 mM solution of TEMPOL in Dichloromethane:Acetonitrile (3:1) glass) measured at  $T = 5$  K. The spectra reveal markedly different intensities of the three hyperfine components.

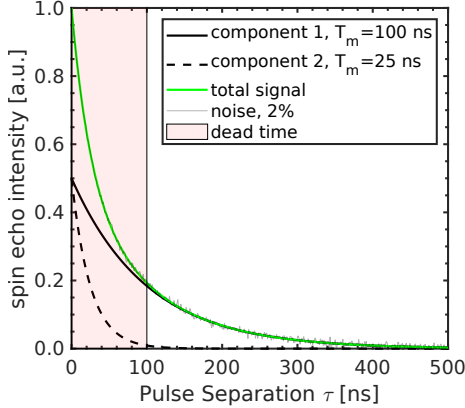


Figure 4.11: Simulated echo decay transient of a spin ensemble exhibiting two distinct phase memory times  $T_m^1 = 100$  ns and  $T_m^2 = 25$  ns. The 100 ns dead time, during which the spin echo detection is not possible, is marked in red. After the dead time, the sum of the two components is indistinguishable from the slowly relaxing component within the 2% noise.

The changed relative peak intensities in pDiTBuS may be the result of a magnetic field-dependent spin relaxation mechanism that manifests itself in a field-dependent phase memory time  $T_m$  [93]. The  $T_m$  for pDiTBuS and for TEMPOL was probed in a field-swept echo decay experiment. The echo decay transients for the three samples are shown in Figure 4.12b. A Hahn echo pulse sequence was used with a  $\pi/2$  pulse length of 20 ns and variable pulse separation time  $\tau \geq 120$  ns. Spin echo was detected at  $2\tau$  after the  $\pi/2$  pulse. Periodic oscillations in the echo decay transients correspond to the ESEEM effect from protons [93] with  $\Delta\omega_L \approx 15$  MHz, which are particularly pronounced for TEMPOL.

If the sample contains several different species (i.e. nitroxide radicals in different environments and/or different local concentration) with distinct spin-spin relaxation times, the echo decay transients may contain multiple decay components, so more than one  $T_m$  can correspond to each field point. This effect is not considered when simulating the effect of instantaneous diffusion using Equation 4.4. To determine the number of decay components in the echo decay transients, we studied the poles of the Padé approximation of the Taylor expansion of the Laplace transforms of the transients that is known as the Padé-Laplace method [37] (see ESI, Section 4.6.1 for details). This analysis revealed only monoexponential spin echo decays for both 95% ESOC and 85% ESOC. We therefore assumed a monoexponential spin echo decay for pDiTBuS, though some faster relaxing components with  $T_m < t_d$  might have decayed by the earliest achievable  $\tau$ , as shown in Section 4.6.2,

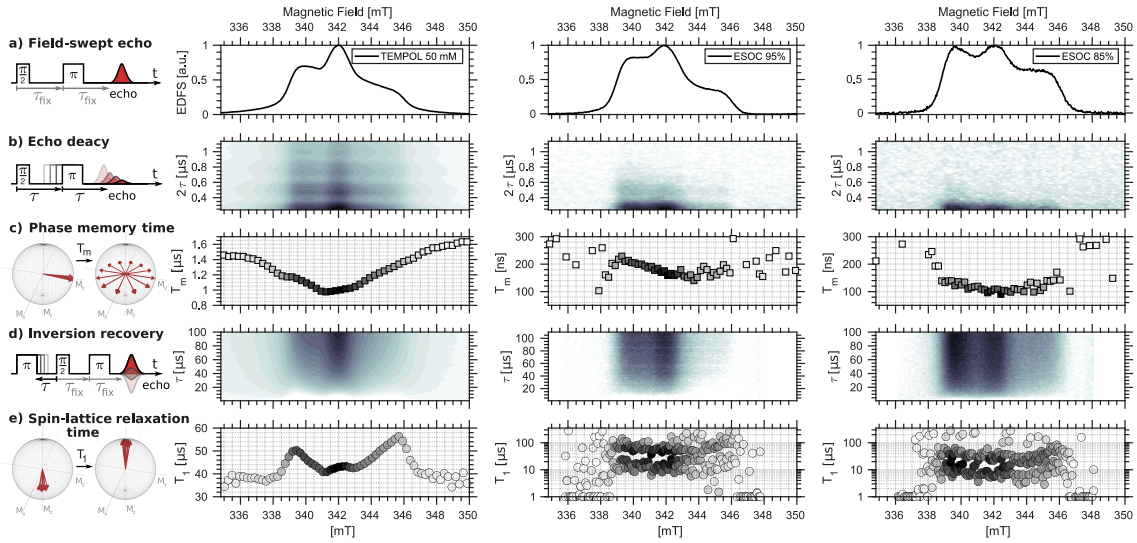


Figure 4.12: Field-swept echo (a), echo decay transients (b), phase memory times  $T_m$  (c), inversion recovery (d) and spin-lattice relaxation times  $T_1$  (e) measured in 50 mM frozen electrolyte solution of TEMPOL (left) and in dry pDiTBuS film charged to ESOC 95% (center) and to ESOC 85% (right). Temperature 5 K. Grayscale represents the intensity in b)–e).

ESI. The detected decay times  $T_m(B_0)$ , extracted from fits of the background-corrected echo-decay curves, are shown in Figure 4.12c as filled squares with the grayscale representing the amplitude of the corresponding fit component. As expected,  $T_m$  is significantly larger for 95% than for 85% ESOC, consistent with the weaker spin-spin couplings in the fully charged film. Further, we note that the field-dependence of  $T_m$  is more pronounced for 95% ESOC, with  $T_m \geq 200$  ns for the  $m_I = +1$  hyperfine component. This anisotropy in  $T_m$  results in an increased intensity of the low-field peak, which is in line with the observation that we cannot describe the 95% ESOC spectrum assuming only instantaneous diffusion (see Section 4.3.3). The transient fits and the residuals are shown in Section 4.6.1, ESI.

We attempted to reproduce the pDiTBuS spectra from a standard nitroxide spectrum by considering anisotropic transient decay of the spectral intensity at  $t = \tau = 120$  ns for each  $B_0$  with the measured  $T_m(B_0)$ . However, this approach did not allow us to reconstruct the pDiTBuS spectra for neither 85%, nor 95% ESOC.

It was recently shown, that densely packed TEMPO radicals in a TEMPO-containing,

non-conductive polymer PTMA, intermixed into an amorphous carbon mesh, show multiple spin-lattice relaxation times  $T_1$  because of different types of contact between the TEMPO radicals and the conductive additive in the TEMPO/carbon composite [15]. In order to find out whether such behavior can also be observed for the porous pDiTBuS film, we measured spin-lattice relaxation times  $T_1$  with an inversion-recovery pulse sequence ( $\pi - \tau - \pi/2 - \tau_{fix} - \pi - \tau_{fix} - echo$ ) with variable  $\tau$  (Figure 4.12d). The Padé-Laplace analysis yielded one decay component for TEMPOL and two decay components for pDiTBuS both at 85% ESOC and 95% ESOC (see ESI, Section 4.6.1 for details). The  $T_1$  for charged pDiTBuS is on the same order as for TEMPOL and splits in two rather broad distributions with similar intensities (Figure 4.12e). Similar as in the case of  $T_m$ , also  $T_1$  is larger for 95% than for 85% ESOC. Irrespective of the ESOC there is no significant field dependence of  $T_1$ , in contrast to what is observed for the TEMPOL reference sample.

Daniel et al. [15] concluded that separate distributions of  $T_1$  correspond to different binding between TEMPO and the carbon mesh, representing the quality of electrical contact between TEMPO and the conductive additive. With the observed distribution of  $T_1$  and considering the two-component cwEPR spectral contributions for charged pDiTBuS (“broad” and “dilute” components, cf. Section ??, ESI), we suggest that two types of domains could exist in a partially charged pDiTBuS film as well. These two morphologies may correspond to “conductive” domains with shorter  $T_1$ , where TEMPO $^\bullet$  are close to the conductive pNiSalen backbone, and “non-conductive” domains with longer  $T_1$ , where TEMPO $^\bullet$  are separated from pNiSalen. We note, however, that based on the experimental data presented here, this interpretation is rather speculative. The detected  $T_1$  values for pDiTBuS may also correspond to one distribution, as the separation between the  $T_1$  values is comparable to the widths of their distributions.

#### 4.5.1 Temperature Dependence of Pulse Spectra of Charged pDiTBuS

Spin relaxation times usually depend on temperature[93]. We measured EDFS of charged pDiTBuS at 5 K and at 80 K to see how faster spin relaxation affects the spectral shape. Figure 4.13 shows EDFS spectra for pDiTBuS charged to ESOC 95% (a) and to ESOC 85% (b) at 80 K (solid) and at 5 K (dashed). At 80 K an overnight scan was required to obtain a satisfactory signal-to-noise ratio, whereas at 5 K the spectrum was recorded in a few minutes. The spectral intensities at different temperatures were scaled such that the high-field  $m_I = -1$  peak has the same intensity. Figure 4.13 clearly shows that the relative intensities of the peaks change with temperature for both ESOC. At higher temperatures the EDFS

spectrum of pDiTBuS has a peak ratio closer to that of dilute TEMPOL that corresponds to a lower spin concentration, according to Equation 4.4. The influence of the temperature increase on the spectral shape is stronger for the lower, 85% ESOC.

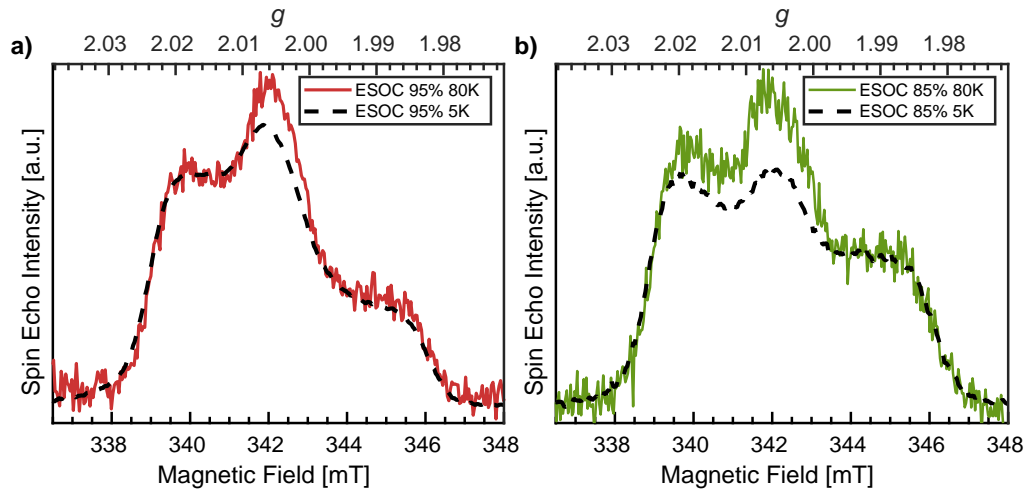


Figure 4.13: EDFs spectra for pDiTBuS charged to 95% ESOC (a) and to 85% ESOC (b) measured at 5K and at 80K.

The overall relaxation times in the film decrease with increasing temperature, but the dead time of the spectrometer ( $t_d = 120$  ns) does not change. Therefore, at a given temperature, only spins with  $T_m > t_d$  contribute to the signal. At higher temperature only the weakly coupled spins (with the longest  $T_m$ ) are detectable, which results in a spectral shape that is less affected by instantaneous diffusion and thus closer to a dilute nitroxide solution.

## 4.6 Padé-Laplace Deconvolution of Polyexponential Decay Signals

The echo decay and inversion recovery transients measured in the corresponding experiments may contain multiple exponential decay components. The conventional method of determining the distribution of the decay components in a transient decay is the Laplace inversion, where the signal in the time domain  $s(t)$  is converted into its Laplace image

$$L(p) = \int_0^{+\infty} s(t)e^{-pt}dt$$

in the time-constant domain  $p = 1/t$ , where the peaks of  $L(p)$  give

the decay constants that make up the signal. However, for the noisy signal, the direct calculation of the Laplace transform brings in artifacts that drastically vary with the noise. The signal-to-noise ratio (SNR) of the recorded data makes it difficult to apply the Laplace inversion to determine the number of the decay components, as the Laplace transform is unstable at that SNR.

The Padé-Laplace method comes useful for analyzing noisy polyexponential decays as it was demonstrated in Ref. [38]. The idea of the Padé-Laplace method is to analyze the Padé approximation of the Taylor expansion of the  $L(p)$  in the vicinity of one of the expected decay constants  $p_0$ , rather than considering the  $L(p)$  fully. This way of signal decomposition is stable against the noise for SNR<10 (see Figure 4.14). The number of exponents detected by the Padé-Laplace method as well as their locations in the  $p$  space may vary depending on the expansion point  $p_0$ . We considered  $p_0 = 1/t_{1/2}$  where  $t_{1/2}$  is the time at which the signal amplitude halves.

We implemented the following algorithm to detect the number of exponents in the decaying transient  $s(t)$ :

First, a point  $p_0 = 1/t_{1/2}$  was chosen, at which  $s(t)$  halves.

Then, 11 coefficients of the Taylor expansion of the Laplace transform  $L(p)$  were calculated in the vicinity of  $p \rightarrow p_0$

$$L(p)|_{p \rightarrow p_0} = \sum_{n=0}^{11} d_i (p - p_0)^i \quad (4.6)$$

with

$$d_i = \frac{1}{i!} \left( \frac{d^{(i)} L}{dp^{(i)}} \right)_{p=p_0} \quad (4.7)$$

where the derivatives  $\frac{d^{(i)} L}{dp^{(i)}}$  are computed numerically at the point  $p = p_0$  from the discrete signal  $s(t) = (t_j, f_j)$ ,  $j = 1 \dots M$ :

$$\frac{d^{(i)} L}{dp^{(i)}} = \sum_{j=2}^{M-1} (-t_j)^i e^{(-p_0 t_j)} f_j + \frac{1}{2} \left( (-t_1)^i e^{(-p_0 t_1)} f_1 + (-t_M)^i e^{(-p_0 t_M)} f_M \right) \quad (4.8)$$

Then the Taylor expansion for  $L(p)$  was approximated in the vicinity of  $p_0$  with the Padé polynomials  $a(p)$  and  $b(p)$  of orders  $n = 5$  and  $n = 6$  respectively:

$$L(p)|_{p \rightarrow p_0} = d_0 + d_1(p - p_0) + \dots + d_{11}(p - p_0)^{11} = \frac{a_0 + a_1(p - p_0) + \dots + a_5(p - p_0)^5}{1 + b_1(p - p_0) + \dots + b_6(p - p_0)^6} \quad (4.9)$$

The equation 4.9 is multiplied by the denominator and the prefactors at  $(p - p_0)^n$  for  $n = 6 \dots 11$  are compared. This defines a system of linear equations on coefficients  $b_i$ :

$$\begin{pmatrix} d_5 & d_4 & d_3 & d_2 & d_1 & d_0 \\ d_6 & d_5 & d_4 & d_3 & d_2 & d_1 \\ d_7 & d_6 & d_5 & d_4 & d_3 & d_2 \\ d_8 & d_7 & d_6 & d_5 & d_4 & d_3 \\ d_9 & d_8 & d_7 & d_6 & d_5 & d_4 \\ d_{10} & d_9 & d_8 & d_7 & d_6 & d_5 \end{pmatrix} \begin{pmatrix} b_1 \\ b_2 \\ b_3 \\ b_4 \\ b_5 \\ b_6 \end{pmatrix} = \begin{pmatrix} -d_6 \\ -d_7 \\ -d_8 \\ -d_9 \\ -d_{10} \\ -d_{11} \end{pmatrix} \quad (4.10)$$

From 4.10,  $b_i$  are found. The coefficients  $a_i$  are found from  $d$  and  $b$ .

Finally, the Padé approximation  $P = \frac{a}{b}$  is constructed and its poles are analyzed. The position of the poles reveal the decay constants. The residues at the poles may give the amplitudes of the decay components, but this was not used in the present study.

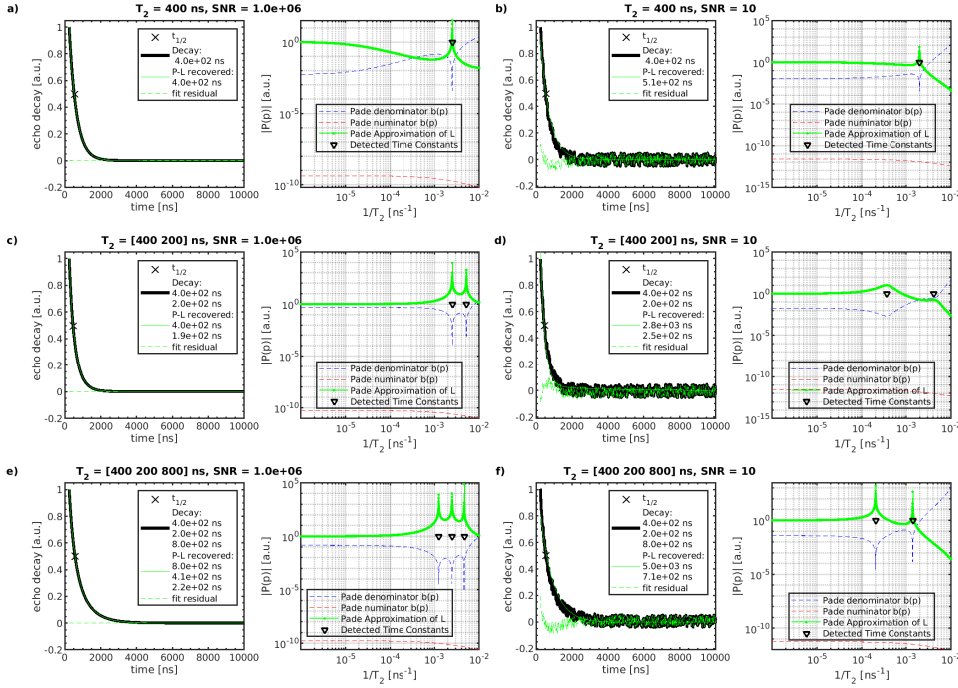


Figure 4.14: Padé-Laplace deconvolution of the mock data containing two decay constants with various signal-to-noise (SNR) ratios.

#### 4.6.1 Padé-Laplace Deconvolution of the Echo-Decay and Inversion-Recovery Transients

We used the Padé-Laplace method to determine the number of the decay constants in the signals and used multiexponential fits to adjust the decay constants and their amplitudes. For the echo decay transients the best fits were monoexponential fits, even though the Padé-Laplace analysis initially showed biexponential behavior for pDiTBuS with major contribution from the fast decay constants in the order of the detector's dead time. All recorded echo decay transients contain oscillations due to the ESEEM effect. The oscillations were excluded from the analysis as shown in the 'fit area' on the plots in Figure 4.16, Figure 4.18 and Figure 4.20.

### Echo Decay in 50 mM TEMPOL

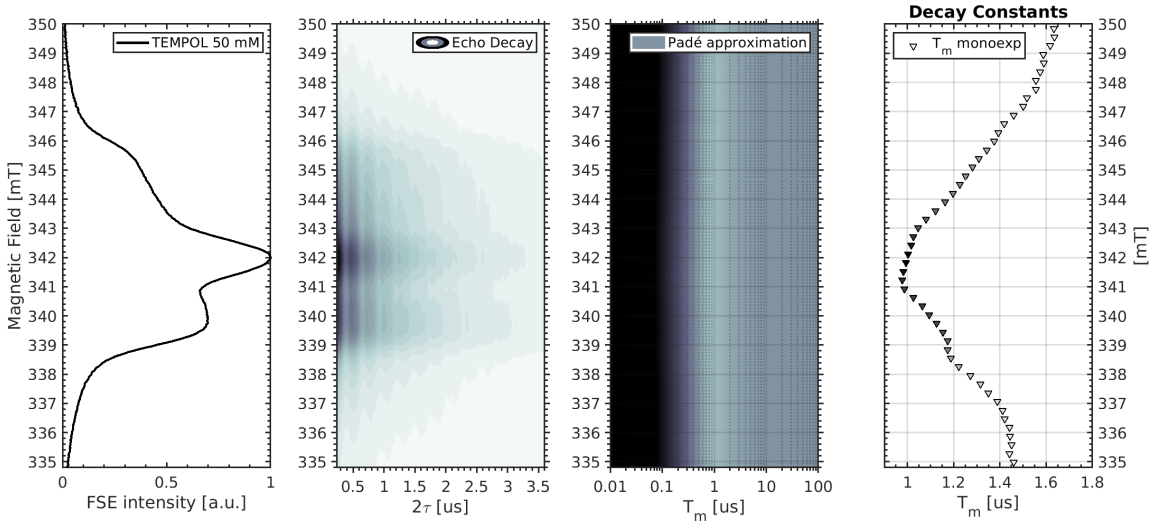


Figure 4.15: Padé-Laplace deconvolution of the field-swept spin echo decay in a frozen 50 mM solution of TEMPOL in Dichloromethane:Acetonitrile glass (3:1). One decay component detected with Padé-Laplace (triangles, right panel). Monoexponential fit (squares for faster component, circles for slower component, right panel). Temperature 5K.

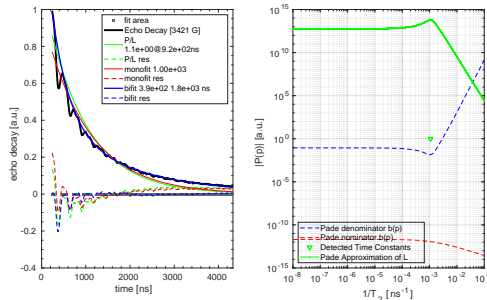


Figure 4.16: Fits of the echo decay transient in the frozen 50 mM TEMPOL solution at the central spectral peak ( $m_I = 0$ , 342 mT). Padé-Laplace deconvolution the transient vs. free monoexponential fit vs biexponential fit. Temperature 5K. Data was fit in the 'fit area' region. ESEEM oscillations were excluded from the data for fit and Padé-Laplace analysis.

## Echo Decay in DiTBuS 95% ESOC

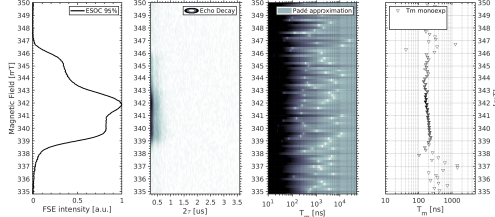


Figure 4.17: Padé-Laplace deconvolution of the field-swept spin echo decay in the pDiTBuS film at 95% ESOC. Temperature 5K.

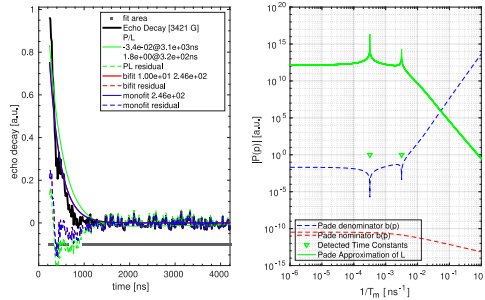


Figure 4.18: Fits of the echo decay transient in the pDiTBuS film at 95% SoC at the central spectral peak ( $m_I = 0$ , 342 mT). Padé-Laplace deconvolution the transient vs. free monoexponential fit vs biexponential fit. Temperature 5K. Data was fit in the 'fit area' region. ESEEM oscillations were excluded from the data for fit and Padé-Laplace analysis.

### Echo Decay in DiTBuS 85% ESOC

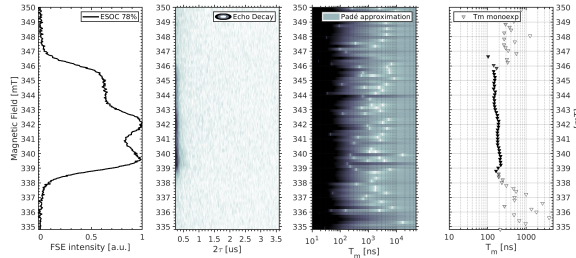


Figure 4.19: Padé-Laplace deconvolution of the field-swept spin echo decay in a pDiTBuS film at 85% ESOC. Temperature 5K.

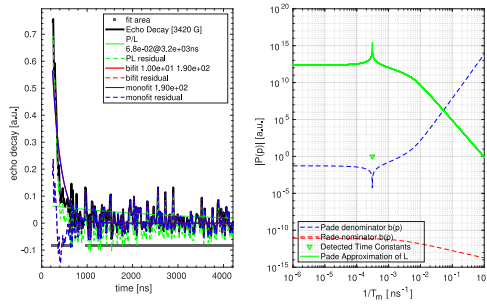


Figure 4.20: Padé-Laplace deconvolution, biexponential and monoexponential fits of the spin echo decay in a pDiTBuS film at 85% SoC at the  $m_I = 0$  spectral position. Temperature 5K. Data was fit in the 'fit area' region. ESEEM oscillations were excluded from the data for fit and Padé-Laplace analysis.

### Inversion Recovery in 50 mM TEMPOL

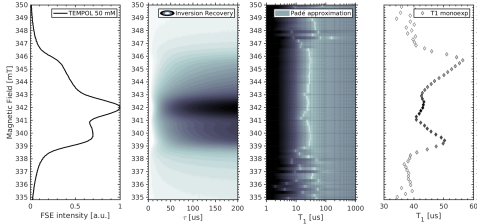


Figure 4.21: Padé-Laplace deconvolution of the field-swept inversion recovery in a frozen 50 mM solution of TEMPOL in the Dichloromethane:Acetonitrile glass (3:1). Two decay components detected with Pade-Laplace (separated poles in the Padé-Laplace approximation, third panel). Biexponential fit (circles for faster component, squares for slower component, right panel). Temperature 5K.

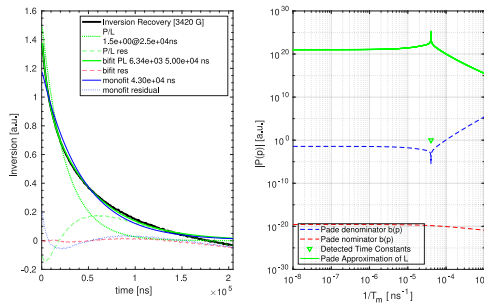


Figure 4.22: Fits of the inversion recovery transient in the frozen 50 mM TEMPOL solution at the central spectral peak ( $m_I = 0$ , 342 mT). Padé-Laplace deconvolution the transient and a biexponential fit. Temperature 5K.

### Inversion Recovery in DiTBuS 95% ESOC

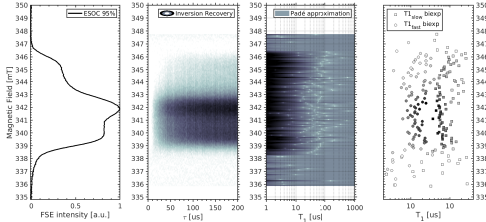


Figure 4.23: Padé-Laplace deconvolution of the field-swept inversion recovery in a pDiTBuS film at 95% ESOC. Temperature 5K.

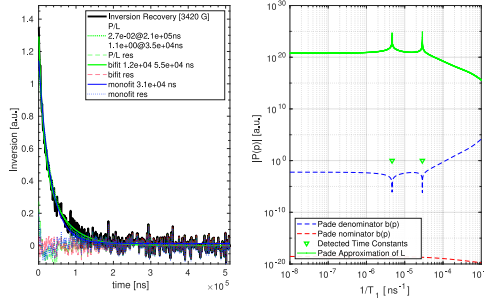


Figure 4.24: Fits of the inversion recovery transient in the 95% ESOC pDiTBuS film at the central spectral peak ( $m_I = 0$ , 342 mT). Padé-Laplace deconvolution the transient and a biexponential fit. Temperature 5K.

### Inversion Recovery in DiTBuS 85% ESOC

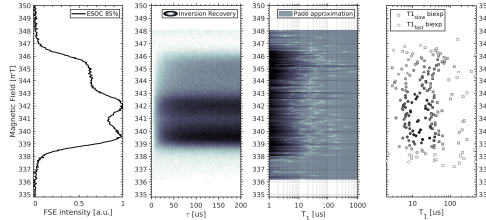


Figure 4.25: Pade-Laplace deconvolution of the field-swept inversion recovery in a pDiTBuS film at 85% ESOC. Temperature 5K.

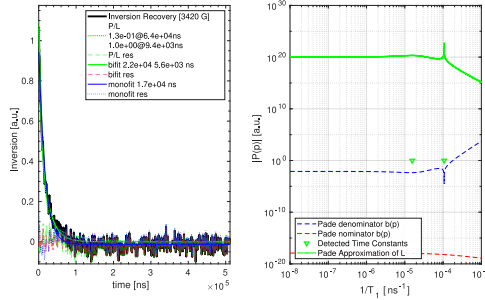


Figure 4.26: Pade-Laplace deconvolution and biexponential fit of the inversion recovery in a pDiTBuS film at 85% ESOC at the  $m_I = 0$  spectral position. Temperature 5K. Data is inverted and scaled before fitting.

### 4.6.2 Limitation on Shortest Detectable $T_m$ by the Spectrometer Dead Time

If a system exhibits multiple phase memory times  $T_m$ , the spin echo from the species with short memory times may decay below the noise level at a given pulse separation  $\tau$ . Figure 4.27 illustrates the spin echo intensity in a two-component system with  $T_m^1 = 100$  ns and  $T_m^2 = 25$  ns in dependence on the pulse separation  $\tau$ . The fast relaxing component with  $T_m^2 = 25$  ns decays below the noise level after the dead time of  $t_d = 100$  ns.

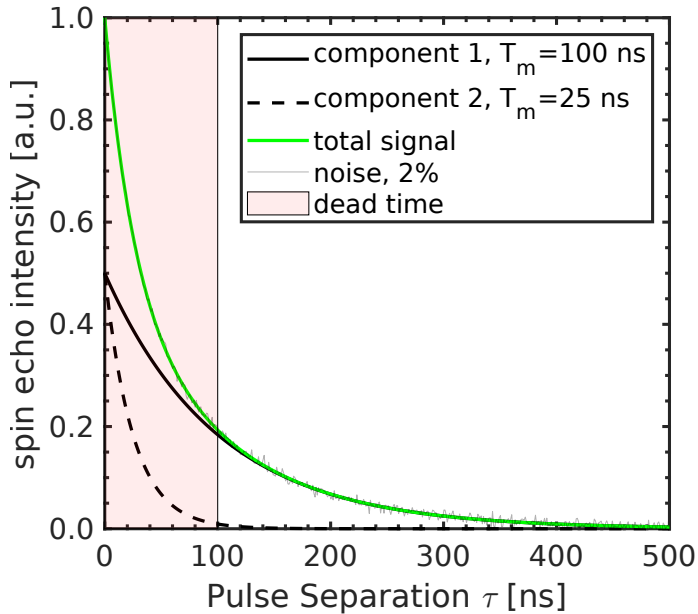


Figure 4.27: Simulated echo decay transient of a spin ensemble exhibiting two distinct phase memory times  $T_m^1 = 100$  ns and  $T_m^2 = 25$  ns. The 100 ns dead time, during which the spin echo detection is not possible, is marked in red. After the dead time, the sum of the two components is indistinguishable from the slowly relaxing component within the 2% noise.

#### 4.6.3 Detection of Domains with Poor Conductivity

#### 4.6.4 Towards Electron Resonance Imaging of Spin Concentrations in Battery Electrodes

The local spin concentrations that are present in an electrode film can be obtained by the time-constant-domain analysis of the echo decay transients, as it was described in 4.6.3. One can extend this characterization technique and obtain a spatially resolved image of the spin concentrations inside the battery electrode by encoding the position at which the sample is excited with a gradient of the magnetic field. A strongly asymmetric ferromagnetic wedge [29] can be used to superimpose a gradient of  $B_0$  in a chosen direction so one can not only measure the spin concentrations that are present in the electrode, but also to locate the electrochemically inactive domains and to visualize the conductive paths throughout the electrode, analogously to the NMR imaging. The difficulty on the way to apply this visualization technique lies in the large excitation bandwidth of the pulse sequence.

Let the cathode film of width  $l$  be oriented along the static magnetic field so that  $B_0$  lies

in the film plane. Let the  $B_0$  be fixed at the maximum intensity of the FSE spectrum, say,  $B_0 = B_0^{res} = 342$  mT. Let  $B_0$  be homogeneous within the film length, which is normally the case for the EPR resonator. Let the film contain a distribution of spin concentrations within its length  $C_{min} < C(z) < C_{max}$ . With the homogeneous  $B_0$ , the microwave pulse will excite the entire film length and the spin echo signal will contain spin echoes from all length elements of the film, that correspond to all  $C(z)$ . The inversion recovery transient will contain the time constants from all length elements of the film  $T_1(z)$ . With the Padé-Laplace analysis one recovers the distribution of the concentrations within the film  $C_i$ , but since the  $B_0$  is homogeneous, the information on the position  $z_i$  at which the domains are located, is lost.

Let now the  $B_0$  to be linearly increasing from  $B_0(z = -l/2) = B_0^{res} - \Delta B_0$  at one side of the film to  $B_0(z = l/2) = B_0^{res} + \Delta B_0$  by the other side of the film, so that for a given length element  $dl$  the inhomogeneity of  $B_0$  is  $dB/dl = \frac{B(z=l/2)-B(z=-l/2)}{l}$ . In the center of the film (at  $z = 0$ ) the  $B_0$  is resonant and the spin echo signal will be generated, while from the other positions of the film the magnetic field will be non-resonant and no spin echo signal will be generated. Let the width of the EPR spectrum be  $\Delta B_{FWHM} = 8$  mT and that to define the probed length element  $\Delta l$  with the given  $B_0$  gradient.  $\frac{\Delta B_{FWHM}}{\Delta l} = \frac{B(z=l/2)-B(z=-l/2)}{l}$ , so the spatial resolution is

$$\frac{\Delta l}{l} = \frac{\Delta B_{FWHM}}{B(z = l/2) - B(z = -l/2)} \quad (4.11)$$

With the spectral width of  $\Delta B_{FWHM} \leq 8$  mT and the film width of  $l \leq 3 \times 10^{-1}$  cm to get 256 points per film length one needs a  $B_0$  gradient of  $dB/dl \geq 256 * 8 / 0.3 \geq 6.8$  [T/cm] which is a realistic value for a typical Stern-Gerlach apparatus [29, 62].



# **Chapter 5**

## **Conclusions and Outlook**

What hasn't worked so far is the EDMR. It would be super cool to see the signal, but my devices don't live that long. LOD also did not work up to now. Adjusting the pulse train rate to the eigenfrequency of the ENDOR coils turned out to be an irresistible obstacle.

EDMR is allowing to manipulate the spin of an electron that tunnels through a disordered media such as the amorphous silicon in a solar cell, through intertwined fragments of conjugated polymers in an organic solar cell or an organic field-effect transistor.



# Bibliography

- [1] Kaltum Abdiaziz, Enrico Salvadori, Katarzyna P Sokol, Erwin Reisner, and Maxie M Roessler. Protein film electrochemical epr spectroscopy as a technique to investigate redox reactions in biomolecules †. *Chem. Commun.*, 55:8840, 2019.
- [2] R. V. Apraksin, Y. A. Volosatova, A. I. Volkov, P. S. Vlasov, D. A. Lukyanov, I. R. Kulikov, S. N. Eliseeva, and O. V. Levin. Electrochemical synthesis and characterization of poly [ni(ch<sub>3</sub>osalen)] with immobilized poly(styrenesulfonate) anion dopants. *Electrochimica Acta*, 368:137637, 2021.
- [3] Muhammed Aydin and Burak Esat. A polythiophene derivative bearing two electroactive groups per monomer as a cathode material for rechargeable batteries. *Journal of Solid State Electrochemistry*, 19:2275–2281, 8 2015.
- [4] S Bahceci and B Esat. A polyacetylene derivative with pendant tempo group as cathode material for rechargeable batteries. *Journal of Power Sources*, 242:33–40, 2013.
- [5] Allen J. Bard, Larry R. Faulkner, and Henry S. White. *Electrochemical Methods. Funcamentals and Applications*, volume 1. Wiley, 2 edition, 2022.
- [6] Loris Bennett, Bernd Melchers, and Boris Proppe. Curta: A general-purpose high-performance computer at zedat, freie universität berlin. <http://dx.doi.org/10.17169/refubium-26754>, 2020.
- [7] Robert Bittl and Stefan Weber. Transient radical pairs studied by time-resolved epr. *Biochimica et Biophysica Acta - Bioenergetics*, 1707:117–126, 2005.
- [8] Enrica Bordignon. Epr spectroscopy of nitroxide spin probes. *eMagRes*, 6:235–254, 2017.
- [9] A Carrington and A. D. McLachlan. *Introduction to Magnetic Resonance with Applications to Chemistry and Chemical Physics*. John Weatherhill, inc, 1969.

- [10] A Carrington and A. D. McLachlan. *Introduction to Magnetic Resonance with Applications to Chemistry and Chemical Physics*. John Weatherhill, inc, 1969.
- [11] Nerea Casado and David Mecerreyes. Chapter 1: Introduction to redox polymers: Classification, characterization methods and main applications, 2021.
- [12] Nerea Casado and David Mecerreyes. *Redox Polymers for Energy and Nanomedicine*. The Royal Society of Chemistry, 2021.
- [13] Harold Cassidy. Electron exchange-polymers. *J. Am. Chem. Soc.*, 71:402–406, 1949.
- [14] Davis Thomas Daniel, Steffen Oevermann, Souvik Mitra, Katharina Rudolf, Andreas Heuer, Rüdiger A. Eichel, Martin Winter, Diddo Diddens, Gunther Brunklaus, and Josef Granwehr. Multimodal investigation of electronic transport in ptma and its impact on organic radical battery performance. *Scientific Reports*, 13, 12 2023.
- [15] Davis Thomas Daniel, Conrad Szczuka, Peter Jakes, Rüdiger-A. Eichel, and Josef Granwehr. Laplace inverted pulsed epr relaxation to study contact between active material and carbon black in li–organic battery cathodes. *Physical Chemistry Chemical Physics*, 25:12767–12776, 2023.
- [16] Florian Degen and Marius Schütte. Life cycle assessment of the energy consumption and ghg emissions of state-of-the-art automotive battery cell production. *Journal of Cleaner Production*, 330:129798, 2022.
- [17] Boucar Diouf and Christophe Avis. The potential of li-ion batteries in ecowas solar home systems. *Journal of Energy Storage*, 22:295–301, 2019.
- [18] Evgenia Dmitrieva, Marco Rosenkranz, Julia S. Danilova, Evgenia A. Smirnova, Mikhail P. Karushev, Irina A. Chepurnaya, and Aleksander M. Timonov. Radical formation in polymeric nickel complexes with n2o2 schiff base ligands: An in situ esr and uv–vis–nir spectroelectrochemical study. *Electrochimica Acta*, 283:1742–1752, 2018.
- [19] Sandra S Eaton, Lukas B Woodcock, and Gareth R Eaton. Continuous wave electron paramagnetic resonance of nitroxide biradicals in fluid solution. *Concepts in Magnetic Resonance Part A: Bridging Education and Research*, 47A:1–16, 2018.
- [20] A. Einstein. Relativity the special and general theory, 1921.

- [21] X. Fan, T. G. Myers, B. A.D. Sukra, and G. Gabrielse. Measurement of the electron magnetic moment. *Physical Review Letters*, 130, 2 2023.
- [22] Chen Fang, Thanh Nhan Tran, Yangzhi Zhao, and Gao Liu. Electrolyte decomposition and solid electrolyte interphase revealed by mass spectrometry, 12 2021.
- [23] M. Fehr, J. Behrends, S. Haas, B. Rech, K. Lips, and A. Schnegg. Electrical detection of electron-spin-echo envelope modulations in thin-film silicon solar cells. *Physical Review B - Condensed Matter and Materials Physics*, 84:1–5, 11 2011.
- [24] R P Feynman. Space-time appxoach to quantum electxotiyynamics. *Physical Review*, 76:769–789, 1949.
- [25] Jan Figgener, Peter Stenzel, Kai Philipp Kairies, Jochen Linßen, David Haberschus, Oliver Wessels, Georg Angenendt, Martin Robinius, Detlef Stolten, and Dirk Uwe Sauer. The development of stationary battery storage systems in germany – a market review. *Journal of Energy Storage*, 29, 6 2020.
- [26] C Fribe and U S Schubert. High-power-density organic radical batteries. *Topics in Current Chemistry*, 375:1–35, 2017.
- [27] Yangyang Fu, Song Lu, Kaiyuan Li, Changchen Liu, Xudong Cheng, and Heping Zhang. An experimental study on burning behaviors of 18650 lithium ion batteries using a cone calorimeter. *Journal of Power Sources*, 273:216–222, 1 2015.
- [28] Yangyang Fu, Song Lu, Kaiyuan Li, Changchen Liu, Xudong Cheng, and Heping Zhang. An experimental study on burning behaviors of 18650 lithium ion batteries using a cone calorimeter. *Journal of Power Sources*, 273:216–222, 1 2015.
- [29] Walther Gerlach and Otto Stern. Der experimentelle nachweis der richtungsquantelung im magnetfeld. *Zeitschrift für Physik*, 9:348–352, 1922.
- [30] Nicolas Goujon, Nerea Casado, Nagaraj Patil, Rebeca Marcilla, and David Mecerreyes. Organic batteries based on just redox polymers: Abstract. *Progress in Polymer Science*, 122:101449, 2021.
- [31] Cristina Grosu, Chiara Panosetti, Steffen Merz, Peter Jakes, Stefan Seidlmayer, Sebastian Matera, Rüdiger a Eichel, Josef Granwehr, and Christoph Scheurer. Revisiting the storage capacity limit of graphite battery anodes : Spontaneous lithium overintercalation at ambient pressure. *PRX Energy*, 2:1–14, 2023.

- [32] Ting Guan, Shun Sun, Fengbin Yu, Yunzhi Gao, Peng Fan, Pengjian Zuo, Chunyu Du, and Geping Yin. The degradation of  $\text{LiCoO}_2$ /graphite batteries at different rates. *Electrochimica Acta*, 279:204–212, 2018.
- [33] Karin Halbmair, Jan Seikowski, Igor Tkach, Claudia Höbartner, Deniz Sezer, and Marina Bennati. High-resolution measurement of long-range distances in rna: Pulse epr spectroscopy with tempo-labeled nucleotides. *Chemical Science*, 7:3172–3180, 2016.
- [34] Padinhare Cholakkal Harikesh, Chi-Yuan Yang, Deyu Tu, Jennifer Y. Gerasimov, Abdul Manan Dar, Adam Armada-Moreira, Matteo Massetti, Renee Kroon, David Bliman, Roger Olsson, Eleni Stavrinidou, Magnus Berggren, and Simone Fabiano. Organic electrochemical neurons and synapses with ion mediated spiking. *Nature Communications*, 13:901, 12 2022.
- [35] Xiyue He and Xuelai Zhang. A comprehensive review of supercapacitors: Properties, electrodes, electrolytes and thermal management systems based on phase change materials, 12 2022.
- [36] Alan J Heeger. Semiconducting and metallic polymers: The fourth generation of polymeric materials. *The Journal of Physical Chemistry B*, 105:8475–8491, 9 2001.
- [37] Edward H. Hellen. Padé–laplace analysis of signal averaged voltage decays obtained from a simple circuit. *American Journal of Physics*, 73:871–875, 2005.
- [38] Edward H. Hellen. Padé–laplace analysis of signal averaged voltage decays obtained from a simple circuit. *American Journal of Physics*, 73:871–875, 9 2005.
- [39] Takuma Hirasawa, Mika Yoshida, and Shin’ya Obara. Battery control for leveling the amount of electricity purchase in smart-energy houses. *International Journal of Energy Research*, 45:807–823, 2021.
- [40] Peng Hu, Xuexia He, and Hui Jiang. Greater than  $10 \text{ cm}^2 \text{ V}^{-1} \text{ s}^{-1}$ : A breakthrough of organic semiconductors for field-effect transistors, 6 2021.
- [41] Q Huang, E D Walter, L Cosimbescu, D Choi, and J P Lemmon. In situ electrochemical-electron spin resonance investigations of multi-electron redox reaction for organic radical cathodes. *Journal of Power Sources*, 306:812–816, 2016.
- [42] T Janoschka, M D Hager, and U S Schubert. Powering up the future: Radical polymers for battery applications. *Adv. Mater.*, 24:6397–6409, 2012.

- [43] Tobias Janoschka, Christian Friebe, Martin D. Hager, Norbert Martin, and Ulrich S. Schubert. An approach toward replacing vanadium: A single organic molecule for the anode and cathode of an aqueous redox-flow battery. *ChemistryOpen*, 6:216–220, 2017.
- [44] Tobias Janoschka, Christian Friebe, Martin D. Hager, Norbert Martin, and Ulrich S. Schubert. An approach toward replacing vanadium: A single organic molecule for the anode and cathode of an aqueous redox-flow battery. *ChemistryOpen*, 6:216–220, 2017.
- [45] G Jeschke. Deer distance measurements on proteins. *Annual Review of Physical Chemistry*, Vol 63, 63:419–446, 2012.
- [46] Josef Kadlec, Radoslav Cipin, Dalibor Cervinka, Pavel Vorel, and Bohumil Klima. Li-ion accumulators for propulsion system of electric airplane vut 051 ray. *Journal of Solid State Electrochemistry*, 18:2307–2313, 2014.
- [47] T Katsumata, M Satoh, J Wada, M Shiotsuki, F Sanda, and T Masuda. Polyacetylene and polynorbornene derivatives carrying tempo. synthesis and properties as organic radical battery materials. *Macromolecular Rapid Communications*, 27:1206–1211, 2006.
- [48] M Khodeir, B Ernould, J Brassinne, S Ghiassinejad, H Jia, S Antoun, C Friebe, U S Schubert, Z Kochovski, Y Lu, E Van Ruymbeke, and J F Gohy. Synthesis and characterisation of redox hydrogels based on stable nitroxide radicals. *Soft Matter*, 15:6418–6426, 2019.
- [49] Jihyeon Kim, Youngsu Kim, Jaekyun Yoo, Giyun Kwon, Youngmin Ko, and Kisuk Kang. Organic batteries for a greener rechargeable world. *Nature Reviews Materials*, 8:54–70, 2023.
- [50] H Koezuka, A Tsumura, and T Ando. Field-effect transistor with polythiophene thin film, 1987.
- [51] Kenichiroh Koshika, Naoki Sano, Kenichi Oyaizu, and Hiroyuki Nishide. An aqueous, electrolyte-type, rechargeable device utilizing a hydrophilic radical polymer-cathode. *Macromolecular Chemistry and Physics*, 210:1989–1995, 11 2009.
- [52] Ilia Kulikov, Naitik A. Panjwani, Anatoliy A. Vereshchagin, Domenik Spallek, Daniil A. Lukianov, Elena V. Alekseeva, Oleg V. Levin, and Jan Behrends. Spins

- at work: probing charging and discharging of organic radical batteries by electron paramagnetic resonance spectroscopy. *Energy and Environmental Science*, 15:3275–3290, 2022.
- [53] Ilia Kulikov, Anatoliy A. Vereshchagin, Daniil A. Lukianov, Oleg V. Levin, and Jan Behrends. A nitroxide-containing cathode material for organic radical batteries studied with pulsed epr spectroscopy. *Journal of Magnetic Resonance Open*, 16-17, 12 2023.
- [54] Ilya Kuprov. *Spin: From Basic Symmetries to Quantum Optimal Control*. Springer International Publishing, 1 2023.
- [55] T. Kushida and J. C. Murphy. Volume dependence of the knight shift in lithium. *Physical Review B*, 21:4247–4250, 1980.
- [56] Yury Kutin, Nicholas Cox, Wolfgang Lubitz, Alexander Schnegg, and Olaf Rüdiger. In situ epr characterization of a cobalt oxide water oxidation catalyst at neutral ph. *Catalysts*, 9, 11 2019.
- [57] Anna Köhler and Heinz Bässler. Electronic processes in organic semiconductors, 2015.
- [58] Fredrik Larsson, Petra Andersson, Per Blomqvist, and Bengt Erik Mellander. Toxic fluoride gas emissions from lithium-ion battery fires. *Scientific Reports*, 7:1–13, 12 2017.
- [59] C H Lee, G Yu, D Moses, K Pakbaz, C Zhang, N S Sariciftci, A J Heeger, and F Wudl. Sensitization of the photoconductivity of conducting polymers by c60: Photoinduced electron transfer, 1993.
- [60] Yong Hee Lee, Joo Seong Kim, Jonghyeon Noh, Inhwa Lee, Hyeong Jun Kim, Sunghun Choi, Jeongmin Seo, Seokwoo Jeon, Taek Soo Kim, Jung Yong Lee, and Jang Wook Choi. Wearable textile battery rechargeable by solar energy. *Nano Letters*, 13:5753–5761, 2013.
- [61] Chao Li, Ming Shen, and Bingwen Hu. Solid-state nmr and epr methods for metal ion battery research. *Wuli Huaxue Xuebao/Acta Physico - Chimica Sinica*, 36:1–16, 2019.
- [62] Jiahao Liang, Thomas M. Fuchs, Rolf Schäfer, and Vitaly V. Kresin. Strong permanent magnet gradient deflector for stern-gerlach-type experiments on molecular beams. *Review of Scientific Instruments*, 91, 5 2020.

- [63] Xiangli Liu, Yougang Mao, Errol V. Mathias, Collin Ma, Osmundo Franco, Yong Ba, Julia A. Kornfield, Tieli Wang, Lijun Xue, Bing Sen Zhou, and Yun Yen. Study the property of double-ended fluoroalkyl poly(ethylene glycol) hydrogel as a depot for hydrophobic drug delivery using electron paramagnetic resonance technique and cell proliferation assay. *Journal of Sol-Gel Science and Technology*, 45:269–278, 3 2008.
- [64] Yong Lu and Jun Chen. Prospects of organic electrode materials for practical lithium batteries. *Nature Reviews Chemistry*, 4:127–142, 2020.
- [65] Tianyi Ma, Siyuan Wu, Fang Wang, Joseph Lacap, Chunjing Lin, Shiqiang Liu, Mohan Wei, Weijian Hao, Yunshi Wang, and Jae Wan Park. Degradation mechanism study and safety hazard analysis of overdischarge on commercialized lithium-ion batteries. *ACS Applied Materials and Interfaces*, 12:56086–56094, 2020.
- [66] Praveen Kumar Reddy Maddikunta, Gautam Srivastava, Thippa Reddy Gadekallu, Natarajan Deepa, and Prabadevi Boopathy. Predictive model for battery life in iot networks. *IET Intelligent Transport Systems*, 14:1388–1395, 2020.
- [67] Christoph Meier, Jan Behrends, Christian Teutloff, Oleksandr Astakhov, Alexander Schnegg, Klaus Lips, and Robert Bittl. Multi-frequency edmr applied to micro-crystalline thin-film silicon solar cells. *Journal of Magnetic Resonance*, 234:1–9, 2013.
- [68] Alice J. Merryweather, Quentin Jacquet, Steffen P. Emge, Christoph Schnedermann, Akshay Rao, and Clare P. Grey. Operando monitoring of single-particle kinetic state-of-charge heterogeneities and cracking in high-rate li-ion anodes. *Nature Materials*, 21:1306–1313, 2022.
- [69] S Muench, A Wild, C Friebe, B Haupler, T Janoschka, and U S Schubert. Polymer-based organic batteries. *Chemical Reviews*, 116:9438–9484, 2016.
- [70] K Nakahara, S Iwasa, M Satoh, Y Morioka, J Iriyama, M Suguro, and E Hasegawa. Rechargeable batteries with organic radical cathodes. *Chem. Phys. Lett.*, 359:351–354, 2002.
- [71] David B Newell and Eite Tiesinga. The international system of units (si);, 8 2019.
- [72] Arvid Niemöller, Peter Jakes, Rüdiger A. Eichel, and Josef Granwehr. In operando epr investigation of redox mechanisms in licoo<sub>2</sub>. *Chemical Physics Letters*, 716:231–236, 2019.

- [73] Arvid Niemöller, Peter Jakes, Svitlana Eurich, Anja Paulus, Hans Kungl, Rüdiger A. Eichel, and Josef Granwehr. Monitoring local redox processes in  $\text{LiNi}_0.5\text{Mn}_1.5\text{O}_4$  battery cathode material by in operando epr spectroscopy. *Journal of Chemical Physics*, 148:1–10, 2018.
- [74] H Nishide, S Iwasa, Y J Pu, T Suga, K Nakahara, and M Satoh. Organic radical battery: nitroxide polymers as a cathode-active material. *Electrochimica Acta*, 50:827–831, 2004.
- [75] Hiroyuki Nishide, Kenichiro Koshika, and Kenichi Oyaizu. Environmentally benign batteries based on organic radical polymers. volume 81, pages 1961–1970, 2009.
- [76] Naoki Nitta, Feixiang Wu, Jung Tae Lee, and Gleb Yushin. Li-ion battery materials: Present and future. *Materials Today*, 18:252–264, 2015.
- [77] M. V. Novozhilova, E. A. Smirnova, M. P. Karushev, A. M. Timonov, V. V. Malev, and O. V. Levin. Synthesis and study of catalysts of electrochemical oxygen reduction reaction based on polymer complexes of nickel and cobalt with schiff bases. *Russian Journal of Electrochemistry*, 52:1183–1190, 12 2016.
- [78] Cavendish Laboratory University of Cambridge. Organic semiconductors, 2018.
- [79] D E O'reilly. Exchange narrowing in electron paramagnetic resonance of ruby. *Chemical Physics Letters*, 10:239–241, 1971.
- [80] Dongxu Ouyang, Jingwen Weng, Mingyi Chen, Jiahao Liu, and Jian Wang. Experimental analysis on the degradation behavior of overdischarged lithium-ion battery combined with the effect of high-temperature environment. *International Journal of Energy Research*, 44:229–241, 2020.
- [81] Rikard Owenius, Maria Engström, Mikael Lindgren, and Martina Huber. Influence of solvent polarity and hydrogen bonding on the epr parameters of a nitroxide spin label studied by 9-ghz and 95-ghz epr spectroscopy and dft calculations. *Journal of Physical Chemistry A*, 105:10967–10977, 2001.
- [82] Kenichi Oyaizu, Hanae Tatsuhira, and Hiroyuki Nishide. Facile charge transport and storage by a tempo-populated redox mediating polymer integrated with polyaniline as electrical conducting path. *Polymer Journal*, 47:212–219, 2 2015.

- [83] Dirac P. A. M. The quantum theory of the electron. *Proceedings of the Royal Society of London. Series A, Containing Papers of a Mathematical and Physical Character*, 117:610–624, 1928.
- [84] Jens F. Peters, Manuel Baumann, Benedikt Zimmermann, Jessica Braun, and Marcel Weil. The environmental impact of li-ion batteries and the role of key parameters – a review. *Renewable and Sustainable Energy Reviews*, 67:491–506, 2017.
- [85] M. H. Poincaré. Sur la dynamique de l'électron. *Rend. Circ. Matem. Palermo*, pages 129–175, 12 1906.
- [86] Anna Pražanová, Vaclav Knap, and Daniel Ioan Stroe. Literature review, recycling of lithium-ion batteries from electric vehicles, part i: Recycling technology. *Energies*, 15:1–29, 2022.
- [87] Kevin J. Rhodes, Roberta Meisner, Melanie Kirkham, Nancy Dudney, and Claus Daniel. In situ xrd of thin film tin electrodes for lithium ion batteries. *Journal of The Electrochemical Society*, 159:A294–A299, 2012.
- [88] Philip Rohland, Erik Schröter, Oliver Nolte, George R. Newkome, Martin D. Hager, and Ulrich S. Schubert. Redox-active polymers: The magic key towards energy storage – a polymer design guideline progress in polymer science, 2 2022.
- [89] J. J. Sakurai and Jim Napolitano. *Modern Quantum Mechanics*. Dorling Kindersley Pvt. Ltd., 2 edition, 2014.
- [90] K. M. Salikhov, S. A. Dzuba, and A. M. Raitsimring. The theory of electron spin-echo signal decay resulting from dipole-dipole interactions between paramagnetic centers in solids. *Journal of Magnetic Resonance*, 42:255–276, 1981.
- [91] K M Salikhov and N E Zavoiskaya. Zavoisky and the discovery of epr, 2015.
- [92] Pierre Olivier Schwartz, Marijana Pejic, Mario Wachtler, and Peter Bäuerle. Synthesis and characterization of electroactive pedot-tempo polymers as potential cathode materials in rechargeable batteries. *Synthetic Metals*, 243:51–57, 9 2018.
- [93] A Schweiger and G Jeschke. *Principles of Pulse Electron Paramagnetic Resonance*. Oxford University Press, 2001.
- [94] J Schwinger. On quantum-electrodynamics and the magnetic moment of the electron. *Physical Review*, 73:416–417, 1948.

- [95] Yongchao Shi and Mingxue Tang. Nmr/epr investigation of rechargeable batteries. *Wuli Huaxue Xuebao/Acta Physico - Chimica Sinica*, 36:1–13, 2019.
- [96] By Hideki Shirakawa, Edwin J Louis, Alan G Macdiarmid, C H W A N K Chiang, and Alan J HEEGERt. Synthesis of electrically conducting organic polymers : Halogen derivatives of polyacetylene, (ch), 1977.
- [97] Domenik Spallek. Spin-dependent processes in organic radical batteries, master thesis, 6 2022.
- [98] H. Staudinger. Über polymerisation. *European Journal of Inorganic Chemistry*, 53:1073–1085, 6 1920.
- [99] Stefan Stoll and Arthur Schweiger. Easyspin, a comprehensive software package for spectral simulation and analysis in epr. *Journal of Magnetic Resonance*, 178:42–55, 1 2006.
- [100] Hiroyuki Takeo Nishide and Suga. Organic radical battery. *Journal of the Society of Mechanical Engineers*, 110:194–195, 2007.
- [101] Nir Tessler, Yevgeni Preezant, Noam Rappaport, and Yohai Roichman. Charge transport in disordered organic materials and its relevance to thin-film devices: A tutorial review. *Advanced Materials*, 21:2741–2761, 2009.
- [102] Yu. V. Toropov, S. A. Dzuba, Yu. D. Tsvetkov, V Monaco, F Formaggio, M Crisma, C Toniolo, and J. Raap. Molecular dynamics and spatial distribution of toac spin-labelled peptaibols studied in glassy liquid by echo-detected epr spectroscopy. *Applied Magnetic Resonance*, 15:237–246, 1998.
- [103] Anatolii. A. Vereshchagin, Daniil A. Lukyanov, Ilia R. Kulikov, Naitik A. Panjwani, Elena A. Alekseeva, Jan Behrends, and Oleg V. Levin. The fast and the capacious: A [ni(salen)]-tempo redox-conducting polymer for organic batteries. *Batteries and Supercaps*, 4:336–346, 2020.
- [104] Anatoliy A. Vereshchagin, Arseniy Y. Kalnin, Alexey I. Volkov, Daniil A. Lukyanov, and Oleg V. Levin. Key features of tempo-containing polymers for energy storage and catalytic systems. *Energies*, 15:1–50, 2022.
- [105] Anatoly A. Vereshchagin, Petr S. Vlasov, Alexander S. Konev, Peixia Yang, Galina A. Grechishnikova, and Oleg V. Levin. Novel highly conductive cathode material based on stable-radical organic framework and polymerized nickel complex

- for electrochemical energy storage devices. *Electrochimica Acta*, 295:1075–1084, 2 2019.
- [106] John A. Weil and James R. Bolton. *Electron Paramagnetic Resonance Elementary Theory and Practical Applications*. Wiley, 2nd edition, 2007.
- [107] Ting Ting Wu, Gao Le Dai, Jin Jia Xu, Fang Cao, Xiao Hong Zhang, Yu Zhao, and Yu Min Qian. Structural design of organic battery electrode materials: from dft to artificial intelligence, 10 2023.
- [108] Y Xie, K Zhang, Y Yamauchi, K Oyaizu, and Z F Jia. Nitroxide radical polymers for emerging plastic energy storage and organic electronics: fundamentals, materials, and applications. *Materials Horizons*, 8:803–829, 2021.
- [109] Yuan Xie, Kai Zhang, Yusuke Yamauchi, Kenichi Oyaizu, and Zhongfan Jia. Nitroxide radical polymers for emerging plastic energy storage and organic electronics: Fundamentals, materials, and applications. *Materials Horizons*, 8:803–829, 2021.
- [110] Chengjian Xu, Qiang Dai, Linda Gaines, Mingming Hu, Arnold Tukker, and Bernhard Steubing. Future material demand for automotive lithium-based batteries. *Communications Materials*, 1:1–10, 2020.
- [111] Lihuan Xu, Fang Yang, Chang Su, Lylv Ji, and Cheng Zhang. Synthesis and properties of novel tempo-contained polypyrrole derivatives as the cathode material of organic radical battery. *Electrochimica Acta*, 130:148–155, 6 2014.
- [112] He Yan, Zhihua Chen, Yan Zheng, Christopher Newman, Jordan R. Quinn, Florian Dötz, Marcel Kastler, and Antonio Facchetti. A high-mobility electron-transporting polymer for printed transistors. *Nature*, 457:679–686, 2 2009.
- [113] H T Yi, Y N Gartstein, and V Podzorov. Charge carrier coherence and hall effect in organic semiconductors. *Scientific Reports*, 6:1–11, 2016.
- [114] Hyun Deog Yoo, Elena Markevich, Gregory Salitra, Daniel Sharon, and Doron Aurbach. On the challenge of developing advanced technologies for electrochemical energy storage and conversion. *Materials Today*, 17:110–121, 2014.
- [115] E K Zavoisky. Paramagnetic relaxation of liquid solutions for perpendicular fields. *Zhur. Eksperiment. i Theoret. Fiz.*, 15:344–350, 1945.

- [116] E K Zavoisky. Spin-magnetic resonance in paramagnetics. *Journal of Physics*, 9:245, 1945.
- [117] Clara Zens, Christian Friebe, Ulrich S. Schubert, Martin Richter, and Stephan Kupfer. Tailored charge transfer kinetics in precursors for organic radical batteries – a joint synthetic-theoretical approach. *ChemSusChem*, e202201679:1–14, 2022.
- [118] Guangxu Zhang, Xuezhe Wei, Siqi Chen, Guangshuai Han, Jiangong Zhu, and Haifeng Dai. Investigation the degradation mechanisms of lithium-ion batteries under low-temperature high-rate cycling. *ACS Applied Energy Materials*, 5:6462–6471, 2022.
- [119] Qingsong Zhang, Tiantian Liu, and Qiong Wang. Experimental study on the influence of different heating methods on thermal runaway of lithium-ion battery. *Journal of Energy Storage*, 42:1–9, 10 2021.
- [120] Yiren Zhang, Albert M. Park, Stephen R. McMillan, Nicholas J. Harmon, Michael E. Flatté, Gregory D. Fuchs, and Christopher K. Ober. Charge transport in conjugated polymers with pendent stable radical groups. *Chemistry of Materials*, 30:4799–4807, 7 2018.
- [121] Lingyun Zhu, Yuanping Yi, Yuan Li, Eung Gun Kim, Veaceslav Coropceanu, and Jean Luc Brédas. Prediction of remarkable ambipolar charge-transport characteristics in organic mixed-stack charge-transfer crystals. *Journal of the American Chemical Society*, 134:2340–2347, 2 2012.

# **Appendix A:**

## **Electron Magnetic Resonance**

### **Environment**

A python-based interactive program EMRE (Electron Magnetic Resonance Environment) was developed to interconnect and control the EPR spectrometer and to simultaneously operate the electrochemical device under testing. The program allows one to perform electrochemical measurements such as cyclic voltammetry and galvanostatic charge-discharge cycling and to simultaneously record cwEPR spectra with customizable, lab-built and commercial EPR spectrometers. Most of the redox conductive films considered in this thesis were manufactured using EMRE. Additionally, some of the potential-dependent spectra and degradation studies were carried out using EMRE. The source code of the program and the documentation is available at the remote repository:

[https://github.com/rst030/EMRE.](https://github.com/rst030/EMRE)